University of Wisconsin Milwaukee
UWM Digital Commons

Theses and Dissertations

May 2019

In Situ Chemical Probing of Vacancy Defects in Graphene and Boron Nitride at Room Temperature

Ali Ihsan Altan
University of Wisconsin-Milwaukee

Follow this and additional works at: https://dc.uwm.edu/etd

 Part of the Chemistry Commons, and the Materials Science and Engineering Commons

Recommended Citation
Altan, Ali Ihsan, "In Situ Chemical Probing of Vacancy Defects in Graphene and Boron Nitride at Room Temperature" (2019). *Theses and Dissertations*. 2037.
https://dc.uwm.edu/etd/2037

This Dissertation is brought to you for free and open access by UWM Digital Commons. It has been accepted for inclusion in Theses and Dissertations by an authorized administrator of UWM Digital Commons. For more information, please contact open-access@uwm.edu.

IN SITU CHEMICAL PROBING OF VACANCY DEFECTS IN GRAPHENE AND BORON NITRIDE AT ROOM TEMPERATURE

by

Ali Ihsan Altan

A Dissertation Submitted in

Partial Fulfillment of the

Requirements for the Degree of

Doctor of Philosophy

in Chemistry

at

The University of Wisconsin-Milwaukee

May 2019

ABSTRACT

IN SITU CHEMICAL PROBING OF VACANCY DEFECTS IN GRAPHENE AND BORON NITRIDE AT ROOM TEMPERATURE

by

Ali Ihsan Altan

The University of Wisconsin-Milwaukee, 2019
Under the Supervision of Professor Jian Chen

Chemical vapor deposition (CVD) has emerged as the most promising technique towards manufacturing of large area, high quality graphene. Characterization, understanding, and controlling of various structural defects in CVD-grown graphene are essential to realize its true potential for real-world applications. We report a new method for *in situ* chemical probing of vacancy defects in CVD-grown graphene at room temperature. Our approach is based on a solid–gas phase reaction that occurs selectively in graphene vacancy defect regions such as holes and cracks. Our new probing technique has a unique combination of the following advantages: (1) no exposure to liquids; (2) non-damaging *in situ* probing; (3) high selectivity, sensitivity, and reliability towards vacancy defects; (4) simplicity and scalability. By focusing on hexagonal graphene domains, we have made the following findings: (1) the nucleation centers of graphene domains are favorable locations of hole defects. (2) The lengthy electron-beam irradiation at very low energy (3.5 keV) could etch the graphene. (3) Graphene cracks often kink at the angle of primarily 150° or 120°. (4) There exist complex graphene cracks such as cracks with clock-hands patterns, and cracks with snowflake-like branched structures. (5) There exist discontinuous cracks in some graphene domains, where hole defects are oriented along a straight or curved line. Such discontinuous cracks may arise from the ductile fracture of graphene. In addition, we have shown that our method is also applicable to chemical probing

of vacancy defects such as holes, continuous and discontinuous cracks in CVD-grown monolayer polycrystalline graphene films on copper. Our study also suggests that the copper grain and copper grain boundary play significant roles in formation and distribution of graphene vacancy defects. We have studied and clarified potential effects of graphene wrinkles on the formation of vacancy defects in polycrystalline graphene and single crystalline graphene, respectively. We have found that although the graphene wrinkles are the main source for vacancy defects in the polycrystalline CVD-grown graphene samples, there are other possible sources such as mechanical stress that are responsible for the formation of vacancy defects in polycrystalline graphene where wrinkles are not found. In contrast, we have found that graphene wrinkles are NOT mainly responsible for the observed vacancy defects in single crystalline hexagonal graphene domains, which provides further indirect support that the copper grain and copper grain boundary play significant roles in formation and distribution of graphene vacancy defects, and the observed discontinuous cracks more likely originate from a ductile fracture of graphene.

The practical investigation of individual nanoscale vacancy defects in h-BN still remains a great challenge. Hence, it is important to develop a method for rapidly identification of the vacancy defects in large area monolayer h-BN, which will provide insightful information on defect formation in h-BN. We have performed *in situ* chemical probing study of vacancy defects in CVD-grown h-BN. Our H_2S gas treatment procedure reveals that currently commercially available CVD-grown monolayer h-BN samples have high density of nanoscale voids. High defect density in monolayer h-BN appears to be caused by the hardship of stitching of individual domains with various rotations and edge atoms. It has been shown that h-BN may have nanoscale vacancy defects along the grain boundaries which is different than graphene. It is

important to limit H_2S amount and treatment time for our method to work well towards identification of vacancies.

To

My parents Gulseren and Ali Altan

And

My wife Ashley Jenkins Altan

And

My twin daughters Leyla and Sarah Altan

TABLE OF CONTENTS

TABLE OF CONTENTS vi

Chapter 1: Introduction 1

1.1. Graphene 1

1.2. Chemical Vapor Deposition (CVD) Graphene 3

1.3. Defects in CVD-grown graphene 4

1.4. Observation of structural defects in CVD-grown graphene 6

1.4.1. Nanoparticle deposition 9

1.4.2. Liquid crystal deposition 10

1.4.3. Oxidation Methods 11

1.4.4. Under-etching Method 13

1.5. References 14

Chapter 2: *In Situ* Chemical Probing of Hole Defects and Cracks in Graphene at Room Temperature 19

2.1. Introduction 19

2.2. Experimental 20

2.2.1. Materials 20

2.2.2. Characterization 21

2.2.3. Graphene dry-transfer 21

2.2.4. H_2S treatment of graphene on copper foil 22

2.3. Results and Discussion 23

2.3.1 Characterization of CVD-grown graphene samples 23

2.3.2 Chemical probing of vacancy defects in hexagonal graphene domains 25

2.3.3. Chemical probing of vacancy defects in polycrystalline graphene films 43

2.3.4. H_2S-related issues 52

2.3.5. Minimization of H_2S usage 58

2.4. Conclusion 61

2.5. References 62

Chapter 3: Preliminary investigation of Origins of Vacancy Defects in CVD-Grown Graphene 65

3.1. Introduction 65

3.2 Experimental 73
3.2.1 Characterization 73
3.2.2 H_2S treatment of graphene on copper foil 73
3.3 Results and Discussion 74
3.3.1 The relationship between discontinuous cracks and wrinkles in polycrystalline graphene films 74
3.3.2 The relationship between discontinuous cracks and wrinkles in hexagonal graphene domains 77
3.3.2.1 The hexagonal graphene domains with wrinkle and no discontinuous crack 78
3.4. Conclusion 81
3.5 References 82
Chapter 4: *In Situ* Chemical Probing of Defects in Hexagonal Boron Nitride (h-BN) at Room Temperature 84
4.1. Introduction 84
4.1.1. Chemical Vapor Deposition (CVD) h-BN 85
4.1.2. Defects in Chemical Vapor Deposition (CVD) h-BN 87
4.1.3. Characterization of CVD-grown monolayer h-BN 90
4.2. Experimental 92
4.2.1. Materials 92
4.2.2. Characterization 92
4.2.3. H_2S treatment of h-BN on copper foil 93
4.3. Results and Discussion 94
4.3.1 Characterization of CVD-grown h-BN samples 94
4.3.2. Chemical probing of vacancy defects in polycrystalline h-BN films 98
4.4. Conclusion 105
4.5. References 106
Curriculum Vitae 126

LIST OF FIGURES

Figure 1.1. Graphene, a single layer of carbon atoms in a honeycomb lattice.[1] 1

Figure 1.2. Mechanical exfoliation of graphene from graphite flakes, 'scotch tape method'.[4] .. 2

Figure 1.3. Illustration of the graphene growth mechanism on copper in CVD process, as divided into three main steps.[19] 3

Figure 1.4. Shapes of the line defects in CVD-grown graphene.[32] 5

Figure 1.5. Aberration-corrected TEM image of a hole in a single layer of graphene. Scale bar: 5 Å.[37] 6

Figure 1.6. Individual Raman spectra taken from 4 representative locations on graphene (left). Spectroscopic Raman mapping of graphene grains and grain boundary (right). (a) inside a single crystalline graphene grain, (b) on the grain boundary location, (c) on a defect site, which could be a nucleation center, inside an individual grain, and (d) on the edge of graphene.[40] 7

Figure 1.7. (a) STM image of a grain boundary in graphene. Scale bar: 1 nm.[33] **(b)** Aberration corrected TEM image of a hole in a single layer of graphene. Scale bar: 5 Å.[37] 8

Figure 1.8. Visualization of one-dimensional defects in CVD-grown graphene by ALD. **(a)** Schematic of selective Pt growth on various line defects such as grain boundaries, cracks and folded structures in CVD graphene. **(b)** SEM image of graphene on a glass substrate after 500 ALD cycles of Pt deposition. **(c)** SEM image of graphene with Pt deposition after 1000 ALD cycles. Scale bar: 2 μm.[49] 9

Figure 1.9. (a) Schematic of liquid crystal alignment on the surface of the graphene. The alignment directions of liquid-crystal molecules depend on the orientations of graphene domains. **(b)** POM images of graphene islands coated with liquid-crystal molecules on glass. **(c,d)** POM images of polycrystalline and monocrystalline graphene films coated with liquid-crystal molecules on a Cu substrate, respectively.[45] 11

Figure 1.10. Observation of graphene grain boundaries after ultraviolet exposure under moisture-rich ambient conditions. **(a)** Schematic of the ultraviolet treatment of a graphene on

copper sample. **(b,c)** Optical images of graphene on copper before **(b)** and after **(c)** oxidation. **(d)** SEM image of oxidized graphene on copper. **(e)** AFM image of the location marked by a red square in **(c)**.[51] 12

Figure 1.11. (a) Schematic illustration of the under-etching process for CVD-grown graphene on copper foil. SEM images showing the etch pits formed after iron chloride solution etch for **(b)** 5 s, **(c)** 30 s, **(d)** 60 s.[60] 13

Figure 2.1. Photo of the reaction setup before sealing and injection of dilute H_2SO_4 solution. The double vials ensure that the graphene sample is only exposed to H_2S gas which is generated *in situ*, not any liquids or solids. Scale bar: 1 cm. 22

Figure 2.2. Representative SEM images of the purchased CVD-grown graphene on copper. (a) The pristine continuous graphene film from the front side of the sample. The white arrows indicate copper grain boundaries. (b) Pristine multiple hexagonal graphene domains as well as coalesced domains from the back side of the sample. Scale bar: 20 µm. 24

Figure 2.3. Representative Raman spectra of the pristine graphene film and individual hexagonal graphene domain transferred onto Si wafer. **(a-d)** Microscopic optical images of the graphene film and individual hexagonal graphene domain on Si wafer and the green dots showing spots where the Raman spectra were taken. Scale bars: 4 µm **(a-b)** and 2 µm **(c-d)**. **(e-i)** Raman spectrum of **(a)** and **(e-ii)** Raman spectrum of **(b)**, different regions of monolayer graphene film on Si wafer. **(f-i)** Raman spectrum of the spot in **(c)** and **(f-ii)** Raman spectrum of the spot in **(d)** in the same hexagonal graphene domain on Si wafer. Both continuous graphene film from front side and individual hexagonal domain from back side of CVD-grown graphene show the characteristic features of the monolayer graphene. 25

Figure 2.4. Schematic illustration of the *in situ* chemical probing principle. **(a)** The solid-gas phase reactions between H_2S gas and exposed copper substrate in the air lead to formation of Cu_2S nanoparticles at room temperature.[1,2] **(b)** Untreated monolayer hexagonal graphene domain on copper. The H_2S treatment leads to selective formation of Cu_2S nanoparticles in graphene vacancy defect regions. This allows for visualization of various types of graphene vacancy defects under SEM: **(c)** Hole defects; **(d,e)** Hole defect generated by low-energy electron-beam irradiation; **(f)** Various continuous cracks; **(g)** Discontinuous cracks..... 26

Figure 2.5. EDX spectrum **(b)** of a nanoparticle formed on graphene domain after the H_2S treatment. Electron beam was focused on the center of the nanoparticle (indicated by the green arrow) in the SEM image **(a)**. Scale bar: 3 µm. 27

Figure 2.6. XRD pattern of Cu_2S nanoparticles scraped off from the copper foil surface. The asterisks indicate diffraction peaks coming from copper particles..... 28

Figure 2.7. Elemental analysis of particle found on the graphene domain on copper foil. **(a)** EDS beam is focused on the center of the particle on a graphene domain that is indicated by the arrow in the SEM image. **(b)** The EDS spectrum of the particle. Scale bar is 2 μm. 29

Figure 2.8. SEM images of monolayer hexagonal graphene domains on copper foil before and after H_2S gas treatment. **(a,b)** No Cu_2S nanoparticle is detected after H_2S treatment. **(c,d)** Cu_2S nanoparticle is formed only at the nucleation center of graphene domain. **(e-h)** Cu_2S nanoparticles emerge from SiO_x nanoparticle sites (indicated by blue arrows) after H_2S treatment. Scale bar: 2 μm. 30

Figure 2.9. SEM images of monolayer hexagonal graphene domain on copper foil before and after H_2S gas treatment following electron beam application. **(a)** Electron beam (3.5 KeV) is applied to the point #1 (1 min), #2 (2 min), #3 (3 min), #4 (4 min), and #5 (5 min), respectively. **(b)** Cu_2S nanoparticles are found on the point #2-#5 after 15 min of H_2S treatment. The size of the nanoparticle increases with the increase of electron-beam irradiation time. **(c)** The same graphene sample is subjected to additional 15 min of H_2S treatment for the total of 30 min of H_2S treatment time. No particle can be detected on the spot #1. Scale bar: 2 μm. 32

Figure 2.10. Boundary layer MD models and coordinates. A pre-existing straight crack along **(a)** zigzag and **(b)** armchair edge is embedded in a two-dimensional graphene lattice (green). K_{eff} is effective stress intensity factor. K_I and K_{II} are SIF components specified by opening and shear stress, respectively. φ is the phase angle.[11] 34

Figure 2.11. The crack propagation after initiation in Figure 2.10 under complex mechanical stress. **(a–f)** Zigzag (ZZ) crack models at φ= 0°, 30c, 45°, 60°, 65°, and 90°. **(g–l)** Armchair (AC) crack models at φ= 0°, 26.5°, 30°, 45°, 60°, and 90°, respectively. The angle of crack propagation orienting to primary crack is depicted correspondingly. ZZ crack edges are shown in blue, AC in red.[11] 35

Figure 2.12. Images of crack kinking in graphene lattices (green) after propagation in Figure 2.11. ZZ (blue), or AC (red) edges appear alternatively changing direction of growth.[11] 36

Figure 2.13. SEM images of graphene domains before and after H_2S treatment. Both kinked and straight cracks can be visualized with formation of Cu_2S nanoparticles in the crack regions. Scale bar: 2 μm. 37

Figure 2.14. (a,b) Schematic illustration of representative kinked graphene crack structures. **(c)** Histogram of the distribution of kink angles (θ) for the cracks starting at 90° (± 10°) angle (α) from zigzag edge. **(d)** Histogram of the distribution of kink angles (θ) for the cracks starting at 60° (± 10°) or 120° (± 10°) angle (α) from zigzag edge..... 38

Figure 2.15. SEM images of graphene domains before and after H_2S treatment. **(a,b)** Crack initiates from domain center. **(c,d)** A group of cracks with main crack lines orienting roughly along the zigzag direction. One straight continuous crack (indicated by green arrow) is immediately followed by discontinuous crack (indicated by orange arrow) along the same direction. Other cracks display varying degrees of branched structures. Some graphene cracks exhibit snowflake-like branched structures (indicated by purple arrows). Scale bar: 3 µm. 40

Figure 2.16. SEM images of graphene domains before **(a,c)** and after **(b,d)** H_2S treatment. Two cracks originate from domain center, resembling hour and minute hands in a clock. Scale bar: 2 µm. 41

Figure 2.17. SEM images of graphene domains before **(a,c)** and after **(b,d)** H_2S treatment. **(b-d)** Discontinuous cracks highlighted by orange dashed lines. Scale bar: 3 µm. 42

Figure 2.18. EDX spectrum (right) of a pre-existing nanoparticle in polycrystalline graphene film before the H_2S treatment. Electron beam was focused on the center of the nanoparticle (indicated by the green arrow) in the SEM image (left). Scale bar: 0.5 µm. 44

Figure 2.19. SEM images of polycrystalline graphene films on copper foil before and after H_2S gas treatment. **(a,b)** Cu_2S nanoparticles emerge from both SiO_x nanoparticle sites (indicated by blue arrows) and non-SiO_x regions after H_2S treatment. **(c,d)** Cu_2S nanoparticles are formed on the copper grain boundary. **(e,f)** Numerous cracks and hole defects are visualized in a defective graphene film region on multiple copper grains after H_2S gas treatment. Majority of graphene cracks are oriented roughly along the same direction within the same copper grain, but different copper grains lead to different orientation of graphene cracks. Cu_2S nanoparticles are also formed on some copper grain boundaries. **(g,h)** Discontinuous cracks highlighted by orange dashed lines. Pre-existing SiO_x nanoparticle sites are indicated by blue arrows. Scale bar for **(a-d)** and **(g,h)**: 1 µm. Scale bar for **(e,f)**: 10 µm. 45

Figure 2.20. SEM images of polycrystalline graphene films on copper foil before and after H_2S gas treatment. **(a,b)** SEM images from Figure 2.14g and h with three highlighted zoom-in regions. **(a-i,b-i)** SEM images from the zoom-in region (i). **(a-ii,b-ii)** SEM images from the zoom-in region (ii). **(a-iii,b-iii)** SEM images from the zoom-in region (iii). Pre-existing SiO_x

nanoparticle sites are indicated by blue arrows. The Cu_2S nanoparticle size analysis was performed in original SEM images using the ImageJ software. Scale bar: 500 nm. 49

Figure 2.21. (a) Void growth. **(b-e)** Modes of void coalescence: **(b)** Necking of intervoid ligament **(c-d)** Coalescence in a microshear band. **(e)** "Necklace" coalescence.[21] 50

Figure 2.22. SEM images of graphene domains before treatment (0 min) and after repeated H_2S treatment. The total amount of H_2S treatment time is denoted in each SEM image. **(a-e)** No Cu_2S nanoparticle formation after repeated treatments. **(f-k)** The size of the Cu_2S nanoparticle formed at the nucleation center of domain increases with reaction time. **(l-n)** The Cu_2S nanoparticle emerges from a pre-existing impurity nanoparticle at the center and grows much larger with additional reaction time. In addition, a large straight crack is easily visible even before the H_2S treatment. Scale bar: 2 μm. 53

Figure 2.23. SEM images of graphene domains before treatment (0 min) and after repeated H_2S treatment. The total amount of H_2S treatment time is denoted in each SEM image. Multiple Cu_2S nanoparticles are formed in each graphene domain. Although the sizes of the Cu_2S nanoparticles generally increase with reaction time, some Cu_2S nanoparticles grow much faster than others within the same graphene domain. The different growth rates may originate from either the difference in vacancy defect sizes, or tight or loose binding of pre-existing SiO_x nanoparticles with surrounding defective graphene. Scale bar: 2 μm. 54

Figure 2.24. SEM images of graphene domains before treatment (0 min) and after repeated H_2S treatment. The total amount of H_2S treatment time is denoted in each SEM image. Both kinked and straight cracks can be visualized with formation of Cu_2S nanoparticles in the crack regions. The reaction time-dependent study shows that Cu_2S nanoparticles form rapidly and occupy all of cracked areas within 15 min of H_2S treatment. Further chemical treatment does not change the lengths of 1D Cu_2S nanowires, only increases their widths slightly. Scale bar: 2 μm. 55

Figure 2.25. SEM images of graphene domains before treatment (0 min) and after repeated H_2S treatment. The total amount of H_2S treatment time is denoted in each SEM image. Both kinked and straight cracks can be visualized with formation of Cu_2S nanoparticles in the crack regions. The reaction time-dependent study shows that Cu_2S nanoparticles form rapidly and occupy all of cracked areas within 15 min of H_2S treatment. Further chemical treatment does not change the lengths of 1D Cu_2S nanowires, only increases their widths slightly. Scale bar: 2 μm. 56

Figure 2.26. SEM images of graphene domains before treatment (0 min) and after repeated H_2S treatment. The total amount of H_2S treatment time is denoted in each SEM image.

Cracks can be visualized with formation of Cu_2S nanoparticles in the crack regions. **(a-c)** Two cracks originate from domain center, resembling hour and minute hands in a clock. **(d-h)** Branched cracks. Scale bar: 2 µm. 57

Figure 2.27. Representative Raman spectra of the monolayer graphene domain transferred onto Si wafer. **(a,b)** Microscopic optical images of the graphene domain on Si wafer and the green dots showing the first and second spots where the Raman spectra were taken, respectively. Scale bar: 2 µm. **(c)** Raman spectra on the same region of the first spot in the same graphene domain on Si wafer before (bottom) and after (top) 15 min of H_2S treatment. **(d)** Raman spectra on the same region of the second spot in the same graphene domain on Si wafer before (bottom) and after (top) 15 min of H_2S treatment. There is little change of Raman features of monolayer graphene after H_2S treatment. 58

Figure 2.28. SEM images of graphene domains before treatment (0 min) and after 15 min of H_2S treatment using the minimum amount of H_2S gas produced *in situ*, corresponding to 0.02 mg of H_2S/cm^2 of graphene. A Cu_2S nanoparticle appears at the nucleation center of each of two graphene domains, respectively. In addition, the exposed copper substrate outside the graphene domain is fully covered with numerous Cu_2S nanoparticles, suggesting 0.02 mg of H_2S/cm^2 of graphene is sufficient for chemical probing of graphene vacancy defects. Scale bar: 0.5 µm. 59

Figure 3.1. The orientation relationship between copper step bunches (copper surface stripes) and graphene wrinkles. **(a)** SEM and **(b)** Electron back scattering diffraction (EBSD) images of graphene grown on polycrystalline Cu foil. The red, yellow, and white arrows show Cu step bunches, graphene wrinkles, and graphene adlayers, respectively. **(c)** SEM image of a graphene wrinkle, showing graphene wrinkle and copper step bunches are nearly perpendicular to each other. **(d)** AFM image of a graphene wrinkle. Inset shows the height profile along the white line. (e) Illustration of ultraflat graphene on Cu with a premelting layer. (f) Illustration of the corrugation process during cooling. The black and red arrows indicate the buckling of graphene and the surface roughening of Cu, respectively.[3] 67

Figure 3. 2. (a) Steps of a reaction on a graphene sheet. (b) Pyramidalization: the π orbital and three σ bonds describe pyramidalization.[11] 68

Figure 3.3. Illustrations of simple ripple, standing collapsed wrinkle and folded wrinkle on graphene grown by chemical vapor deposition. 70

Figure 3.4. (a) SEM image of monolayer graphene on copper film. The subtle surface features such as graphene wrinkles are not obvious. **(b)** SEM-BSE image of the same region in **(a)**. The graphene wrinkles that are not visible or partially visible in **(a)** are obvious.[19] 71

Figure 3. 5. (a) An SEM image of the graphene on copper surface after dipping in an aqueous HCl solution for 10 minutes. **(b)** BSE mode image of the same region in (a). Blue and red arrows indicate wrinkles in the images.[19] 72

Figure 3.6. SEM and SEM-BSE images graphene on copper samples before H_2S gas treatment and SEM images after 15 minutes of H_2S gas treatment. **(a,d,g,j)** SEM images of polycrystalline graphene on copper before H_2S treatment. The white arrows indicate large wrinkles or larger parts of the wrinkles. **(b,e,h,k)** SEM-BSE images of the approximately same region in **(a,d,g,j)** before H_2S treatment. The smaller-width wrinkles are better visible in SEM-BSE images which are not obvious in SEM images in **(a,d,g,j)**. **(c,f,i,l)** SEM images of the approximately same region after 15 minutes of H_2S treatment. The blue arrows show areas that new particles formed on the wrinkles. The orange arrows show new particles formed not on the wrinkles. The thinner lines, that are smaller-width wrinkles, are the preferred locations for the formation of Cu_2S particles. Scale bar: 2 µm. 76

Figure 3.7. SEM and SEM-BSE images graphene on copper samples before H_2S treatment and SEM images after 15 minutes of H_2S gas treatment. **(a,d)** SEM images of polycrystalline graphene on copper before H_2S treatment. **(b,e)** SEM-BSE images of the approximately same region in **(a,d,g,j)** before H_2S treatment. **(c,f)** SEM images of the approximately same region after 15 minutes of H_2S treatment. The blue arrows show areas that new particles formed on the dark regions on thinner lines. The dark spots on thinner lines, that are smaller-width wrinkles, are generally the preferred locations for the formation of Cu_2S particles. Scale bar: 2 µm. 77

Figure 3.8. SEM and SEM-BSE image hexagonal graphene domain on copper before H_2S treatment and SEM image after 15 minutes of H_2S gas treatment. **(a)** SEM image of hexagonal graphene domain on copper before H_2S treatment. The wrinkles are not visible. **(b)** SEM-BSE image of the same region in **(a)**. The white arrows indicate graphene wrinkles. **(c)** SEM image of the same region in **(a,b)** after 15 minutes of H_2S treatment. There is no discontinuous crack, but particle formation at vacancy defect locations which are indicated by orange arrows. Scale bar: 1 µm. 79

Figure 3.9. SEM and SEM-BSE images hexagonal graphene domains on copper before H_2S treatment and SEM images after 15 minutes of H_2S gas treatment. **(a,d)** SEM images of hexagonal graphene domains on copper before H_2S treatment. **(b,e)** SEM-BSE images of the same regions in (a,d). There is no wrinkle observed. **(c,f)** SEM images of the same region in **(a-e)** after 15 minutes of H_2S treatment. There are particles formed on discontinuous defects which is indicated by orange arrows. Scale bar: 1 µm. 80

Figure 3.10. SEM and SEM-BSE images of hexagonal graphene domains on copper before H_2S treatment and SEM image after 15 minutes of H_2S treatment. **(a,d)** SEM images of hexagonal graphene domains on copper before H_2S treatment. The wrinkles are not visible. **(b,e)** SEM-BSE images of the same graphene domains in **(a,d)**. The white arrows indicate graphene wrinkles. **(c,f)** SEM images of the same graphene domains in **(a,d)** after 15 minutes of H_2S treatment. There is no particle formation on wrinkles but on the other regions which is indicated by blue arrows. Scale bar: 1 μm. 81

Figure 4.1. Illustration of atom arrangement of monolayer triangular h-BN domain. 88

Figure 4.2. Schematic illustration of the atomic configuration for merging between triangular h-BN domains that have different orientations. 89

Figure 4.3. SEM images of CVD grown h-BN on copper foil. **(a)** Low-magnification SEM image of a continuous monolayer h-BN. The yellow arrow indicates one of the h-BN wrinkles. **(b)** Higher magnification image, showing triangular multilayer pyramidal h-BN islands (some of which indicated with red triangles) on monolayer h-BN.[25] 90

Figure 4.4. Photo pictures of the experimental steps for H_2S treatment for h-BN on copper. **(a)** A piece of h-BN on copper is cut from commercially bought h-BN on copper foil. **(b)** h-BN on copper foil is placed on an SEM stub and held in place with the screw holders for initial SEM imaging. **(c)** After initial SEM, the piece is placed in a 4 mL vial. **(d)** 4 mL vial with the h-BN on copper piece is placed in a 20 mL vial. The 20 mL vial is charged with reagents for the treatment. **(e)** After the treatment and 24 hours vacuum, h-BN on copper piece is placed on the SEM stub for a second imaging after the treatment. Scale bar: 0.5 cm. 94

Figure 4.5. SEM images of CVD grown h-BN on copper foil. **(a)** Low-magnification image, showing excessive multilayers of h-BN in monolayer h-BN. The white arrows show the wrinkles on h-BN. **(b)** High-magnification image in the same region, showing triangular adlayer and multilayer pyramidal h-BN island on monolayer h-BN. Scale bar: **(a)** 2 μm and **(b)** 0.2 μm. 95

Figure 4.6. EDX spectra of pristine h-BN on copper. **(a)** SEM image of monolayer h-BN on copper with a triangular multilayer region. The scale bar: 0.2 μm. **(b,c,d)** EDX spectra of spots indicated as **(i)**, **(ii)** and **(iii)** in **(a)** in order, respectively. **(e)** Bar graph for atomic percentage of nitrogen in regions i, ii and iii in **(a)**. 96

Figure 4.7. EDX spectra of h-BN on copper after H_2S gas treatment for 2 minutes. **(a)** SEM image of monolayer h-BN on copper with newly formed particles. The scale bar: 0.5 μm. **(b,c,d)** EDX spectra of spots indicated as **(i)**, **(ii)** and **(iii)** in **(a)** in order, respectively. **(e)**

Table showing the elemental composition of the analyzed spots in (a) by atomic percentage. **(f)** Bar graph for atomic percentage of nitrogen in regions i, ii and iii in (a). 98

Figure 4.8. SEM images of monolayer h-BN on copper foil before and after H_2S gas treatment. **(a,b)** SEM images of the same region before and after 2 min treatment. **(c,d)** The higher magnification images of the upper-middle region in **(a)**. **(e,f)** SEM images of another region before and after 1 min H_2S gas treatment. Scale bar: 0.5 μm. 100

Figure 4.9. HRTEM image of CVD-grown h-BN with vacancy defects at the grain boundary region indicated by green arrows.[33] 101
Figure 4.10. SEM images of monolayer h-BN on copper foil before and after 2 minutes of H_2S gas treatment. Scale bar: 2 μm. 102

Figure 4.11. SEM images of monolayer h-BN on copper foil before **(a,c,e)** and after **(b,d,f)** H_2S gas treatment. The treatment time is noted on each image. The blue arrows indicate triangular multilayer regions and orange arrows indicate thin or irregular shaped bright regions in **(a,c,e)**, where Cu_xS particle formation is observed. Scale bar: 0.5 μm. 104

Figure 4.12. SEM images of monolayer h-BN on copper foil before and after H_2S gas treatment. **(a,b)** SEM images of the same region before and after 2 min treatment, respectively. **(c,d)** The higher magnification images of the upper-right region in **(a)**. Scale bar: 0.2 μm. 105

ACKNOWLEDGEMENTS

This PhD degree would not have been possible without the support and guidance of many people. First, I would like to express my appreciation to my advisor, Dr. Jian Chen, for his guidance, instruction, and advice throughout my PhD studies in his research group. His ideas, thoughts, and work ethic have been integral to my professional development. I would like to thank my committee members Dr. James Cook, Dr. Mark Dietz, Dr. Guilherme Indig, and Dr. Alan Schwabacher for their time, valuable feedback, and advice.

I am grateful to Dr. Ryan R. Kohlmeyer, the former member of the Chen group, for his tutorial and willingness to help in my initial steps of research in this group. I would like to acknowledge Dr. Heather Owen for her help and instruction on SEM. She always had time and patience to answer my technical questions in the microscopy lab. Thank you to all current members of the Chen group Adebola Oyefusi, and Milad Momtaz and recent graduate Seyedali Banisadr.

Finally, I would like to sincerely acknowledge my parents for their continuous support throughout my life. I would like to thank to my siblings Yuksel Altan and Ilhan Altan for their support. I would like to thank my wife, Ashley Jenkins Altan, for her love, understanding, support. I am grateful for her patience throughout my graduate studies.

Chapter 1: Introduction

1.1. Graphene

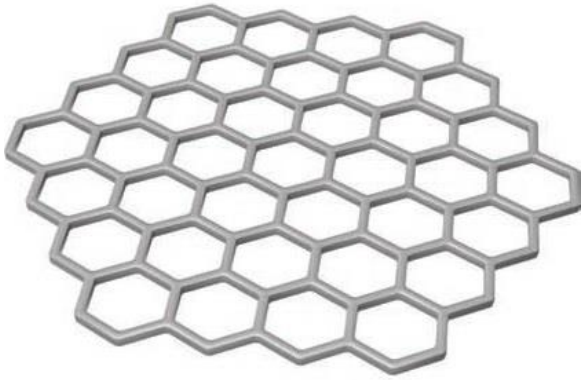

Figure 1.1. Graphene, a single layer of carbon atoms in a honeycomb lattice.[1]

Graphene is a single atomic layer of sp^2-hybridized carbon atoms in hexagonal lattice structure.[2] In graphene, each carbon atom is bonded to three other carbon atoms with 120° in-plane bonding angles with perfect symmetry.[3] This two-dimensional carbon allotrope has attracted a tremendous interest since its first isolation by mechanical exfoliation from graphite flakes which is also widely known as 'scotch tape method' due to its remarkable mechanical, thermal, electrical and optoelectronic properties.[4-5] Graphene has Young's modulus around 1 TPa and its mechanical strength is more than 100 GPa which makes it attractive for nanomechanical systems and membrane applications such as water desalination with improved permeance and robustness.[6-9] Its high thermal conductivity, 5000 $W\ m^{-1}\ K^{-1}$, is useful for applications in which thermal management is needed.[10-11] Together with high mechanical strength and thermal conductivity, its atomically smooth surface make graphene applicable to tribological systems as solid lubricant.[12] Graphene also possess high intrinsic charge mobility of 250 000 $cm^2\ V^{-1}\ s^{-1}$, resulting in intrinsic resistivity as low as 30 Ω/sq, optical transmittance

of 97.7%, and very high surface area of up to 2,630 m^2 g^{-1} which is very desirable for energy storage, batteries, transistors and optoelectronic devices.[4,6,10,13,14] Graphene's chemical inertness and flexibility in out-of-plane direction is highly sought after for devices such as bendable or curved solar cells and displays with long lifetime.[4,6] Due to change in electrical conductivity of graphene with adsorption of molecules on its surface, graphene is also a promising candidate for sensor applications.[8]

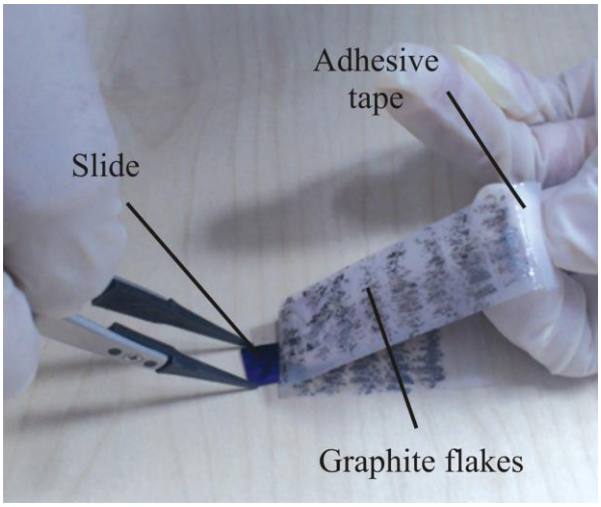

Figure 1.2. Mechanical exfoliation of graphene from graphite flakes, 'scotch tape method'.[4]

Mechanical exfoliation of graphene from graphite flakes provides highest quality but small area graphene in submillimeter scale.[1,4] The mechanical exfoliation method requires tedious repetition of stick and peel cycles with an adhesive tape, and then search for monolayer graphene among numerous multilayer graphene pieces under the optical microscope.[15] It also suffers from dependency on the experimentalist.[16] While this method provides the best quality samples for researchers, it seems to be not applicable for large scale production of graphene and graphene devices due to the necessity of large area and uniform monolayer graphene.[17]

1.2. Chemical Vapor Deposition (CVD) Graphene

Chemical vapor deposition method is a promising bottom-up technique for large area and scalable graphene production. CVD grown graphene can be transferred onto desired substrates due to weak interaction with the metal substrate on which it is grown.[2] It has been demonstrated that 30 inch sized graphene can be produced and transferred by roll-to-toll based techniques.[18] A typical CVD process involves annealing of a metal substrate under H_2/Ar gas flow at high temperature, around 1000 °C, and then introduction of a hydrocarbon resource into the growth chamber such as methane. The metal substrate catalyzes the dehydrogenation of the hydrocarbon molecules so that carbon atoms dissolve in the metal surface. Then, diffused carbon atoms start to nucleate and form graphene domains on multiple sites on the metal surface (Figure 1.1). The preferred nucleation sites on metal, also called as active sites, can be impurity locations, grain boundaries and surface defects.[19] Subsequently, growing adjacent domains coalesce and thus form continuous polycrystalline monolayer graphene covering the metal surface. [20-21]

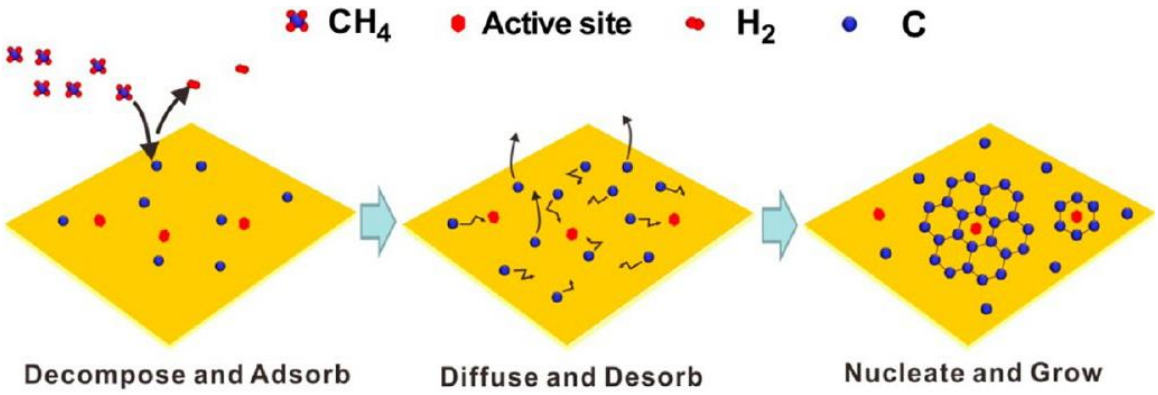

Figure 1.3. Illustration of the graphene growth mechanism on copper in CVD process, as divided into three main steps.[19]

Methane is the mostly preferred precursor in CVD process, whereas it is possible to produce graphene from various carbon resources which are gas or solid.[4,22] The solubility of carbon in the metal is one of the important factors affecting monolayer graphene formation. In case of high solubility of carbon in the metal such as Ni, upon cooling, carbon atoms precipitate and form multilayer graphene on the surface. In the case of low solubility of carbon in the metal such as Cu, predominantly monolayer graphene formation is favored due to a self-limiting effect.[2,23] Researchers have been able to produce graphene on various substrates such as Ni, Pd, Ru, Rh, Ir, Pt, Cu, Co and Ge by CVD.[24-25] Commercially available copper foils are mostly used for monolayer graphene production by CVD due to low cost and likelihood of large area monolayer coverage.[26] The graphene growth by CVD method on copper foils results in graphene formation with inferior quality compared to mechanical exfoliation method. This can be caused by the topology change of Cu surface during CVD process due to evaporation of surface Cu atoms at temperatures nearing its melting point, polycrystalline structure of copper foil with various orientation of its crystallographic grains and presence of grain boundaries.[25] Moreover, during graphene growth copper grains evolve and are far from being fixed geometry and orientation.[27] Beside copper surface topology and crystalline structure, used H_2/Ar/CH_4 gas ratio, pressure and temperature in the growth chamber, gas flow direction and the location of the copper foil inside the chamber effect the nucleation, shape and orientation of graphene domains, thus overall quality of produced polycrystalline graphene film.[21,28-29]

1.3. Defects in CVD-grown graphene

CVD method yields larger area, but lower quality graphene compared to mechanically exfoliated graphene due to existence of a variety of defects. Structural defects often have negative effects on graphene's phenomenal physical properties such as reduced mechanical

strength, thermal conductivity, electrical conductivity, and impermeability and etc.[3,14,30] However, in some applications defects can be deliberately introduced by, for instance, irradiation or chemical treatments and exploited to alter the intrinsic physical properties of graphene for target applications.[30] For example, CVD-grow graphene with engineered nanopores is ideal for next generation membrane applications with high selectivity and permeability.[9,31] Being a two-dimensional material, graphene has limited number of possible types of defects compared to bulk materials.[30] Defects in three-dimensional crystals are regarded as intrinsic defects when the crystalline order is disrupted without the presence of atoms of another element and as extrinsic defects with the presence of foreign atoms, impurities.[30] Possible intrinsic defects for CVD-grown graphene are line defects such as grain boundaries (GBs) and wrinkles, hole defects and microcracks which are created during synthesis or processing.[14]

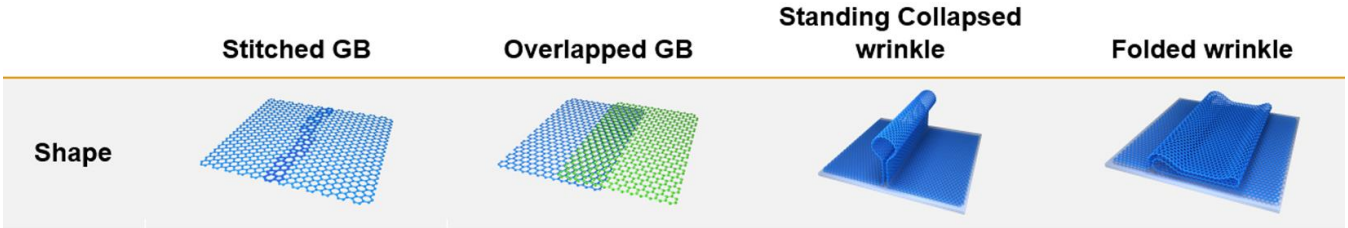

Figure 1.4. Shapes of the line defects in CVD-grown graphene.[32]

CVD method produces polycrystalline graphene due to formation of numerous graphene domains ubiquitously on the metal substrate.[33] During the growth, neighboring graphene grains are stitched together by forming disordered grain boundaries.[34] In addition, neighboring graphene grains can overlap instead of stitching (Figure 1.4).[13,33,35] However, it is also possible that different graphene grains can perfectly merge without forming grain boundaries in the case of having the same crystallographic orientations.[36] Accordingly, grain boundaries cause

electrical and mechanical performance of CVD-grown graphene to be inferior to the exfoliated graphene.[34] Beside GBs, wrinkles are the other type of line defects that is widely observed in graphene produced by CVD. The wrinkles are caused by the thermal expansion coefficient difference between graphene and the copper substrate.[34] The two types of wrinkles are shown in Figure 1.4, as standing collapsed wrinkle and folded wrinkle. In case of missing carbon atoms in the lattice, graphene hole defects are observed (Figure 1.5).[37]

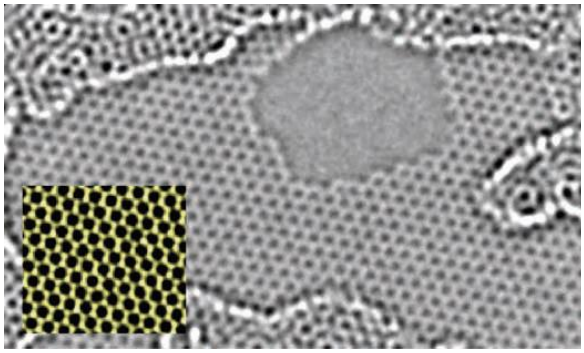

Figure 1.5. Aberration-corrected TEM image of a hole in a single layer of graphene. Scale bar: 5 Å.[37]

It is utmost importance to characterize and control various structural defects in CVD-grown graphene to realize its influential potential for real-world applications.[38] Since CVD-grown graphene, in theory, can be as large as the size of available copper foil on which it grows, it is necessary to have an analytical tool or method for large area graphene defect characterization.

1.4. Observation of structural defects in CVD-grown graphene

Keeping in mind that the highest quality graphene is single crystalline graphene without grain boundaries, hole defects or cracks, and impurities, it is important to be able to characterize large area graphene. Raman spectroscopy is a very informative technique for the graphene characterization such as to identify number of layers and the presence of defects.[39] Moreover,

Raman mapping can be used to image graphene defective sites and grain boundaries (Figure 1.6).[40]

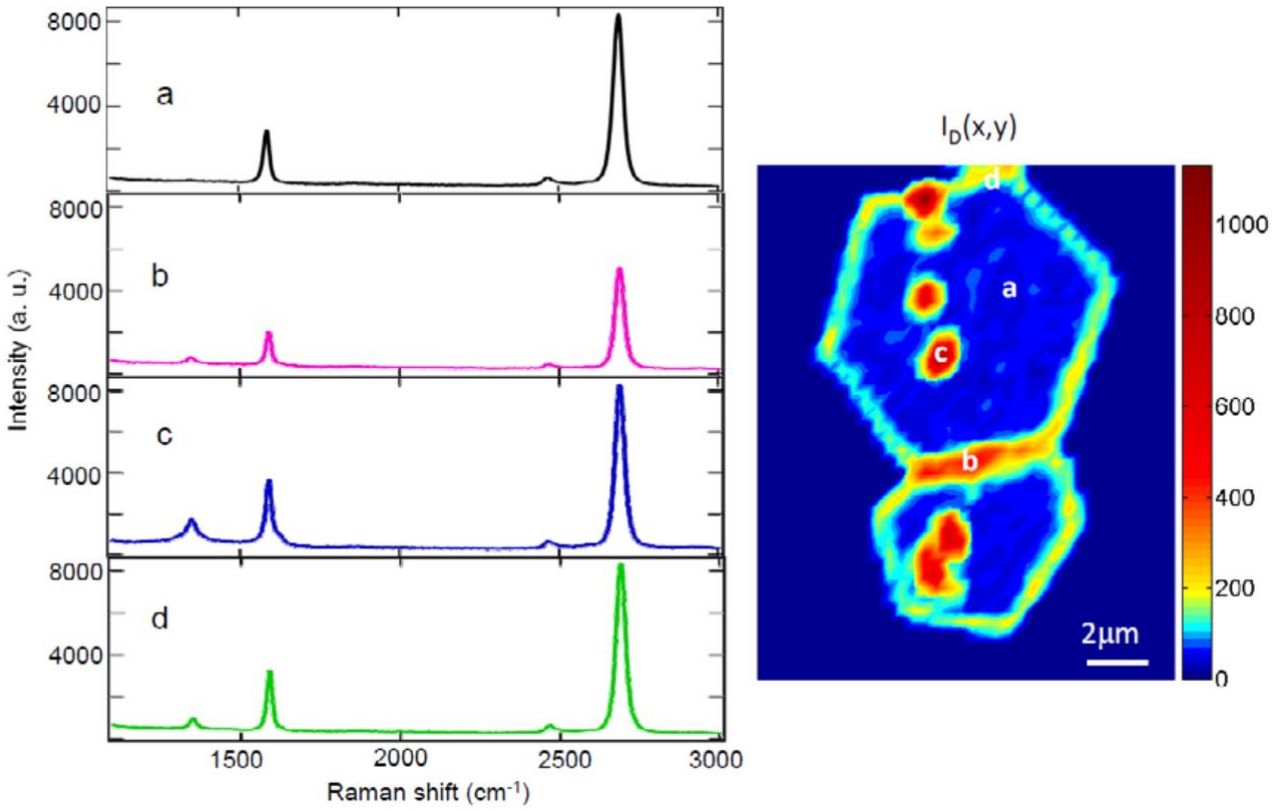

Figure 1.6. Individual Raman spectra taken from 4 representative locations on graphene (left). Spectroscopic Raman mapping of graphene grains and grain boundary (right). (a) inside a single crystalline graphene grain, (b) on the grain boundary location, (c) on a defect site, which could be a nucleation center, inside an individual grain, and (d) on the edge of graphene.[40]

However, Raman mapping often requires the transfer of graphene and suffers from low resolution as well as being time-consuming.[41] Tremendous progress has been made in imaging of structural defects in graphene at atomic level by using high-resolution transmission electron microscopy (HRTEM) and scanning tunneling microscopy (STM).[7,33,42-43] Nowadays, the resolution limits of TEM systems can be as low as 0.05 nm with aberration correction.[44]

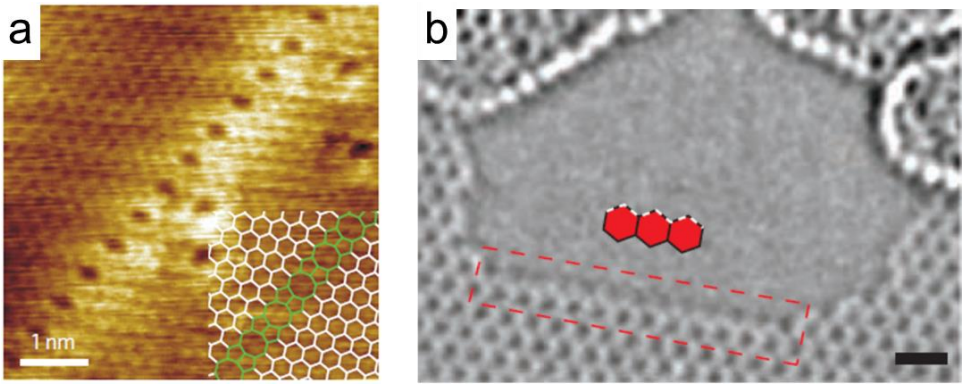

Figure 1.7. (a) STM image of a grain boundary in graphene. Scale bar: 1 nm.[33] **(b)** Aberration corrected TEM image of a hole in a single layer of graphene. Scale bar: 5 Å.[37]

While STM and HRTEM provides high resolution imaging of graphene samples and allows observation of various defects, they have a number of drawbacks (Figure 1.7). These techniques are time-consuming and often require complex sample preparation. Moreover, a very limited area of graphene samples can be surveyed.[14,45] In order to evaluate the quality of produced graphene, it is important to be quickly able to observe spatial distribution of structural defects over a large area of graphene samples. Also, this allow us to investigate and study the origins of defect formation and the control of defect density. A number of techniques have been developed to visualize the distribution of grain boundaries in polycrystalline graphene such as polarized optical microscopy of liquid crystal-coated graphene, infrared nano-imaging, nanoparticle deposition, radical oxidation under ultraviolet irradiation, and air oxidation at 200-250 °C.[46-52]

Beside graphene grain boundaries, nanoscale vacancy defects such as hole defects and cracks are well known to have significant effects on graphene's properties. Though, relatively less research has been devoted for fast probing of the distribution of these nanoscale vacancy defects. Cracks with large width sometimes can be imaged with optical microscopy or scanning

electron microscopy (SEM), whereas finer cracks are more difficult to detect reliably using the same techniques.[53]

1.4.1. Nanoparticle deposition

A number of methods have been developed in the literature to visualize the structural defects by using nanoparticle deposition on CVD-grown graphene.[32,49,54] One of the most common techniques used for nanoparticle deposition on graphene is atomic layer deposition (ALD).

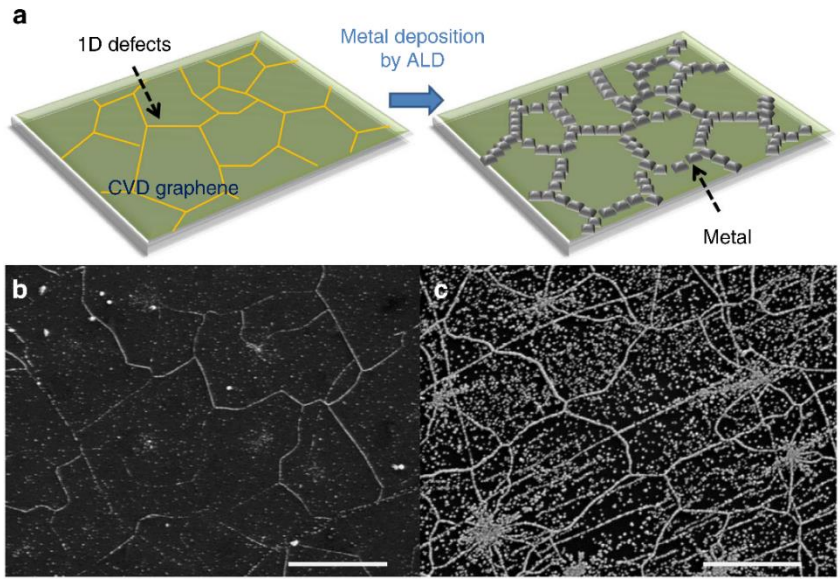

Figure 1.8. Visualization of one-dimensional defects in CVD-grown graphene by ALD. **(a)** Schematic of selective Pt growth on various line defects such as grain boundaries, cracks and folded structures in CVD graphene. **(b)** SEM image of graphene on a glass substrate after 500 ALD cycles of Pt deposition. **(c)** SEM image of graphene with Pt deposition after 1000 ALD cycles. Scale bar: 2 μm.[49]

ALD is a chemical vapor deposition technique (CVD) which allows deposition of atoms layer by layer on the growth substrate with high quality and uniformity.[55] In ALD, the substrate is exposed to pulses of precursors and then co-reactants in repeated cycles. A purge or pump step is applied between each pulse. ALD on graphene is based on the idea that while defect-

free graphene would be chemically passive to nanoparticle growth by atomic layer deposition, dangling bonds in defect locations would be preferential locations for nanoparticle growth. Therefore, defects can be visualized in graphene by selective deposition of nanoparticles by ALD.[49-50,56] Another method is evaporating a noble metal onto graphene. In this method, gold atoms are deposited on graphene grain boundaries and wrinkles by a thermal evaporator.[32]

However, these methods which depend on nanoparticle deposition on graphene defects are not selective towards types of defects and not able to distinguish between hole defects, grain boundaries, cracks or wrinkles. For example, nanoparticles deposited wrinkles would be confused with grain boundary lines.[45]

1.4.2. Liquid crystal deposition

Liquid crystal molecules can be deposited on the graphene substrate and be allowed to transition from isotropic phase to nematic phase. In transition to the nematic phase, the liquid crystal molecules follow the lattice orientation of the graphene grain that they are on. The molecules on the same graphene domain would have the same direction. Thus, graphene domains and grain boundaries become visible under polarized optical microscope (POM) due to contrast difference caused by various alignment of liquid crystal molecules on the domains of polycrystalline graphene (Figure 1.2).[46-47,57]

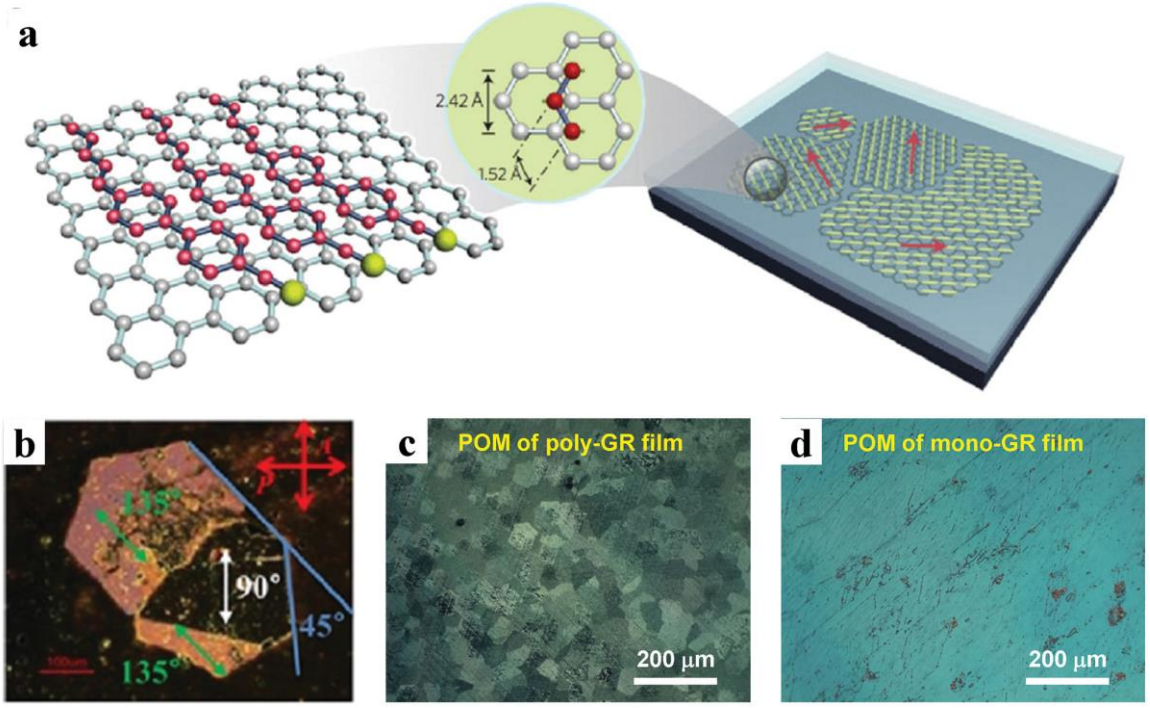

Figure 1.9. (a) Schematic of liquid crystal alignment on the surface of the graphene. The alignment directions of liquid-crystal molecules depend on the orientations of graphene domains. **(b)** POM images of graphene islands coated with liquid-crystal molecules on glass. **(c,d)** POM images of polycrystalline and monocrystalline graphene films coated with liquid-crystal molecules on a Cu substrate, respectively.[45]

The liquid crystalline deposition technique allows one to visualize graphene grain boundaries under POM in relatively large area and gives information on the grain boundaries and polycrystallinity of the graphene. Nevertheless, in the case of existing graphene grain boundary between graphene domains with the same orientation, this method is not able to indicate graphene grain boundaries due to no change in the orientation direction of the liquid crystalline molecules in different domains.[45] Moreover, this method is not able to detect other types of structural defects such as vacancy defects in graphene.

1.4.3. Oxidation Methods

Graphene grain boundaries can be visualized by selectively oxidizing copper underneath through graphene grain boundaries by the formation of copper oxide lines in CVD-grown

graphene. These lines tend to be larger than the actual width of graphene grain boundaries due to continuous supply of the oxidizing agents thus become visible under optical microscope for an easy observation (Figure 1.3).[45] Oxidation can be performed by using air heating at 200-250 °C or by creating radicals under ultraviolet irradiation in humid air environment or by partially immersing graphene on copper sample in an electrolyte solution.[58]

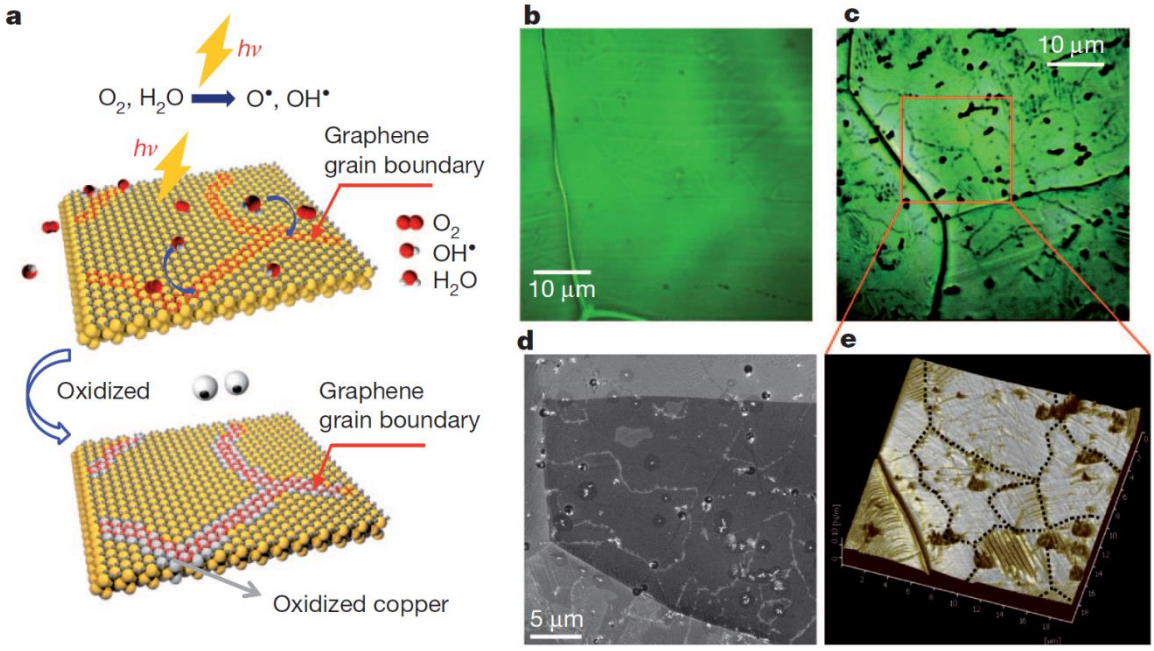

Figure 1.10. Observation of graphene grain boundaries after ultraviolet exposure under moisture-rich ambient conditions. **(a)** Schematic of the ultraviolet treatment of a graphene on copper sample. **(b,c)** Optical images of graphene on copper before **(b)** and after **(c)** oxidation. **(d)** SEM image of oxidized graphene on copper. **(e)** AFM image of the location marked by a red square in **(c)**.[51]

The main disadvantage of these oxidation methods is the use of radicals that can create new structural defects and damage graphene samples. Thus, it becomes impossible to distinguish the original defects and newly created ones with the application of these methods.

1.4.4. Under-etching Method

The under-etching method is developed to make graphene hole defects visible by using an oxidative copper etchant such as $FeCl_3$ or $(NH_4)_2S_2O_8$ on CVD-grown graphene. The basic idea is that graphene would have a barrier role between copper etchant solution and copper substrate while the etchant can only access copper through holes of graphene. Thus, hole defects in graphene could be visualized by the formation of etch pits in the underlying copper only at graphene hole defect sites (Figure 1.4).[31,59-60]

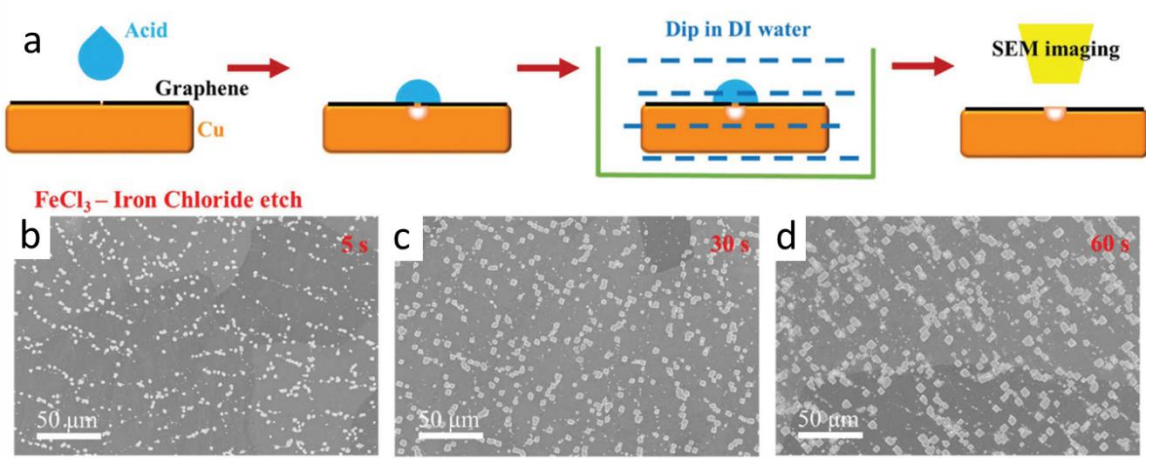

Figure 1.11. (a) Schematic illustration of the under-etching process for CVD-grown graphene on copper foil. SEM images showing the etch pits formed after iron chloride solution etch for **(b)** 5 s, **(c)** 30 s, **(d)** 60 s.[60]

Nevertheless, in under-etching method, it was found that the etch pit size increases while etch pit density decreases with increasing etching time.[60] This indicates the coalescence of initial small etch pits to form larger etch pits. Consequently, the pits visualized may not be reflection of original individual hole defects of the graphene, but multiples of them. The exposure of the graphene sample to the oxidative chemicals may create new defects on graphene. In addition, the direct exposure of a monolayer graphene film to various liquids during the etching and washing steps may result in new graphene defects due to the surface tension and etc.

Other methods such as Raman mapping and the interference reflection microscopy have been used to visualize graphene defects on SiO_2/Si substrates and transparent substrates, respectively.[61-62] However, the graphene transfer process may create new defects such as tears.[63] As a result, the observed defects may not be the original defects before the transfer of the graphene sample.

Therefore, it is important to develop a method to selectively probe vacancy defects such as hole defects and cracks in CVD-grown graphene without creating new ones. In the next chapter, we report a new method for *in situ* chemical probing of hole defects and cracks in CVD-grown graphene.

1.5. References

(1) Weiss, N. O.; Zhou, H.; Liao, L.; Liu, Y.; Jiang, S.; Huang, Y.; Duan, X., *Adv. Mater.,* **2012***,* 24, 5782-5825.

(2) Li, X.; Cai, W.; An, J.; Kim, S.; Nah, J.; Yang, D.; Piner, R.; Velamakanni, A.; Jung, I.; Tutuc, E.; Banerjee, S. K.; Colombo, L.; Ruoff, R. S., *Science*, **2009***,* 324, 1312-1314.

(3) Vicarelli, L.; Heerema, S. J.; Dekker, C.; Zandbergen, H. W., *ACS Nano*, **2015***,* 9, 3428-3435.

(4) Song, Y.; Fang, W.; Brenes, R.; Kong, J., *Nano Today*, **2015***,* 10, 681-700.

(5) Randviir, E. P.; Brownson, D. A. C.; Banks, C. E., *Mater. Today*, **2014***,* 17, 426-432.

(6) Kidambi, P. R.; Terry, R. A.; Wang, L.; Boutilier, M. S. H.; Jang, D.; Kong, J.; Karnik, R., *Nanoscale*, **2017***,* 9, 8496-8507.

(7) Kim, K.; Artyukhov, V. I.; Regan, W.; Liu, Y.; Crommie, M. F.; Yakobson, B. I.; Zettl, A., *Nano Lett.*, **2012***,* 12, 293-297.

(8) Zhu, Y.; Murali, S.; Cai, W.; Li, X.; Suk, J. W.; Potts, J. R.; Ruoff, R. S., *Adv. Mater.*, **2010***,* 22, 3906-3924.

(9) Cohen-Tanugi, D.; Grossman, J. C., *Nano Lett.*, **2012***,* 12, 3602-3608.

(10) Lee, H. C.; Liu, W.; Chai, S.; Mohamed, A. R.; Aziz, A.; Khe, C.; Hidayah, N. M. S.; Hashim, U., *RSC Advances*, **2017***,* 7, 15644-15693.

(11) Preston, D. J.; Mafra, D. L.; Miljkovic, N.; Kong, J.; Wang, E. N., *Nano Lett*., **2015***,* 15, 2902-2909.

(12) Berman, D.; Erdemir, A.; Sumant, A. V., *Mater Today*, **2014***,* 17, 31-42.

(13) El-Kady, M. F.; Shao, Y.; Kaner, R. B., *Nat. Rev. Mater.*, **2016***,* 1, 1-14.

(14) Lee, S.; Kim, J.; Ahn, J., *Mater Today*, **2015***,* 18, 336-344.

(15) Yang, Y.; Kaner, R. B.; Tung, V. C.; Allen, M. J., *Nat. Nanotechnol*., **2009***,* 4, 25-29.

(16) Yuan, L.; Ge, J.; Peng, X.; Zhang, Q.; Wu, Z.; Jian, Y.; Xiong, X.; Yin, H.; Han, J., *AIP Advances*, **2016***,* 6, 125201.

(17) Yi, M.; Shen, Z., *J. Mater. Chem. A*, **2015***,* 3, 11700–11715.

(18) Xu, X.; Bae, S.; Hong, B. H.; Ri Kim, H.; Ahn, J.; Zheng, Y.; Kim, H.; Song, Y. I.; Iijima, S.; Kim, K. S.; Lei, T.; Balakrishnan, J.; Park, J.; Kim, Y.; Lee, Y.; Özyilmaz, B., *Nat. Nanotechnol.,* **2010***,* 5, 574-578.

(19) Yan, Z.; Lin, J.; Peng, Z.; Sun, Z.; Zhu, Y.; Li, L.; Xiang, C.; Samuel, E. L.; Kittrell, C.; Tour, J. M., ACS Nano, **2012***, 6*, 9110-9117.

(20) Iski, E. V.; Yitamben, E. N.; Gao, L.; Guisinger, N. P., *Adv. Funct. Mater.,* **2013***,* 23, 2554-2564.

(21) Yan, Z.; Peng, Z.; Tour, J. M., *Acc. Chem. Res.,* **2014***,* 47, 1327-1337.

(22) Ruan, G.; Sun, Z.; Peng, Z.; Tour, J. M., *ACS Nano*, **2011***,* 5, 7601-7607.

(23) Liu, L.; Zhou, H.; Cheng, R.; Yu, W. J.; Liu, Y.; Chen, Y.; Shaw, J.; Zhong, X.; Huang, Y.; Duan, X., *ACS Nano*, **2012***,* 6, 8241-8249.

(24) Pasternak, I.; Wesolowski, M.; Jozwik, I.; Lukosius, M.; Lupina, G.; Dabrowski, P.; Baranowski, J. M.; Strupinski, W., *Sci. Rep.,* **2016***,* 6, 21773.

(25) Yuan, Q.; Gao, J.; Shu, H.; Zhao, J.; Chen, X.; Ding, F., *J. Am. Chem. Soc*., **2012***,* 134, 2970-2975.

(26) Wood, J. D.; Schmucker, S. W.; Lyons, A. S.; Pop, E.; Lyding, J. W., *Nano Lett*., **2011***,* 11, 4547-4554.

(27) Wu, Y.; Hao, Y.; Jeong, H. Y.; Lee, Z.; Chen, S.; Jiang, W.; Wu, Q.; Piner, R. D.; Kang, J.; Ruoff, R. S., *Adv. Mater*., **2013***,* 25, 6744-6751.

(28) Geng, D.; Wang, H.; Yu, G., *Adv. Mater*., **2015***,* 27, 2821-2837.

(29) Mohsin, A.; Liu, L.; Liu, P.; Deng, W.; Ivanov, I. N.; Li, G.; Dyck, O. E.; Duscher, G.; Dunlap, J. R.; Xiao, K.; Gu, G., *ACS Nano*, **2013***,* 7, 8924-8931.

(30) Banhart, F.; Kotakoski, J.; Krasheninnikov, A. V., *ACS Nano*, **2011***,* 5, 26-41.

(31) O'Hern, S. C.; Stewart, C. A.; Boutilier, M. S.; Idrobo, J. C.; Bhaviripudi, S.; Das, S. K.; Kong, J.; Laoui, T.; Atieh, M.; Karnik, R., *ACS Nano*, **2012***,* 6, 10130-10138.

(32) Yu, S. U.; Park, B.; Cho, Y.; Hyun, S.; Kim, J. K.; Kim, K. S., *ACS Nano*, **2014***,* 8, 8662-8668.

(33) Yazyev, O. V.; Chen, Y. P., *Nat. Nanotechnol*, **2014***,* 9, 755-767.

(34) Long, F.; Yasaei, P.; Sanoj, R.; Yao, W.; Král, P.; Salehi-Khojin, A.; Shahbazian-Yassar, R., *ACS Appl. Mater. Interfaces*, **2016***,* 8, 18360-18366.

(35) Tsen, A. W.; Brown, L.; Levendorf, M. P.; Ghahari, F.; Huang, P. Y.; Havener, R. W.; Ruiz-Vargas, C. S.; Muller, D. A.; Kim, P.; Park, J., Science, **2012***,* 336, 1143-1146.

(36) Nguyen, V. L.; Shin, B. G.; Duong, D. L.; Kim, S. T.; Perello, D.; Lim, Y. J.; Yuan, Q. H.; Ding, F.; Jeong, H. Y.; Shin, H. S.; Lee, S. M.; Chae, S. H.; Vu, Q. A.; Lee, S. H.; Lee, Y. H., *Adv. Mater*., **2015***,* 27, 1376-1382.

(37) Girit, C. O.; Meyer, J. C.; Erni, R.; Rossell, M. D.; Kisielowski, C.; Yang, L.; Park, C. H.; Crommie, M. F.; Cohen, M. L.; Louie, S. G.; Zettl, A., *Science*, **2009***,* 323, 1705-1708.

(38) Deng, B.; Pang, Z.; Chen, S.; Li, X.; Meng, C.; Li, J.; Liu, M.; Wu, J.; Qi, Y.; Dang, W.; Yang, H.; Zhang, Y.; Zhang, J.; Kang, N.; Xu, H.; Fu, Q.; Qiu, X.; Gao, P.; Wei, Y.; Liu, Z.; Peng, H., ACS Nano, **2017***,* 11, 12337-12345.

(39) Berciaud, S.; Ryu, S.; Brus, L. E.; Heinz, T. F., *Nano Lett*., **2009***,* 9, 346-352.

(40) Yu, Q.; Jauregui, L. A.; Wu, W.; Colby, R.; Tian, J.; Su, Z.; Cao, H.; Liu, Z.; Pandey, D.; Wei, D.; Chung, T. F.; Peng, P.; Guisinger, N. P.; Stach, E. A.; Bao, J.; Pei, S. S.; Chen, Y. P., *Nat. Mater*., **2011***,* 10, 443-449.

(41) Cong, C.; Li, K.; Zhang, X. X.; Yu, T., *Sci. Rep*., **2013***,* 3, 1195.

(42) Banhart, F.; Kotakoski, J.; Krasheninnikov, A. V., *ACS Nano*, **2011***,* 5, 26-41.

(43) Huang, P. Y.; Ruiz-Vargas, C. S.; van der Zande, A M; Whitney, W. S.; Levendorf, M. P.; Kevek, J. W.; Garg, S.; Alden, J. S.; Hustedt, C. J.; Zhu, Y.; Park, J.; McEuen, P. L.; Muller, D. A., *Nature*, **2011***,* 469, 389-392.

(44) Luo, C.; Wang, C.; Wu, X.; Zhang, J.; Chu, J., *Small*, **2017***,* 13, 1604259.

(45) Nguyen, V. L.; Lee, Y. H., *Small*, **2015***,* 11, 3512-3528.

(46) Kim, D. W.; Kim, Y. H.; Jeong, H. S.; Jung, H., *Nat. Nanotechnol.,* **2012***,* 7, 29-34.

(47) Jong-ho Son; Seung-jae Baeck; Min-ho Park; Jae-bok Lee; Cheol-woong Yang; Jang-kun Song; Wang-cheol Zin; Jong-hyun Ahn, *Nat. Commun.,* **2014***,* 5, 3484.

(48) Fei, Z.; Rodin, A. S.; Gannett, W.; Dai, S.; Regan, W.; Wagner, M.; Liu, M. K.; McLeod, A. S.; Dominguez, G.; Thiemens, M.; Castro Neto, A. H.; Keilmann, F.; Zettl, A.; Hillenbrand, R.; Fogler, M. M.; Basov, D. N., *Nat. Nanotechnol*, **2013***,* 8, 821-825.

(49) Kim, K.; Lee, H.; Johnson, R. W.; Tanskanen, J. T.; Liu, N.; Kim, M.; Pang, C.; Ahn, C.; Bent, S. F.; Bao, Z., *Nat. Commun*., **2014***, 5*, 4781.

(50) Van Lam, D.; Kim, S. M.; Cho, Y.; Kim, J. H.; Lee, H. J.; Yang, J. M.; Lee, S. M., *Nanoscale*, **2014***,* 6, 5639-5644.

(51) Duong, D. L.; Han, G. H.; Lee, S. M.; Gunes, F.; Kim, E. S.; Kim, S. T.; Kim, H.; Ta, Q. H.; So, K. P.; Yoon, S. J.; Chae, S. J.; Jo, Y. W.; Park, M. H.; Chae, S. H.; Lim, S. C.; Choi, J. Y.; Lee, Y. H., *Nature*, **2012***,* 490, 235-239.

(52) Kalita, G.; Papon, R.; Sharma, S.; Shinde, S. M.; Vishwakarma, R.; Tanemura, M., *Carbon*, **2014***,* 80, 504-512.

(53) Fujihara, M.; Inoue, R.; Kurita, R.; Taniuchi, T.; Motoyui, Y.; Shin, S.; Komori, F.; Maniwa, Y.; Shinohara, H.; Miyata, Y., *ACS Nano*, **2015***,* 9, 9027-9033.

(54) Vervuurt, R. R.; Kessels, W. E.; Bol, A. A., *Adv. Mater. Interfaces*, **2017***,* 4, 1700232.

(55) Vervuurt, R. R.; Karasulu, B. B.; Verheijen, M. M.; Kessels, W. E.; Bol, A. A., *Chem. Mat*., **2017***,* 29, 2090-2100.

(56) Park, K. S.; Kim, S.; Kim, H.; Kwon, D.; Lee, Y. K.; Min, S.; Im, S.; Choi, H. J.; Lim, S.; Shin, H.; Koo, S. M.; Sung, M. M., *Nanoscale*, **2015**, 7, 17702-17709.

(57) Cummings, A. W.; Duong, D. L.; Nguyen, V. L.; Van Tuan, D.; Kotakoski, J.; Barrios Vargas, J. E.; Lee, Y. H.; Roche, S., *Adv. Mater.,* **2014***,* 26, 5079-5094.

(58) Ly, T. H.; Duong, D. L.; Ta, Q. H.; Yao, F.; Vu, Q. A.; Jeong, H. Y.; Chae, S. H.; Lee, Y. H., *Adv. Funct. Mater.*, **2013***,* 23, 5183-5189.

(59) Singha Roy, S.; Jacobberger, R. M.; Wan, C.; Arnold, M. S., *Carbon*, **2016**, 100, 1-6.

(60) Kidambi, P. R.; Terry, R. A.; Wang, L.; Boutilier, M. S. H.; Jang, D.; Kong, J.; Karnik, R., *Nanoscale*, **2017***, 9*, 8496-8507.

(61) Wang, S.; Suzuki, S.; Hibino, H., *Nanoscale*, **2014***,* 6, 13838-13844.

(62) Li, W.; Moon, S.; Wojcik, M.; Xu, K., *Nano Lett*., **2016***,* 16, 5027-5031.

(63) Chen, Y.; Gong, X.; Gai, J., *Adv. Sci*., **2016***,* 3, 1500343.

Chapter 2: *In Situ* Chemical Probing of Hole Defects and Cracks in Graphene at Room Temperature

2.1. Introduction

It is important to develop a method to selectively probe vacancy defects such as hole defects and cracks in CVD-grown graphene without creating new ones. Our approach is based on a solid-gas phase reaction that selectively occurs in graphene vacancy defect sites such as holes and cracks, where the underlying metal catalyst substrate such as copper is exposed to the air and oxidized at room temperature (Figure 2.4). Owing to its small molecular size, which is roughly comparable with O_2, H_2S can penetrate through nanoscale graphene vacancy defects. The reaction between the exposed oxidized copper substrate and H_2S gas at room temperature leads to the formation of Cu_2S nanoparticles, which can be readily imaged by SEM.[1,2] Since H_2S is not an oxidant, it does not oxidize and damage the graphene. Compared with other graphene defects probing techniques, our new probing technique has a unique combination of the following advantages: 1) **No exposure to liquids.** Since the solid-gas phase reaction between the oxidized copper and H_2S gas only produces Cu_2S nanoparticles and trace amount of water vapor (Figure 2.4a), potential liquid-induced damage and contamination of graphene can be avoided. 2) **Non-damaging *in situ* probing.** Our method does not use strong oxidants or heating and does not require the graphene transfer; therefore, it allows for the same-spot *in situ* probing before and after the H_2S treatment while avoiding potential graphene damages caused by the strong oxidants, heating, and graphene transfer. 3) **High selectivity, sensitivity, and reliability towards vacancy defects.** Since the H_2S gas only reacts with the exposed oxidized copper substrate, our approach is highly selective for identifying graphene vacancy defects such as holes and cracks. The Cu_2S nanoparticle size generally increases with

the H_2S treatment time until the reaction completes, which provides an amplifying mechanism to increase the detection sensitivity towards nanoscale graphene vacancy defects. In addition, the unique sulfur signature in the energy-dispersive X-ray spectroscopy (EDX) can be used to distinguish the Cu_2S nanoparticles from other possible nanoparticle contaminants such as C and SiO_x on the CVD-grown graphene surface. The combination of the same-spot probing, amplifying growth of Cu_2S nanoparticles, and unique sulfur signature significantly enhances the reliability of our technique. 4) **Simplicity and scalability.** Our method is very easy to use because it does not involve washing, heating, special chemicals, and graphene transfer. The solid-gas phase reaction is applicable to any sizes of graphene samples. SEM is one of the most convenient and widely accessible nanocharacterization techniques and is suitable for large sample sizes. Therefore, our technique enables the fast probing of the distribution of nanoscale vacancy defects in large area CVD-grown graphene samples. Although this study focuses on the monolayer graphene samples grown on the copper substrate, our approach could be extended to probe 2D materials (graphene, h-BN, etc.) grown on a variety of metal substrates, because H_2S is also known to react with other metals such as nickel, platinum, and silver.

2.2. Experimental

2.2.1. Materials

The CVD-grown monolayer graphene samples on copper foil were purchased from ACS Materials Inc. Sodium sulfide nonahydrate ($Na_2S.9H_2O$) and sulfuric acid (H_2SO_4) (6.00 N) were purchased from MP Biomedicals and Ricca Chemical Company, respectively. The 0.025 mm-thick copper foil was acquired from Alfa Aesar. Ammonium persulfate ($(NH_4)_2S_2O_8$) was

purchased from BDH Chemicals. Sylgard 184 PDMS base and curing agent were supplied from Dow Corning Corporation.

2.2.2. Characterization

SEM imaging and EDX analysis were performed using a Hitachi S-4800 field emission scanning electron microscope equipped with an EDX spectrometer and a back-scattered electron (BSE) detector under high vacuum ($<10^{-3}$ Pa). All SEM and EDX experiments were carried out under the same conditions. An emission current of 10 μA and accelerating voltage of 3.5 keV with a working distance of about 15 mm were used for the EDX experiments. SEM-BSE experiments were performed by using emission current of 10 μA and accelerating voltage of 1 keV with a working distance of about 3 mm. X-ray diffraction (XRD) was performed on Bruker D8 DISCOVER diffractometer with Cu Kα radiation. Raman spectra of the transferred graphene samples were acquired using a Horiba Jobin Yvon Xplora confocal Raman microscope. The wavelength of the excitation laser was 532 nm.

2.2.3. Graphene dry-transfer

Dry transfer method widely known in the literature was used to transfer graphene from copper foil to silicon wafer for the Raman measurements by using a PDMS stamp and ammonium persulfate (APS) as the copper etchant.[3] After attaching PDMS stamp on a graphene on copper foil, the copper layer was etched away in a 1M APS solution in several hours followed by rinsing in a deionized water bath. After drying overnight, the graphene on PDMS piece was stamped on silicon wafer and then PDMS stamp was peeled back by leaving graphene on silicon wafer.

2.2.4. H_2S treatment of graphene on copper foil

In a typical experimental procedure, a piece of graphene on copper was cut for initial SEM imaging (0 min). After SEM imaging, the graphene sample was placed upright in a 4 mL glass vial. The size of the graphene on copper piece and the vial allows almost similar standing angle for the graphene piece in every experiment. Thus, the accessibility of the piece by H_2S gas is similar between different experiments. A 20 mL vial with a larger diameter was charged with 120 mg $Na_2S.9H_2O$. Then the 4 mL vial with graphene sample in it was placed inside the 20 mL vial (Figure 2.1).

Figure 2.1. Photo of the reaction setup before sealing and injection of dilute H_2SO_4 solution. The double vials ensure that the graphene sample is only exposed to H_2S gas which is generated *in situ*, not any liquids or solids. Scale bar: 1 cm.

After that, the 20 mL vial was sealed using a matching screw cap with PTFE/silicone septum. Finally, 0.5 mL of 0.5 M H_2SO_4 solution was quickly injected into the 20 mL vial via a syringe through the septum. Then the reaction setup was immediately placed in dark during the reaction. After certain amount of time (e.g. 15 min), the reaction was stopped by opening the vial and removing the graphene sample. Subsequently, the H_2S-treated graphene sample was

placed under vacuum in dark for about 24 h, in order to remove any potential residual H_2S gas adsorbed on the surface. Later, the chemically treated graphene sample was imaged by SEM for the second time at the same spots as the first SEM imaging. The acquired SEM images were denoted with total amount of reaction time the graphene sample experienced (e.g. 15 min). For reaction time-dependent study, the same H_2S treatment procedure was repeated and the chemically treated graphene sample was imaged by SEM at the same spots as previous cycles of SEM imaging. The acquired SEM images were then denoted with total amount of reaction time the graphene sample experienced (e.g. 30 min, if the second reaction is also 15 min). The same H_2S treatment procedure was used for both hexagonal graphene domains (back side) and polycrystalline graphene films (front side) of the graphene samples. All the H_2S treatment experiments were performed at room temperature in the fume hood.

2.3. Results and Discussion

2.3.1 Characterization of CVD-grown graphene samples

Commercially available CVD-grown monolayer graphene samples from ACS Materials Inc. were used in all experiments. The front side of a typical sample comprises mainly nearly continuous polycrystalline monolayer graphene, whereas the back side has numerous isolated monolayer hexagonal graphene domains (Figure 2.2). Graphene grows continuously across copper crystal grain boundaries (Figure 2.2a). Graphene domains are seen on the back side of the sample (Figure 2.2b). The appearance of individual domains rather than continuous film could be due to inaccessibility of this side of the copper foil by the feedstock inside the quartz-tube during CVD.

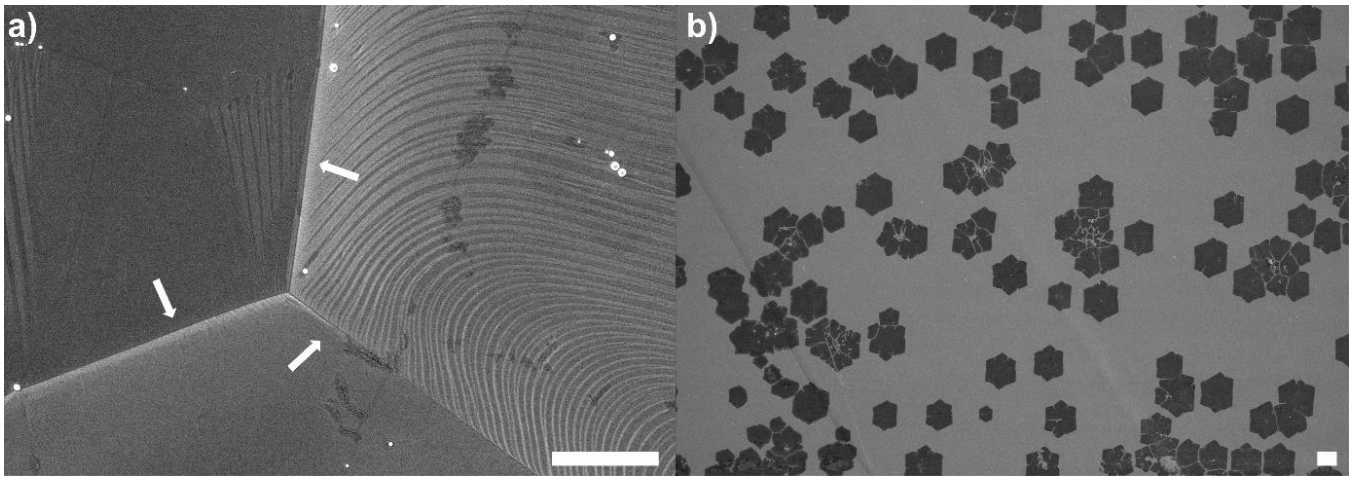

Figure 2.2. Representative SEM images of the purchased CVD-grown graphene on copper. (a) The pristine continuous graphene film from the front side of the sample. The white arrows indicate copper grain boundaries. (b) Pristine multiple hexagonal graphene domains as well as coalesced domains from the back side of the sample. Scale bar: 20 μm.

The Raman spectra of transferred continuous graphene film and individual hexagonal domains on silicon wafer show the characteristic features of the monolayer graphene (Figure 2.3). Representative Raman spectra (Figure 2.3e) from two different spots (Figure 2.3a, b) on pristine monolayer polycrystalline graphene film on Si wafer show the characteristic features of monolayer graphene. Also, representative Raman spectra (Figure 2.3f) from two different spots (Figure 2.3c, d) on the same pristine monolayer hexagonal graphene domain on Si wafer show the characteristic features of monolayer graphene.

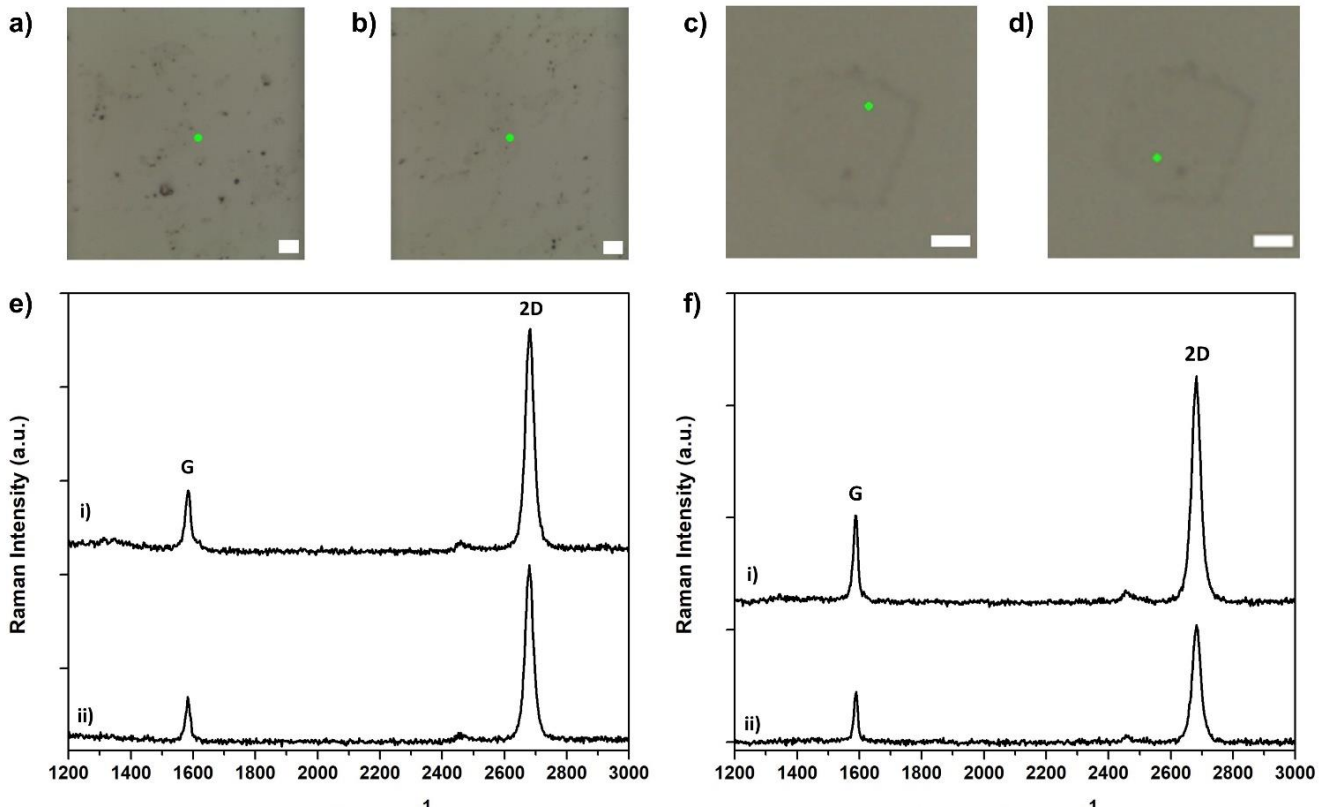

Figure 2.3. Representative Raman spectra of the pristine graphene film and individual hexagonal graphene domain transferred onto Si wafer. **(a-d)** Microscopic optical images of the graphene film and individual hexagonal graphene domain on Si wafer and the green dots showing spots where the Raman spectra were taken. Scale bars: 4 µm **(a-b)** and 2 µm **(c-d)**. **(e-i)** Raman spectrum of **(a)** and **(e-ii)** Raman spectrum of **(b)**, different regions of monolayer graphene film on Si wafer. **(f-i)** Raman spectrum of the spot in **(c)** and **(f-ii)** Raman spectrum of the spot in **(d)** in the same hexagonal graphene domain on Si wafer. Both continuous graphene film from front side and individual hexagonal domain from back side of CVD-grown graphene show the characteristic features of the monolayer graphene.

2.3.2 Chemical probing of vacancy defects in hexagonal graphene domains

The reaction between copper and H_2S in the air is well studied in the literature and is believed to start with the oxidation of copper, then followed by sulfidation to form Cu_2S (Figure 2.4a).[1,2]

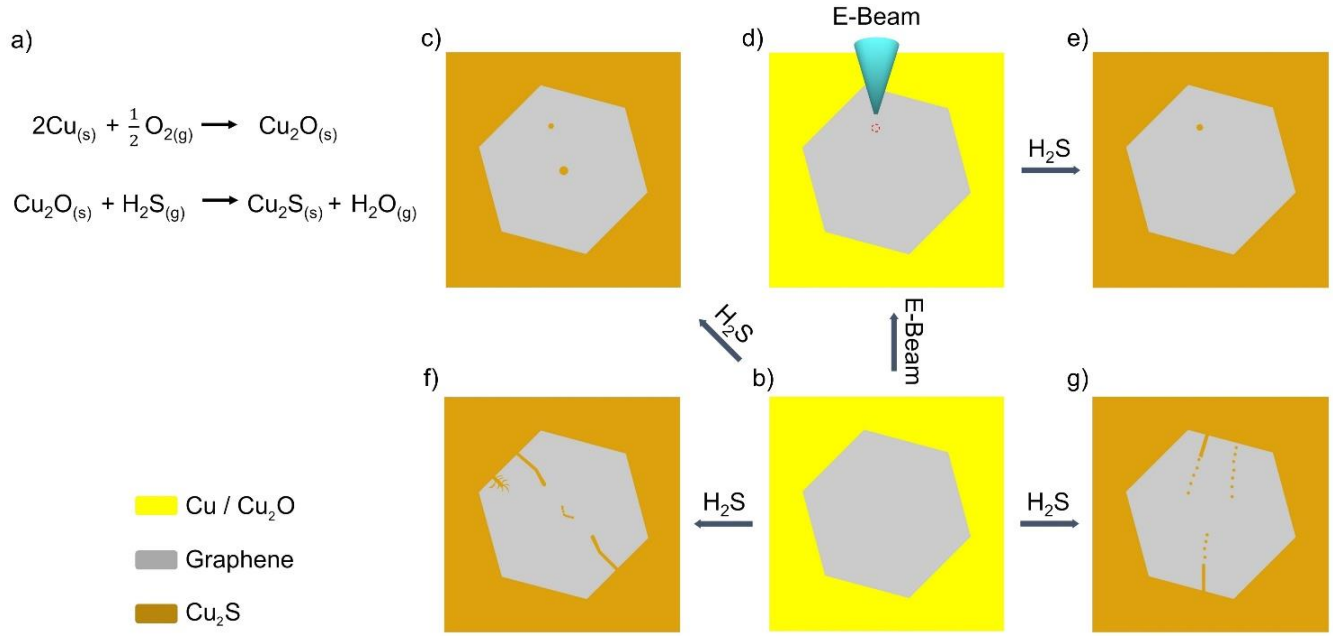

Figure 2.4. Schematic illustration of the *in situ* chemical probing principle. **(a)** The solid-gas phase reactions between H_2S gas and exposed copper substrate in the air lead to formation of Cu_2S nanoparticles at room temperature.[1,2] **(b)** Untreated monolayer hexagonal graphene domain on copper. The H_2S treatment leads to selective formation of Cu_2S nanoparticles in graphene vacancy defect regions. This allows for visualization of various types of graphene vacancy defects under SEM: **(c)** Hole defects; **(d,e)** Hole defect generated by low-energy electron-beam irradiation; **(f)** Various continuous cracks; **(g)** Discontinuous cracks.

The same-spot probing of graphene samples before and after the H_2S treatment allows us to identify the newly formed Cu_2S nanoparticles unambiguously by SEM imaging (Figure 2.4, 2.8, 2.9; 2.13, 2.15-2.17, and 2.22-2.26)

The identity of Cu_2S nanoparticles has been further confirmed by EDX (Figure 2.5) and X-ray diffraction (Figure 2.6). The particles formed with the treatment on the defective sites of

individual graphene domains are examined without transferring. The EDX spectrum shows peaks for Cu, S, O and C elements (Figure 2.5b). The elemental composition of formed particles, in terms of atomic percentages are as follows: C: 9.2 %, Cu: 63.1 %, S: 24.5 %, and O: 3.2 %. The atomic ratio of Cu to S is greater than 2. This can be due to the additional copper signal coming from the Cu substrate.

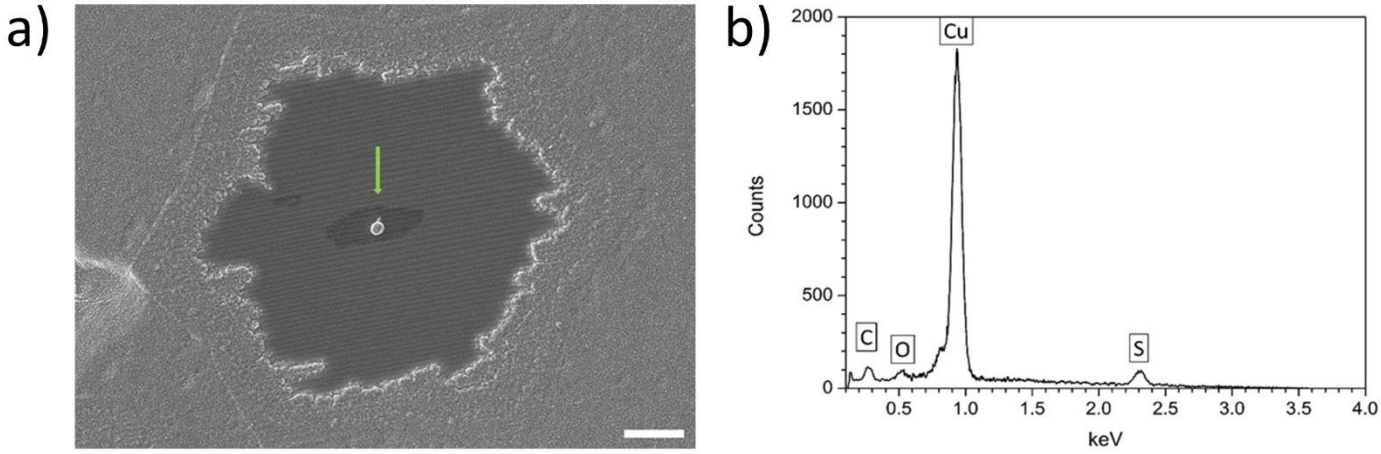

Figure 2.5. EDX spectrum **(b)** of a nanoparticle formed on graphene domain after the H_2S treatment. Electron beam was focused on the center of the nanoparticle (indicated by the green arrow) in the SEM image **(a)**. Scale bar: 3 μm.

A piece of copper foil was treated with H_2S gas by mimicking previously described typical experimental procedure for graphene on copper samples, except for the larger copper foil and longer reaction time is used. A total of 12 hours reaction time was applied to get sufficient amount of particles to be able to perform phase analysis with XRD. The formed thin layer of particles on copper foil surface were scraped off with the help of a razor. The scraped particles were used to obtain XRD spectrum. An XRD spectrum of the particles is presented in Figure 2.6. The diffraction peaks can be indexed as monoclinic Cu_2S (JCPDS no. 33-0490).

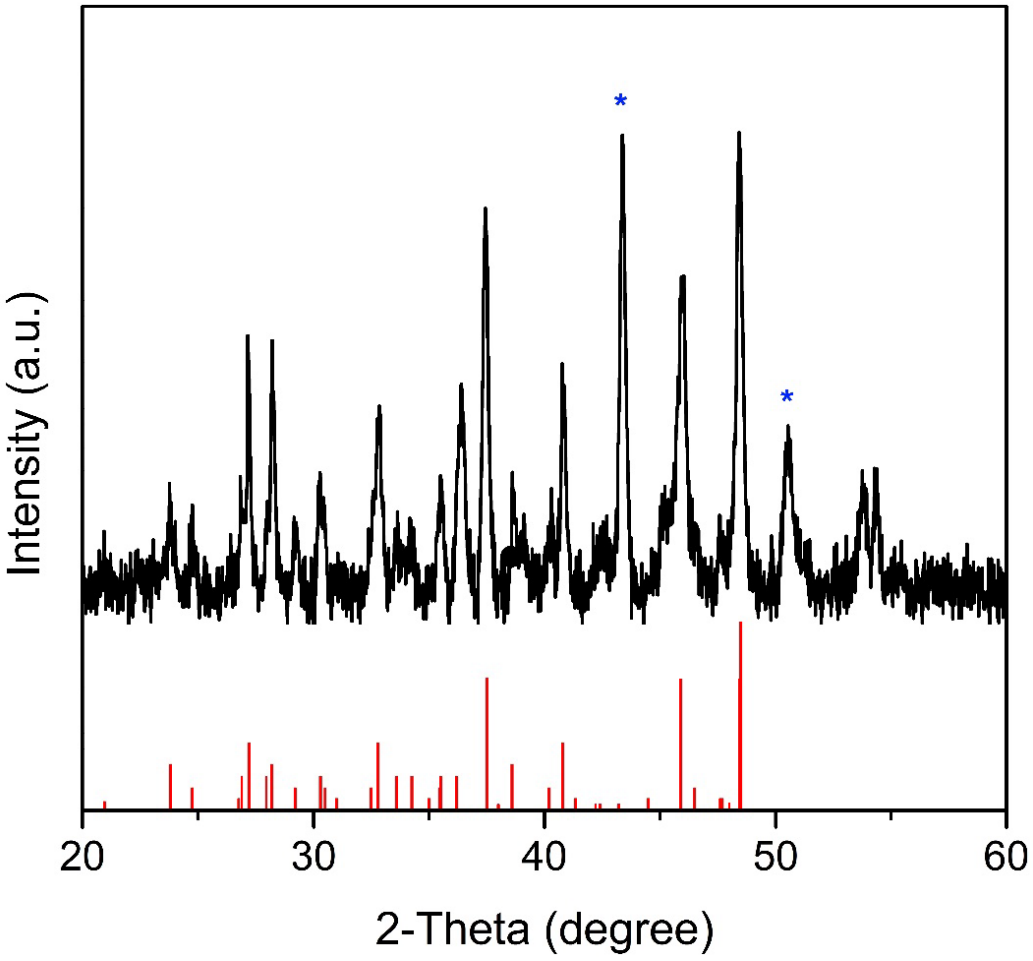

Figure 2.6. XRD pattern of Cu_2S nanoparticles scraped off from the copper foil surface. The asterisks indicate diffraction peaks coming from copper particles.

The reaction time-dependent study shows that the Cu_2S nanoparticle size increases with reaction time until the interaction between oxidized copper and H_2S becomes restricted, probably by the growing Cu_2S nanoparticles (Figure 2.22-2.26).

The nucleation of graphene domains on metal often starts from active carbon species such as magic carbon clusters (e.g. C_{21}) at imperfection sites on metal or locations of impurity nanoparticles.[4,5] We have found that the nucleation centers of many graphene domains surveyed in this study have one or more-hole defects. In some hexagonal domains, no apparent

hole defects or impurity nanoparticles can be detected at the nucleation center by SEM before the H_2S treatment (Figure 2.8c, 2.13c, and 2.13g), but one or more Cu_2S nanoparticles appear at the nucleation center after the H_2S treatment (Figure 2.8d, 2.13d, and 2.13h), indicating the existence of hole defects at the center of the hexagonal domain. The size of a Cu_2S nanoparticle depends on multiple factors such as the reaction time and graphene hole defect size. In addition, the shape of Cu_2S nanoparticle aggregates depends on the shape of a graphene vacancy defect: e.g. a 0D nanoparticle (Figure 2.8, 2.9) *vs* 1D nanowire of coalesced nanoparticles (Figure 2.13). In some other hexagonal domains, the nucleation center is preoccupied with one or more SiO_x nanoparticles (indicated by blue arrows in Figure 2.8e and 2.8g) before the H_2S treatment, which are confirmed by EDX (Figure 2.7).

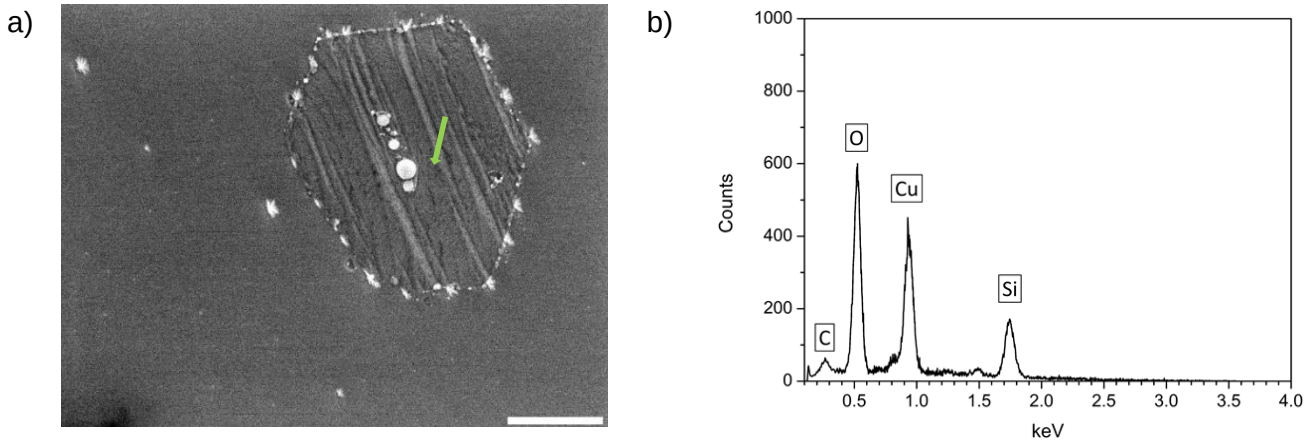

Figure 2.7. Elemental analysis of particle found on the graphene domain on copper foil. **(a)** EDS beam is focused on the center of the particle on a graphene domain that is indicated by the arrow in the SEM image. **(b)** The EDS spectrum of the particle. Scale bar is 2 µm.

SiO_x nanoparticles are well-known contaminants originating from a quartz-tube furnace during the CVD growth of graphene, and they are usually found at graphene defective sites and edges.[6] Interestingly, we have observed the differential responses of the SiO_x sites within the graphene domains towards the same H_2S treatment. For instance, in one domain, merged Cu_2S

nanoparticles grow from three tiny SiO_x nanoparticles of similar sizes at the center of the domain (Figure 2.8e and 2.8f) after the H_2S treatment, indicating the existence of hole defects at all three SiO_x sites. But in another hexagonal domain where three larger SiO_x nanoparticles of similar sizes can be found within the domain, only two Cu_2S nanoparticles with different sizes emerge from two SiO_x sites (one is away from the nucleation center) after the reaction with H_2S, whereas no apparent reaction occurs at the third SiO_x site at the very center of the domain (Figure 2.8g and 2.8h). Such differential responses at different SiOx sites probably arise from tight or loose binding of SiO_x nanoparticles with surrounding defective graphene.

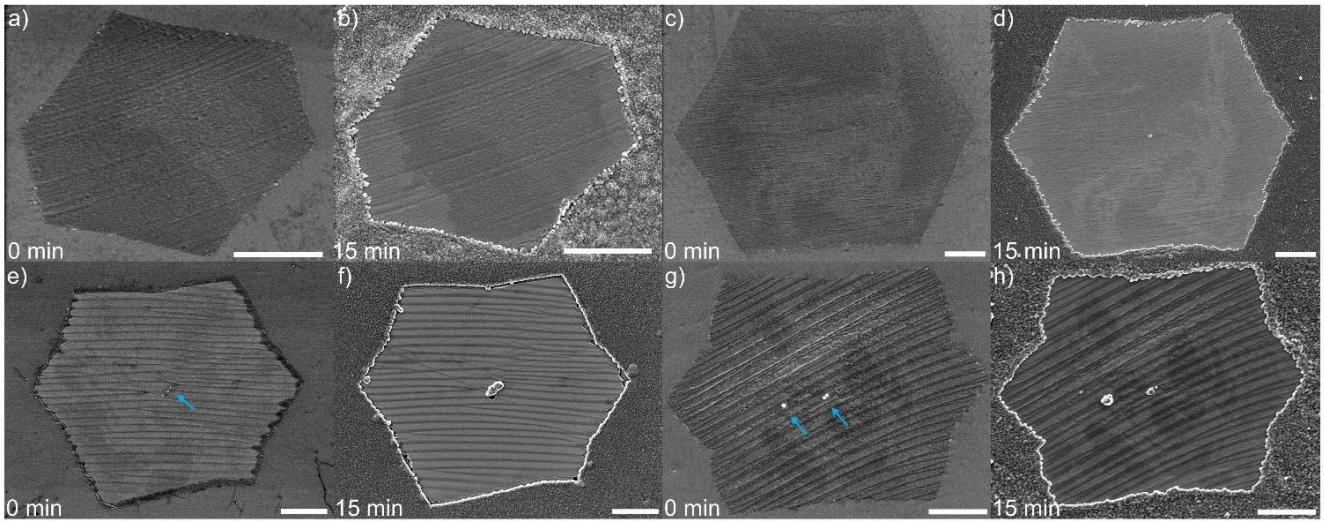

Figure 2.8. SEM images of monolayer hexagonal graphene domains on copper foil before and after H_2S gas treatment. **(a,b)** No Cu_2S nanoparticle is detected after H_2S treatment. **(c,d)** Cu_2S nanoparticle is formed only at the nucleation center of graphene domain. **(e-h)** Cu_2S nanoparticles emerge from SiO_x nanoparticle sites (indicated by blue arrows) after H_2S treatment. Scale bar: 2 µm.

The aforementioned experimental data show clearly that the nucleation centers of many graphene domains surveyed in this study are favorable locations of hole defects. This suggests that the carbon structure at the nucleation center is less stable compared with the rest of the

graphene area, which is consistent with previous theoretical study that identified magic carbon clusters consisting of isolated pentagons as dominating carbon precursors in CVD growth of graphene on various metals.[4]

As mentioned above, we have also observed individual hole defects away from the centers of hexagonal graphene domains (Figure 2.8g, 2.8h, 2.13c, 2.13d, and 2.23). Based on our study, graphene domains without any apparent hole defects and cracks within the domains do exist but are rare. Two such examples are shown in Figure 2.8a, 2.8b, and Figure 2.22a-e, respectively. Since such ideal graphene domains coexist with other defective domains in the same graphene sample, unique unidentified localized graphene growth or healing parameters could be responsible for the formation of such ideal graphene domains.

It is well known that the electron-beam irradiation could damage graphene if the beam energy is close to or exceeds the carbon displacement threshold (86 keV).[7] However, it has been reported that the low-energy electron beam (5-30 keV) can also remove carbon atoms from graphene.[8] In this low-energy carbon etching process, contaminants such as residual water, nitrogen, and oxygen presented on graphene or in the chamber are transformed into active chemical species upon electron-beam irradiation, which then react with graphene to form vacancy defects. Since SEM has been extensively used in this study, we want to investigate whether the electron-beam irradiation can generate new vacancy defects in our typical SEM imaging and EDX conditions.

By comparing SEM images of the same graphene domain after the first and second H_2S treatment, respectively, for numerous graphene domain samples in our reaction time-dependent study (Figure 2.22-2.26), we conclude that the typical SEM imaging conditions used in this study do not produce new vacancy defects that can be detected by our chemical probing

technique. In contrast, we have found strong evidence that EDX with extended irradiation time (≥ 2 min) can induce new hole defects in graphene (Figure 2.9a-c). In addition, we have observed that longer electron-beam irradiation time leads to larger Cu_2S nanoparticle size, which suggests that the beam-induced graphene hole defect size increases with the irradiation time (Figure 2.9a-c). Since the accelerating voltage (3.5 KeV) and beam current (10 μA) remain same for SEM imaging and EDX experiments, the main difference between SEM imaging and EDX lies in very different irradiation time. For SEM imaging in our study, the irradiation time is estimated to be ~ 8 μs/pixel, whereas for EDX, the irradiation time is 1-5 min/spot. The finding that the lengthy electron-beam irradiation (≥ 2 min) at very low energy (3.5 KeV) could etch the graphene has practical implications for graphene characterization and device fabrication that involve the electron-beam irradiation, and controlled patterning of graphene using the electron-beam irradiation.

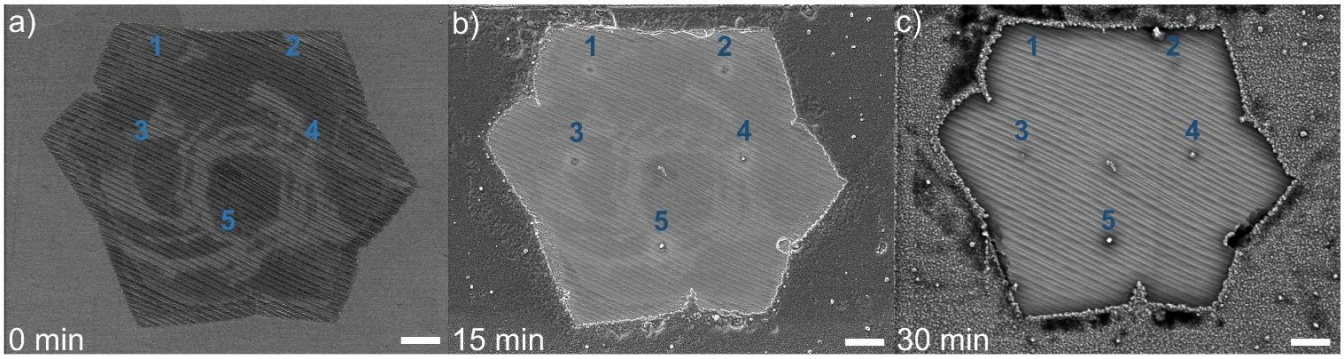

Figure 2.9. SEM images of monolayer hexagonal graphene domain on copper foil before and after H_2S gas treatment following electron beam application. **(a)** Electron beam (3.5 KeV) is applied to the point #1 (1 min), #2 (2 min), #3 (3 min), #4 (4 min), and #5 (5 min), respectively. **(b)** Cu_2S nanoparticles are found on the point #2-#5 after 15 min of H_2S treatment. The size of the nanoparticle increases with the increase of electron-beam irradiation time. **(c)** The same graphene sample is subjected to additional 15 min of H_2S treatment for the total of 30 min of H_2S treatment time. No particle can be detected on the spot #1. Scale bar: 2 μm.

Understanding the fracture behaviors of graphene is crucial for developing practical applications of graphene.[9] Identification of graphene cracks using SEM imaging is still very tricky. Although cracks with large width are sometimes visible under SEM,[10] other cracks, particularly finer cracks, are more difficult to detect using the same imaging technique. Our chemical probing method provides a reliable way to visualize the cracks in graphene under SEM. For instance, it is nearly impossible to distinguish potential cracks from other SEM image contrast features in the untreated graphene domain (Figure 2.13e), but the cracks with various shapes can be easily identified in the same graphene domain after the H_2S treatment, thanks to the formation of 1D nanowires of coalesced Cu_2S nanoparticles in the cracked areas (Figure 2.13f). The reaction time-dependent study shows that Cu_2S nanoparticles form rapidly and occupy all of cracked areas within 15 min of H_2S treatment (Figure 2.24 and 2.25). Further chemical treatment does not change the lengths of 1D Cu_2S nanowires, only increases their widths slightly.

Zhang *et al.* investigated nanoscale fracture of monolayer graphene under coupled in-plane opening and in-plane shear mechanical loading by extensive molecular dynamics simulations.[11] The study considered an initially straight crack subject to in-plane opening (Figure 2.10a) and shear loading (Figure 2.10b) characterized by the local stress intensity factor (SIF) *K* field. As a result of their calculations, graphene is brittle around room temperature and it is easier to break along zigzag direction due to smaller toughness in this direction.

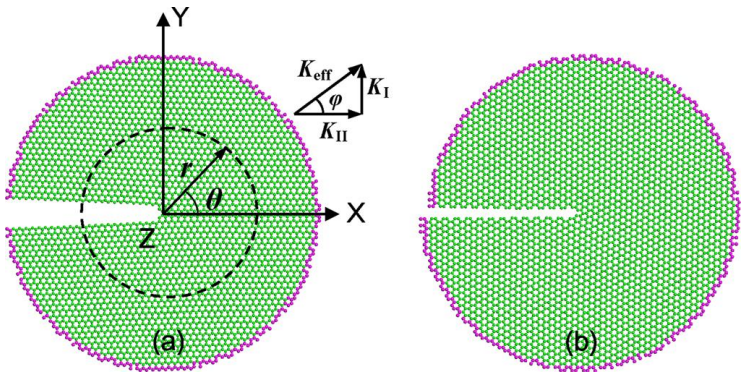

Figure 2.10. Boundary layer MD models and coordinates. A pre-existing straight crack along **(a)** zigzag and **(b)** armchair edge is embedded in a two-dimensional graphene lattice (green). K_{eff} is effective stress intensity factor. K_I and K_{II} are SIF components specified by opening and shear stress, respectively. φ is the phase angle.[11]

The graphene fracture process is dynamic with firstly the cleavage of the most stretched C-C bond abruptly and subsequently disruption of adjacent bonds. φ angle between opening and shear stress changes by which the stress that is more effective. Thus, the path of the crack shifts depending on the dominant stress. As can be seen from the Figure 2.11, in the case of ZZ crack, the crack follows the similar direction with 120° angle of crack propagation when φ= 0°, 30°, 45°, 60° and changes when φ is over 65°. In the case of AC crack, the crack follows the similar direction with 150° angle of crack propagation when φ= 30°, 45°, 60°, 90° and changes when φ is under 26.5°.[11]

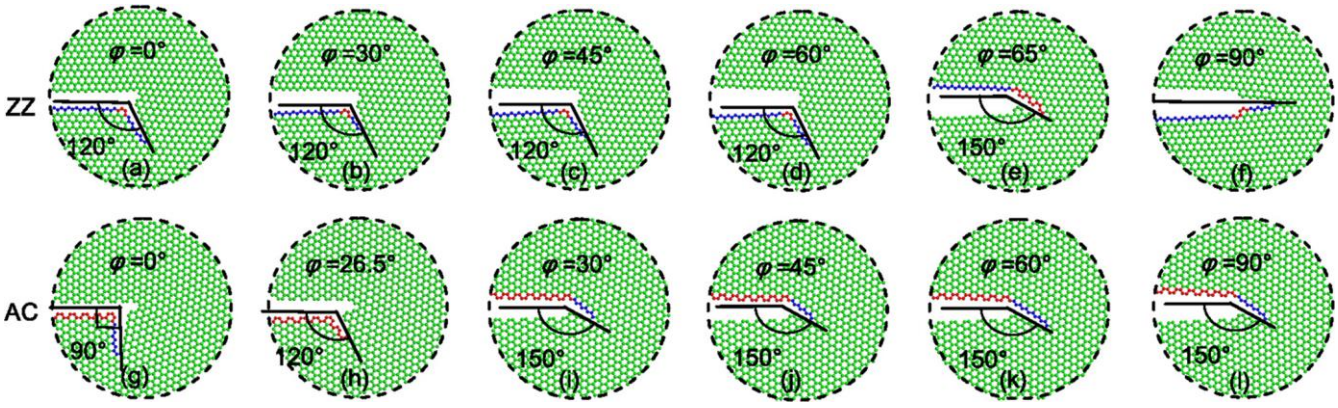

Figure 2.11. The crack propagation after initiation in Figure 2.10 under complex mechanical stress. **(a–f)** Zigzag (ZZ) crack models at φ= 0°, 30c, 45°, 60°, 65°, and 90°. **(g–l)** Armchair (AC) crack models at φ= 0°, 26.5°, 30°, 45°, 60°, and 90°, respectively. The angle of crack propagation orienting to primary crack is depicted correspondingly. ZZ crack edges are shown in blue, AC in red.[11]

In other words, when the in-plane opening stress component becomes significant under complex mechanical stresses, the armchair-to-zigzag kinked crack with 150° angle is always most favorable.[11] However, it is more complicated for the propagation of the initial zigzag crack under complex mechanical stresses. The zigzag-to-zigzag kinked crack with 120° angle is more favorable when the in-plane shear stress component is significant. But the zigzag-to-armchair kinked crack with 150° angle becomes more favorable when the in-plane opening stress component becomes considerably more significant than the in-plane shear stress component. Ultimately the straight zigzag crack without kinking becomes dominant when there is only pure in-plane opening stress.

Figure 2.11 shows that the various sites of bond breaking that's not the original crack tip. Asymmetric cleavage (other than 2.11f for a ZZ) demonstrates that brittle fracture through bond breaking prevails at room temperature. This causes the fracture path to shift downward relative to the initial crack. After the initial crack with both of ZZ and AC edges, it is more apparent that the new crack propagates with ZZ edge (Figure 2.11a,b,c,d,f,g,I,j,k,l) rather than AC edge (Figure 2.11e,h).

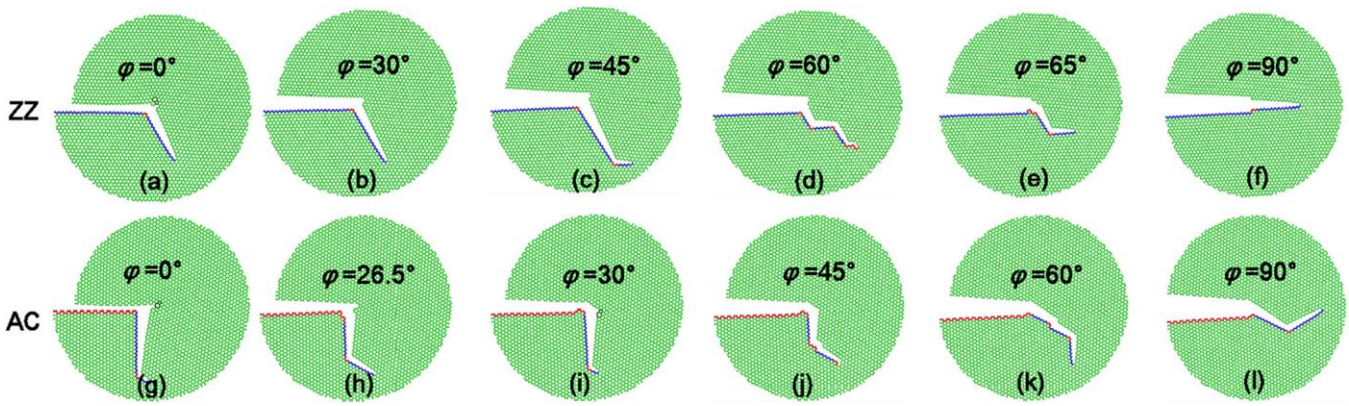

Figure 2.12. Images of crack kinking in graphene lattices (green) after propagation in Figure 2.11. ZZ (blue), or AC (red) edges appear alternatively changing direction of growth.[11]

The direction of crack growth changes definitely under coupled opening and shearing stresses, and edges convert between ZZ and AC, preferably along zigzag directions (Figure 2.12). Their simulations demonstrate that torn edges maintain straightness and cleanness along either zigzag or armchair direction and can change directions by 30° or multiples of 30°. Furthermore, more abundant ZZ edges are present due to not only lower edge energy of ZZ edges but also dynamic fracture effects during propagation of the crack.

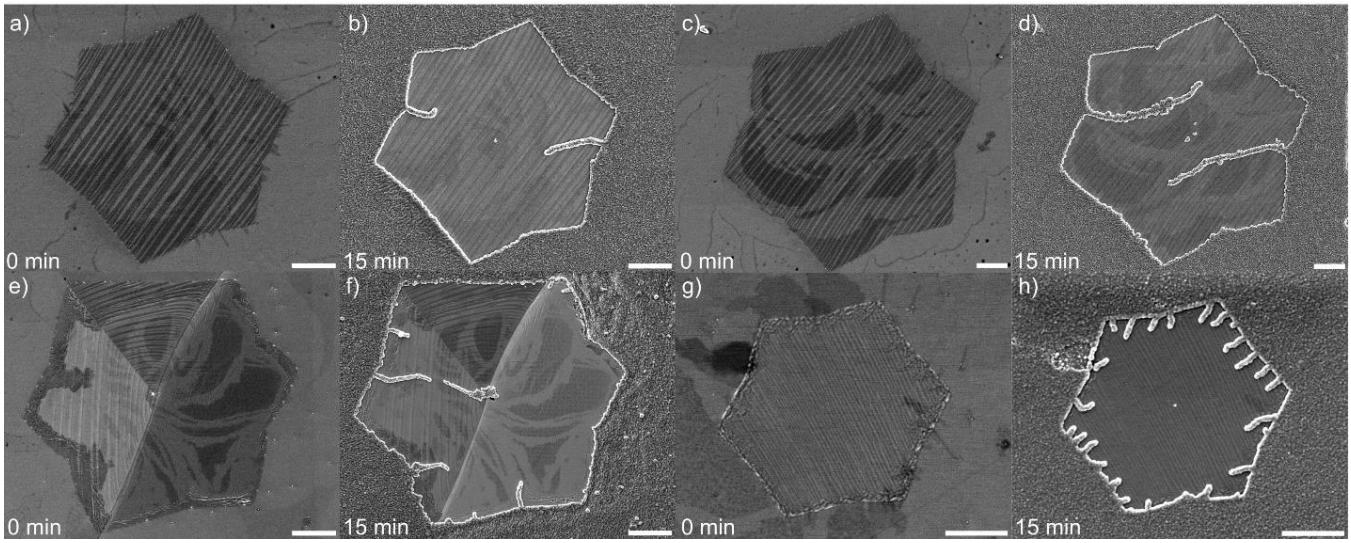

Figure 2.13. SEM images of graphene domains before and after H_2S treatment. Both kinked and straight cracks can be visualized with formation of Cu_2S nanoparticles in the crack regions. Scale bar: 2 μm.

Since the monolayer graphene is supported by copper foil in our study, in-plane mechanical stresses are expected to predominate and therefore Zhang *et al*'s work is applicable to our results. It has been well established that the hexagonal graphene domain is terminated with zigzag edges.[12-14,16] By comparing the angles of 1D nanowires with hexagonal graphene edges, we have found that most cracks orient along either the armchair or zigzag directions, which are consistent with previous studies.[4,7,10,15,] If the edge has a re-entrant angle, we use the plotted straight line between two adjacent vertices of the hexagon as the zigzag reference line. In addition to observation of some straight cracks, we have also discovered that some initial cracks kink at the angle of primarily 150° or 120°. Some representative examples of straight cracks and kinked cracks are presented in Figure 2.13, and Figure 2.24 and 2.25. More specifically, an initial armchair crack turns at the angle of predominantly 150° to form a zigzag crack (Figure 2.14a, c), whereas an initial zigzag crack turns at the angle of either 120° to form a new zigzag crack or 150° to form an armchair crack (Figure 2.14b, d).

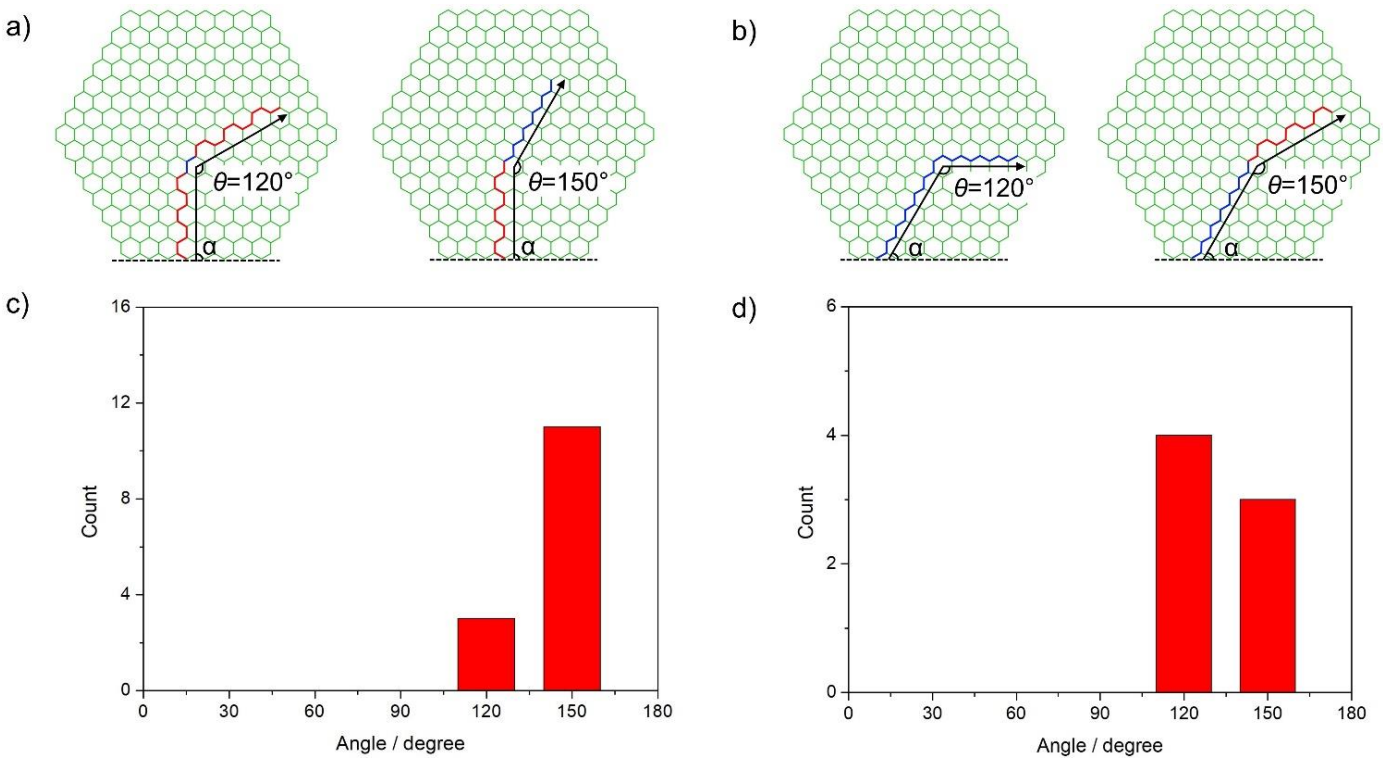

Figure 2.14. (a,b) Schematic illustration of representative kinked graphene crack structures. **(c)** Histogram of the distribution of kink angles (θ) for the cracks starting at 90° (± 10°) angle (α) from zigzag edge. **(d)** Histogram of the distribution of kink angles (θ) for the cracks starting at 60° (± 10°) or 120° (± 10°) angle (α) from zigzag edge.

These experimental results on selective crack kinking are in reasonably good agreement with aforementioned theoretical study by Zhang and coauthors.[11] The propagation of cracks with zigzag edge through kinking is more common in the graphene samples in our study. Furthermore, our method allows experimentally investigate graphene cracking behavior which is studied theoretically or in simulations in the literature.[11]

The study of graphene cracking is important in terms of practical applications. For example, demonstrated roll-to-roll processing of CVD-graphene may lead to cracking of graphene due to applied tensile stress.[17] In addition, graphene, as the strongest material, is used as a reinforcement to increase the resistance to fracture in composites. Therefore, existing

graphene cracks may diminish expected outcomes in such applications.[11] Our H_2S treatment method presents a practical way to observe cracking of graphene. The cracking of graphene also holds importance in terms of newly formed edge structure (ZZ or AC) as edge structure affects electronic and magnetic properties of graphene nanostructures.[7,15] Our method provides a simple way to characterize graphene edges without laborious techniques such as STM, TEM or Raman spectroscopy.[18]

Although most cracks we investigated start at the graphene edges, we have occasionally observed cracks that appear to initiate from the nucleation center of the graphene domain (Figure 2.13f, 2.15b, 2.15d, 2.16b, and 2.16d). Interestingly, sometimes two cracks originate from the center of the hexagonal domain, resembling the hour and minute hands in a clock (Figure 2.16b and 2.136d). Such cracks with clock-hands patterns indicate the existence of stresses with different directions in the same graphene domain during the crack formation.

We have also observed branched cracks in some hexagonal graphene domains. In particular, one hexagonal domain shown in Figure 2.15d shows a group of cracks with main crack lines orienting roughly along the zigzag direction. Among these cracks, only one crack is straight without branches (but it is discontinuous at some points), and the rest of cracks display varying degrees of branched structures. Some graphene cracks exhibit snowflake-like branched structures, which are highlighted with purple arrows in Figure 2.15d. Although the exact formation mechanism remains unknown, the crack branching may be caused by the strain that is perpendicular to some C-C bonds based on previous theoretical study.[19] It was also found in a finite element modelling study that the graphene crack propagates straight along the zigzag direction under low strain rates, whereas the crack kinks and branches under high strain rates.[20] This particular hexagonal domain shown in Figure 2.15d also highlights potentially

complex strains experienced by an individual graphene domain during the crack formation. While unidirectional global strain across the graphene domain may lead to the parallel orientation of main crack lines, the localized additional strain factors are probably responsible for different fine crack structures observed in the same domain (Figure 2.15d).

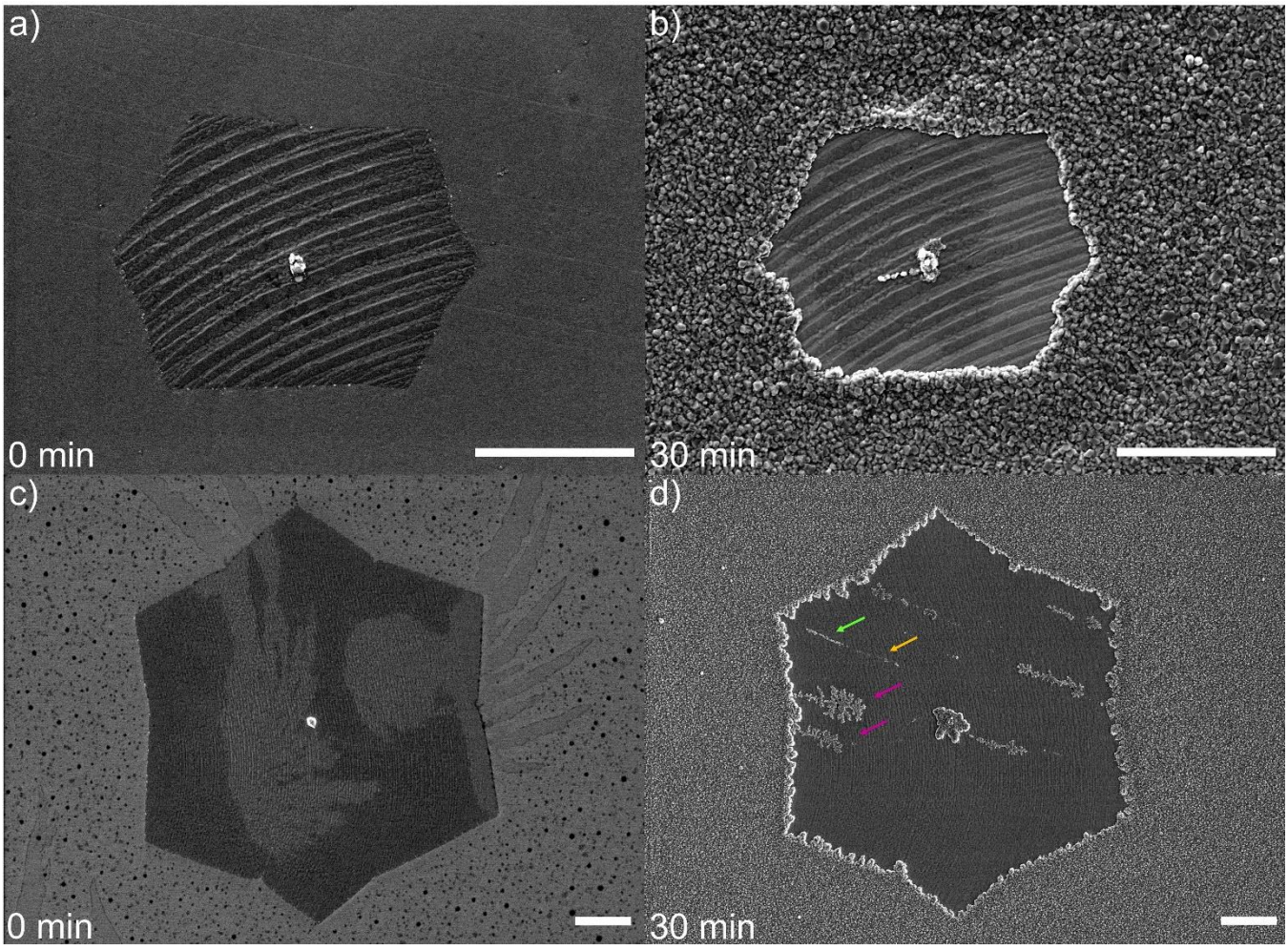

Figure 2.15. SEM images of graphene domains before and after H_2S treatment. **(a,b)** Crack initiates from domain center. **(c,d)** A group of cracks with main crack lines orienting roughly along the zigzag direction. One straight continuous crack (indicated by green arrow) is immediately followed by discontinuous crack (indicated by orange arrow) along the same direction. Other cracks display varying degrees of branched structures. Some graphene cracks exhibit snowflake-like branched structures (indicated by purple arrows). Scale bar: 3 µm.

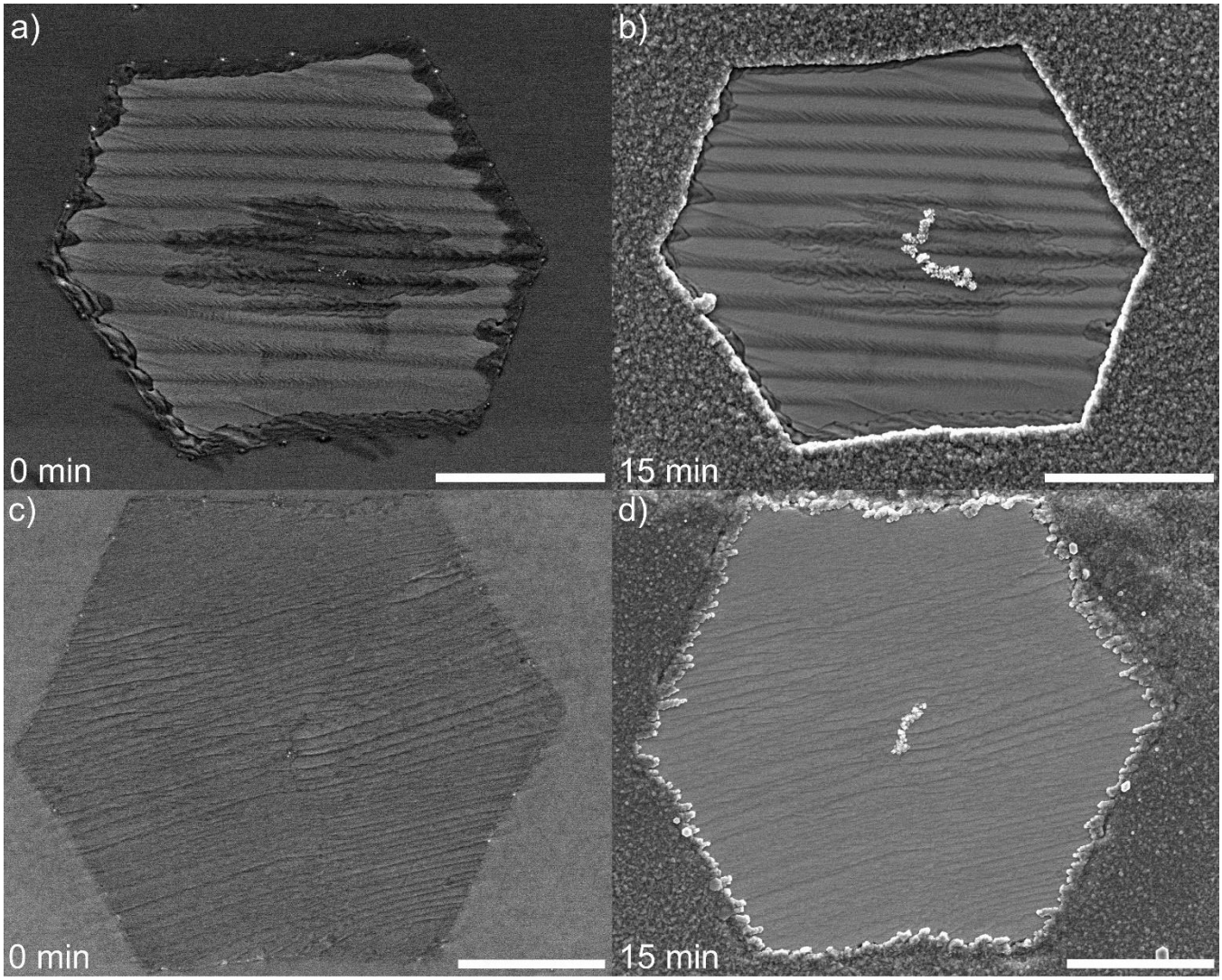

Figure 2.16. SEM images of graphene domains before **(a,c)** and after **(b,d)** H_2S treatment. Two cracks originate from domain center, resembling hour and minute hands in a clock. Scale bar: 2 µm.

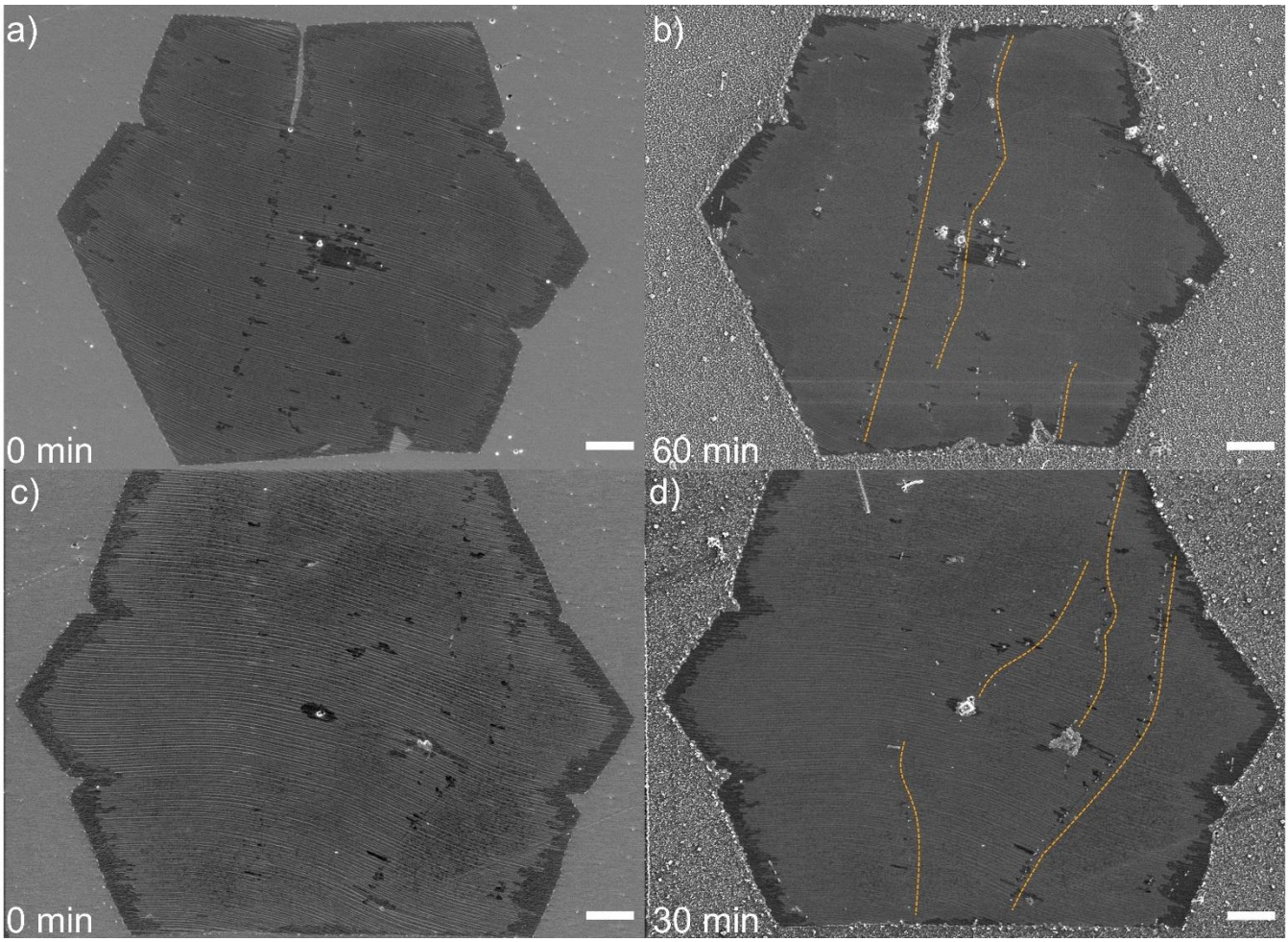

Figure 2.17. SEM images of graphene domains before **(a,c)** and after **(b,d)** H_2S treatment. **(b-d)** Discontinuous cracks highlighted by orange dashed lines. Scale bar: 3 µm.

Most interestingly, we have discovered that discrete Cu_2S nanoparticles in some treated graphene domains are aligned along a straight or curved line (Figure 2.15d, 2.17b, and 2.17d), instead of forming continuous 1D nanowires of coalesced Cu_2S nanoparticles. This strongly suggests the existence of discontinuous cracks in some graphene domains, where the hole defects are oriented along a straight or curved line. The freestanding graphene is well known to undergo a brittle fracture with continuous cleavages at room temperature.[9] In contrast, the observed discontinuous cracks more likely originate from a ductile fracture of graphene, which

involves a plastic deformation ahead of the fracture. In the ductile fracture of conventional materials, the plastic deformation leads to formation of microvoids first, then followed by coalescence of microvoids to form a continuous crack.[20] The discontinuous cracks (Figure 2.15d, 2.17b, and 2.17d) resemble the “necklace” coalescence mode in the ductile failure,[21] which suggests that they may be intermediate precursors to continuous cracks. Furthermore, we have noticed some examples where the continuous crack is immediately followed by oriented hole defects along the roughly same cracking direction (Figure 2.15d, 2.17b).

According to theoretical studies, the fracture mechanism of graphene is dominated by the co-existing ductile flip and brittle breaking of the carbon bonds.[22-24] At low temperature, the plastic deformation is prohibited and the brittle fracture via bond breaking prevails. At high temperature, however, the plastic deformation such as Stone-Wales bond rotation plays a significant role and the ductile fracture predominates. This raises the possibility that the observed discontinuous cracks are probably formed at high temperature during the CVD process than at room temperature. In addition, the aforementioned theoretical studies focus on freestanding graphene, so it is not clear at present what potential effects of a metal support such as copper foil may have on the fracture of graphene.

2.3.3. Chemical probing of vacancy defects in polycrystalline graphene films

Since the front side of a typical CVD-grown monolayer graphene sample from ACS Materials Inc. comprises mainly nearly continuous polycrystalline monolayer, we have also conducted preliminary chemical probing study of vacancy defects in polycrystalline graphene films. Owing to electron channeling effects, different copper grains appear with different

brightness under SEM.[25] Therefore copper grain boundaries in graphene samples are generally visible under SEM (Figure 2.19a-f). [5,26-28] In addition, sometimes copper stripes underneath graphene are shown in SEM (Figure 2.19a-d, g, and h), which originate from the graphene-induced copper surface reconstruction during cooling after the CVD growth.[1,28] Based on our EDX study, the most common pre-existing impurity nanoparticles are SiO_x nanoparticles (Figure 2.18), which are well-known contaminants originating from a quartz-tube furnace during the CVD growth of graphene.[6]

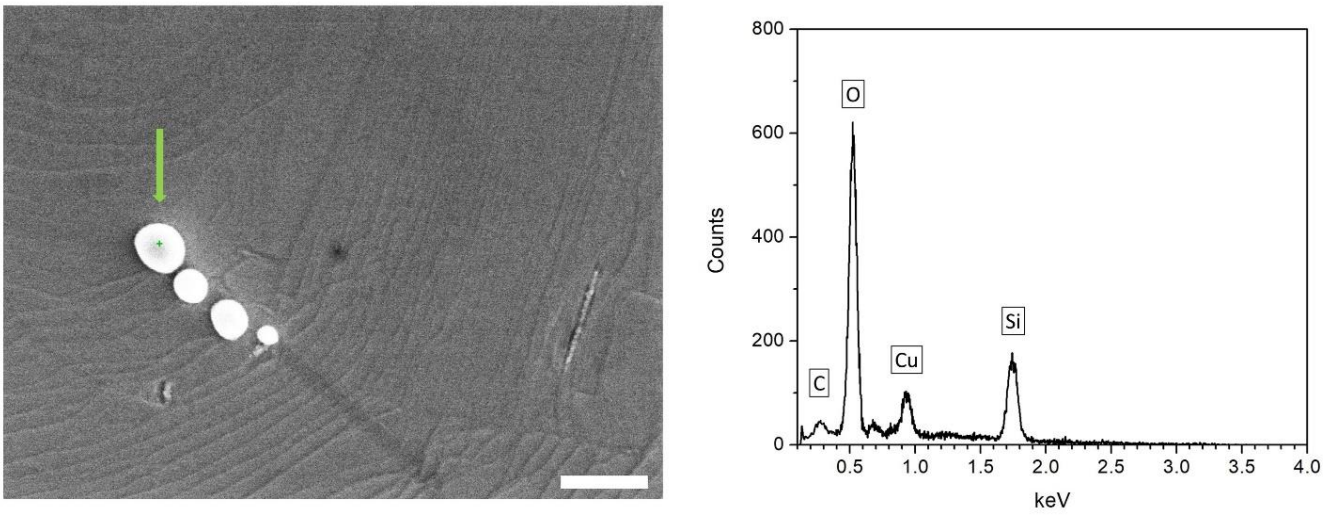

Figure 2.18. EDX spectrum (right) of a pre-existing nanoparticle in polycrystalline graphene film before the H_2S treatment. Electron beam was focused on the center of the nanoparticle (indicated by the green arrow) in the SEM image (left). Scale bar: 0.5 µm.

The same-spot *in situ* SEM probing before and after the H_2S treatment has been used for selective and reliable identification of newly formed Cu_2S nanoparticles in graphene vacancy defect regions. We have not observed other non-vacancy graphene defects such as grain boundaries, which block the reaction of H_2S with underlying copper substrate.[29-30]

As shown in Figure 2.19a and 2.19b, Cu_2S nanoparticles of various sizes emerge from both SiO_x nanoparticle sites (indicated by blue arrows in Figure 2.19a) and non-SiO_x regions in a monolayer polycrystalline graphene film on copper, indicating the existence of hole defects in these regions. Continuous cracks can also be clearly identified due to the formation of 1D nanowires of coalesced Cu_2S nanoparticles in the cracked areas (Figure 2.19b, d, and f).

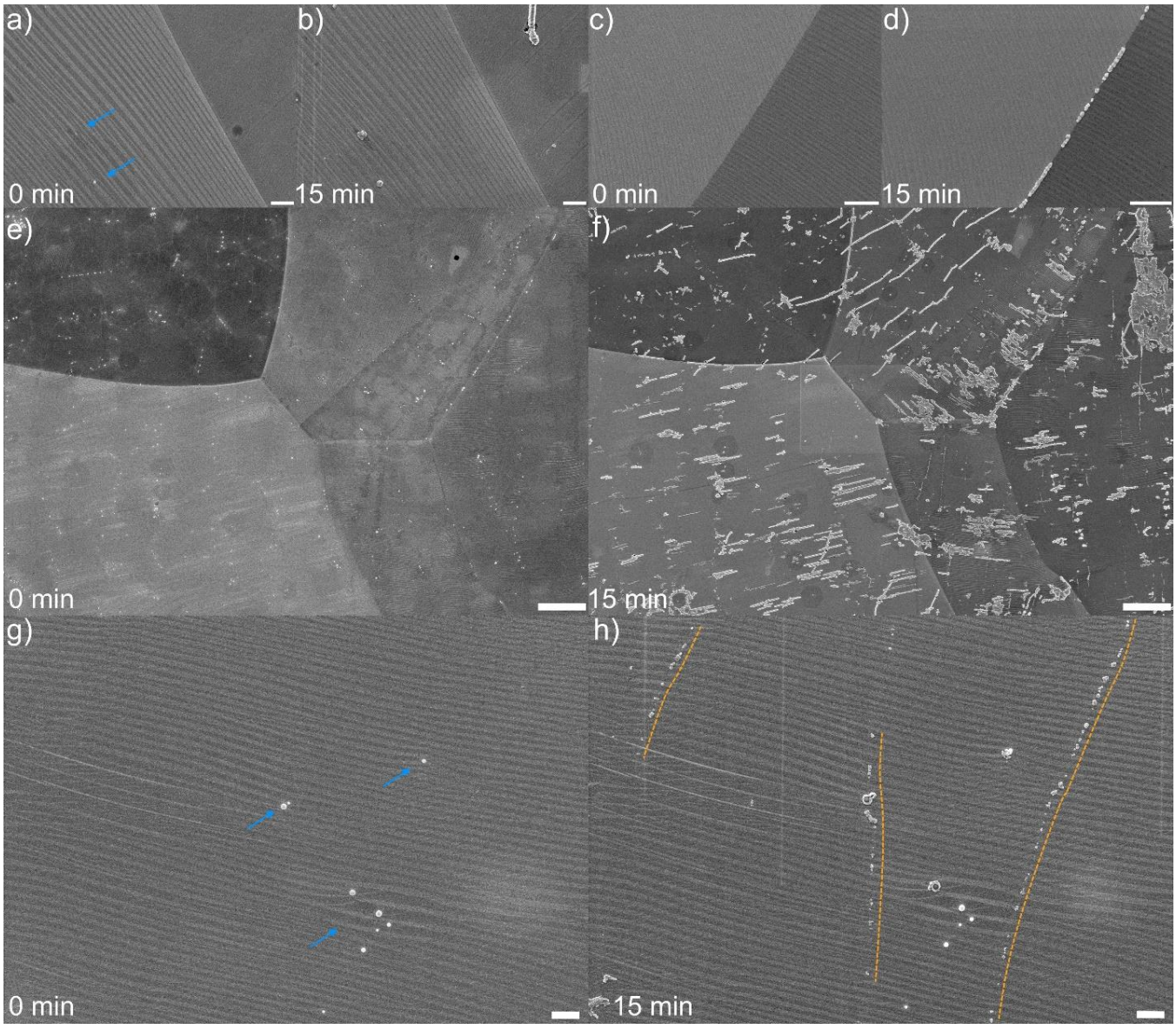

Figure 2.19. SEM images of polycrystalline graphene films on copper foil before and after H_2S gas treatment. **(a,b)** Cu_2S nanoparticles emerge from both SiO_x nanoparticle sites (indicated

by blue arrows) and non-SiO_x regions after H_2S treatment. **(c,d)** Cu_2S nanoparticles are formed on the copper grain boundary. **(e,f)** Numerous cracks and hole defects are visualized in a defective graphene film region on multiple copper grains after H_2S gas treatment. Majority of graphene cracks are oriented roughly along the same direction within the same copper grain, but different copper grains lead to different orientation of graphene cracks. Cu_2S nanoparticles are also formed on some copper grain boundaries. **(g,h)** Discontinuous cracks highlighted by orange dashed lines. Pre-existing SiO_x nanoparticle sites are indicated by blue arrows. Scale bar for **(a-d)** and **(g,h)**: 1 μm. Scale bar for **(e,f)**: 10 μm.

Our study also suggests that the copper grain and copper grain boundary play significant roles in formation and distribution of graphene vacancy defects. For instance, we have discovered that the copper grain boundaries are sometimes favorable locations of hole defects and cracks (Figure 2.19d and f). Most interestingly, for graphene cracks within the copper grains, majority of cracks are oriented roughly along the same direction within the same copper grain, but different copper grains lead to different orientation of graphene cracks (Figure 2.19f). This observation indicates that the orientation of graphene vacancy defects is controlled by underlying copper grain structure. It has been previously reported that the shape, orientation, edge geometry, and thickness of CVD-grown graphene domains can be controlled by the crystallographic orientations of copper substrates.[31] Although the exact underlying mechanisms remain unclear at present and require an in-depth systematic investigation in the future, our results suggest that the copper grain structure and copper grain boundary are important sources of potential mechanical strains that could lead to the formation of vacancy defects in polycrystalline graphene films on copper during the CVD growth and/or subsequent cooling.

As in some hexagonal graphene domains (Figure 2.15d, 2.17b, and 2.17d), we have also observed discontinuous cracks in the polycrystalline graphene film, where the hole defects are oriented along a straight or curved line (Figure 2.19h). The size of the very small Cu_2S

nanoparticles in Figure 2.19h was measured by using ImageJ software. The diameters of some very small Cu_2S nanoparticles in Figure 2.16h are in the range of 30-50 nm. Figure 2.20 provides a closer look and the measured sizes of particles of the same region before and after H_2S treatment.

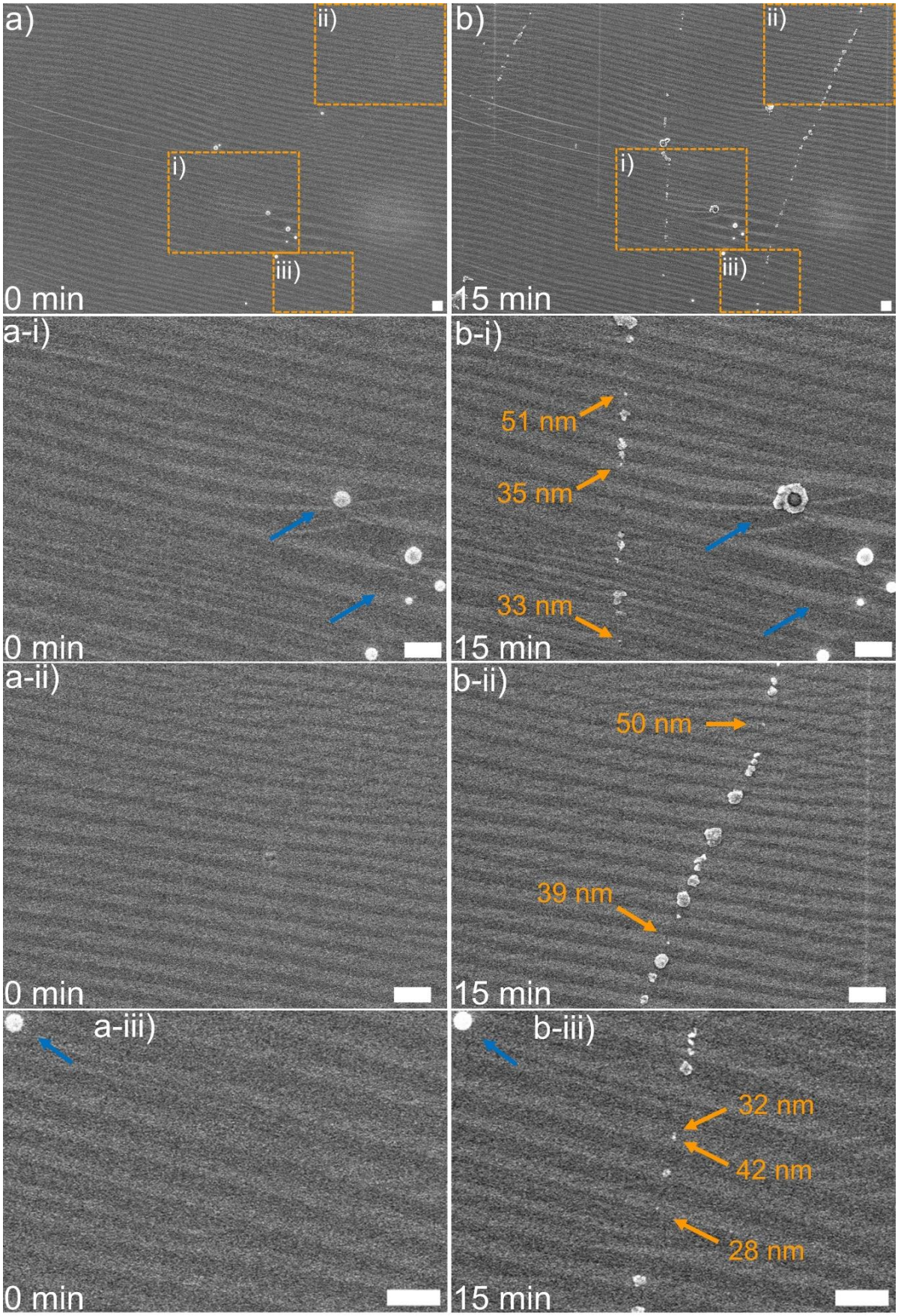
a)
ii)
i)
iii)
0 min
b)
ii)
i)
iii)
15 min
a-i)
0 min
b-i)
51 nm
35 nm
33 nm
15 min
a-ii)
0 min
b-ii)
50 nm
39 nm
15 min
a-iii)
0 min
b-iii)
32 nm
42 nm
28 nm
15 min

Figure 2.20. SEM images of polycrystalline graphene films on copper foil before and after H_2S gas treatment. **(a,b)** SEM images from Figure 2.14g and h with three highlighted zoom-in regions. **(a-i,b-i)** SEM images from the zoom-in region (i). **(a-ii,b-ii)** SEM images from the zoom-in region (ii). **(a-iii,b-iii)** SEM images from the zoom-in region (iii). Pre-existing SiO_x nanoparticle sites are indicated by blue arrows. The Cu_2S nanoparticle size analysis was performed in original SEM images using the ImageJ software. Scale bar: 500 nm.

Since the underlying graphene vacancy defects should be no larger than the diameters of Cu_2S nanoparticles, our experimental data suggest that H_2S can penetrate through nanoscale vacancy defects and react with the Cu substrate. Copper grain boundaries are not directly responsible for the formation of such discontinuous cracks, because they are absent in related regions of both graphene domains and the film (Figure 2.15d, 2.17b, and 2.17d and 2.19h). As discussed in the section 2.3.2, the observed discontinuous cracks most likely originate from a ductile fracture of graphene, which involves a plastic deformation probably at high temperature during the CVD process, leading to the formation of orientated nanoscale hole defects before the fracture. This is similar to the ductile fracture of conventional materials, where the plastic deformation leads to formation of microvoids first, then followed by coalescence of microvoids to form a continuous crack.[21] It remains to be investigated what potential effects of a metal support such as copper foil may have on the fracture of graphene.

The ductile fracture mainly consists of void nucleation, growth and coalescence of voids (Figure 2.21). After a substantial void growth, void linking or coalescence occurs.[21] In contrast, brittle fracture occurs almost instantaneously when a critical threshold is reached. Brittle fractures are characterized as having little or no plastic deformation prior to failure. Brittle materials fail by propagation of cracks.[32] The discontinuous cracks (Figure 2.15d, 2.17b, and 2.17d) resemble the “necklace” coalescence mode in the ductile failure (figure 2.21e),[21] which suggests that they may be intermediate precursors to continuous cracks. Furthermore, we have

noticed some examples where the continuous crack is immediately followed by oriented hole defects along the roughly same cracking direction (Figure 2.15d, 2.17b).

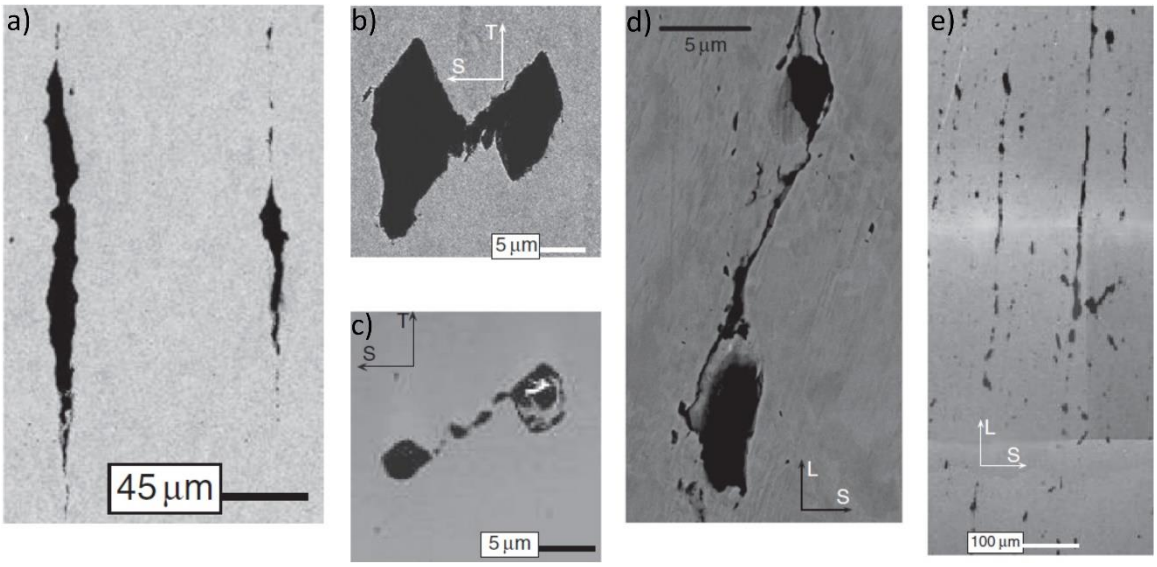

Figure 2.21. (a) Void growth. **(b-e)** Modes of void coalescence: **(b)** Necking of intervoid ligament **(c-d)** Coalescence in a microshear band. **(e)** "Necklace" coalescence.[21]

In molecular dynamics (MD) simulations on nanoscale fracture of graphene under complex mechanical stress, it is shown that the fracture shows plastic behaviors at high temperatures over 1000 °K and brittle at room temperature.[11,22] Stone-Wales isomerization, the bond rotation through concerted movement of two atoms, is a key step towards mechanical relaxation. It is thermodynamically most favorable relaxation but happens under high tension and high temperature due to needed thermal activation energy.[23] Stone-Wales defects and vacancy defects act as a nucleation centers for graphene fracture and deteriorate the sheet strength.[32] Graphene synthesized by CVD method exposed to high temperature and mechanical strain in the CVD chamber before and during the cooling stage. Therefore, it is possible that synthesized graphene on metal substrate can experience ductile-type bond flip and the brittle bond-breaking while its temperature falling down to room temperature. While

ductile fracture is dominant in high temperature and strain conditions, bond rotations would be common.[23] In high temperatures, graphene fracture shows plastic behavior such as reconstruction of crack edges, formation and motion of defects and vacancies.[20] On the other hand, when brittle fracture is dominant at room temperature, bond breaking would prevail.[32] Mechanical stresses applied during the processing of synthesized graphene film at room temperature would possibly cause additional brittle fracture.

It is important to identify graphene defects as caused by ductile or brittle fracture in order to understand the formation of these defects and mechanical behavior of graphene. The experimental works are very limited in the literature for the fracture behavior of monolayer graphene due to the hardship of designing practical experiments at the nanoscale.[33] For example, electron microscopy techniques that is used for imaging fracture may enhance plastic behavior due to heat caused by irradiation.[23] Hence, existing studies on graphene mechanics are either theoretical or based on simulations. Moreover, these theoretical and simulation studies consider freestanding graphene which does not include the interaction with the substrate. Therefore, our method provides a way to experimentally study mechanical behavior of graphene.

There are efforts among graphene researches to synthesize large area single crystalline graphene by CVD, without grain boundaries.[34] This makes methods for the identification of vacancy defects more important in terms of characterization of graphene as single crystalline graphene is believed to be closer to ideal graphene with possibly less or no defects.

Beside the defects formed during the CVD, other defects which can be created during various processes can also be studied by our method. It is common that graphene synthesized on copper foil by CVD is stored on the same substrate and exposed to environmental or

experimental conditions such as air, moisture, high temperature and UV-light, electron-beam, laser light and etc. SEM and TEM are commonly used imaging techniques for graphene. Graphene is exposed to electron-beam irradiation during SEM, TEM and EDX as well as electron-beam lithography studies. A laser beam is used in Raman spectroscopy or microscopy experiments which may possibly cause damage on graphene in a lengthy exposure. In addition, as it clearly seen from our experimental results in Figure 2.9, the conditions which electron-beam can create graphene defects can differ for suspended graphene and graphene on a substrate. Therefore, our method provides a more realistic investigation for the causes of defects in graphene while including graphene and copper interactions too.

2.3.4. H_2S-related issues

As several theoretical works have studied potential interactions between H_2S and graphene,[35,36] it is necessary to address whether the H_2S exposure can damage the graphene or not. In our study, H_2S-treated graphene is always placed under vacuum in dark for about 24 h, in order to remove any potential residual H_2S gas adsorbed on the surface. Therefore, there should be no or minimum residual H_2S gas on treated graphene sample. In our reaction time-dependent study, the same H_2S treatment procedure was repeated and the chemically treated graphene sample was imaged by SEM at the same spots as previous cycles of SEM imaging. As shown in SEM images of our reaction time-dependent study (Figure 2.22-2.26), no new vacancy defects can be detected at the same spot after the previous H_2S treatment, which indicates that the H_2S treatment does not create new vacancy defects in graphene.

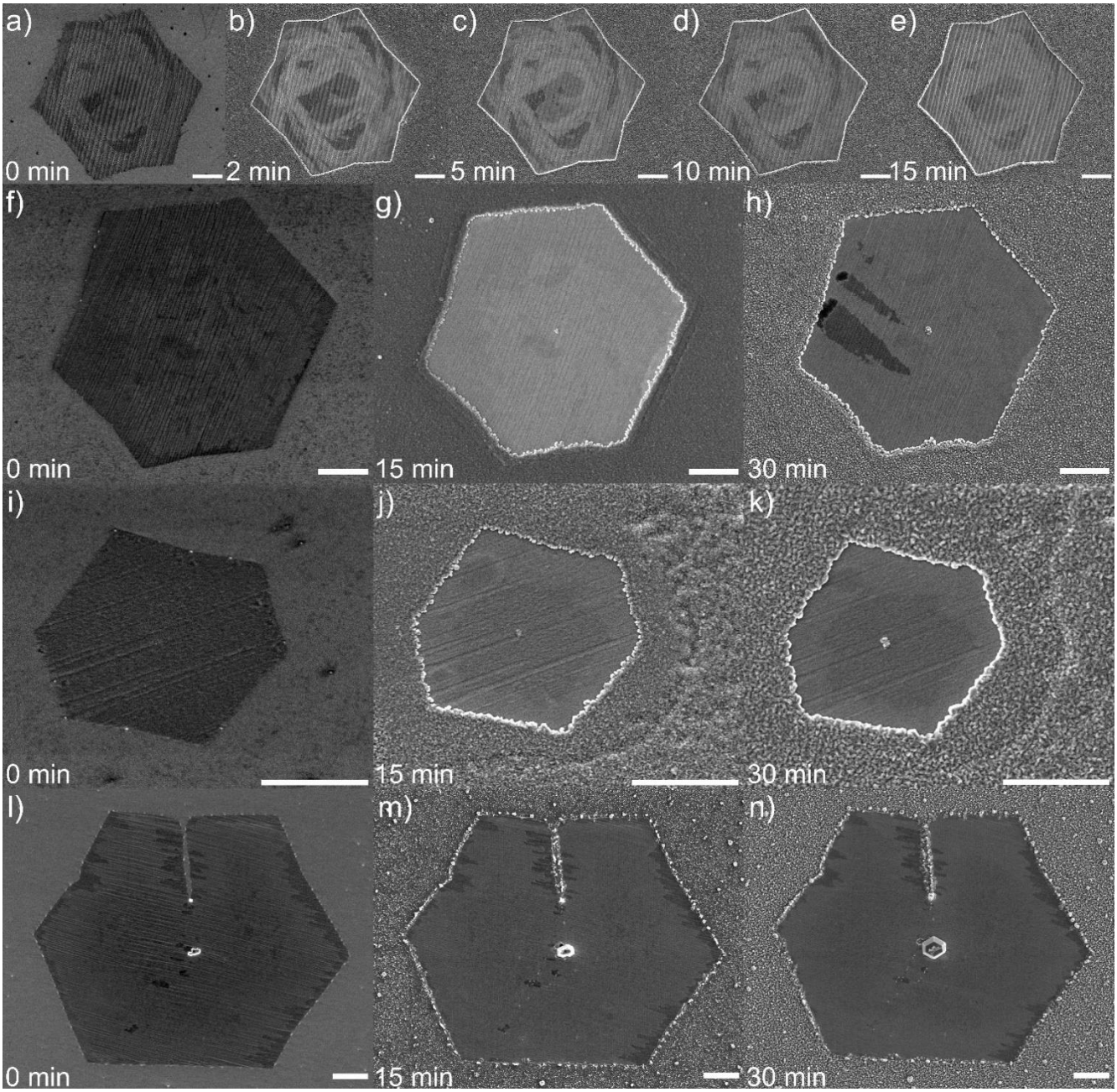

Figure 2.22. SEM images of graphene domains before treatment (0 min) and after repeated H_2S treatment. The total amount of H_2S treatment time is denoted in each SEM image. **(a-e)** No Cu_2S nanoparticle formation after repeated treatments. **(f-k)** The size of the Cu_2S nanoparticle formed at the nucleation center of domain increases with reaction time. **(l-n)** The Cu_2S nanoparticle emerges from a pre-existing impurity nanoparticle at the center and grows much larger with additional reaction time. In addition, a large straight crack is easily visible even before the H_2S treatment. Scale bar: 2 µm.

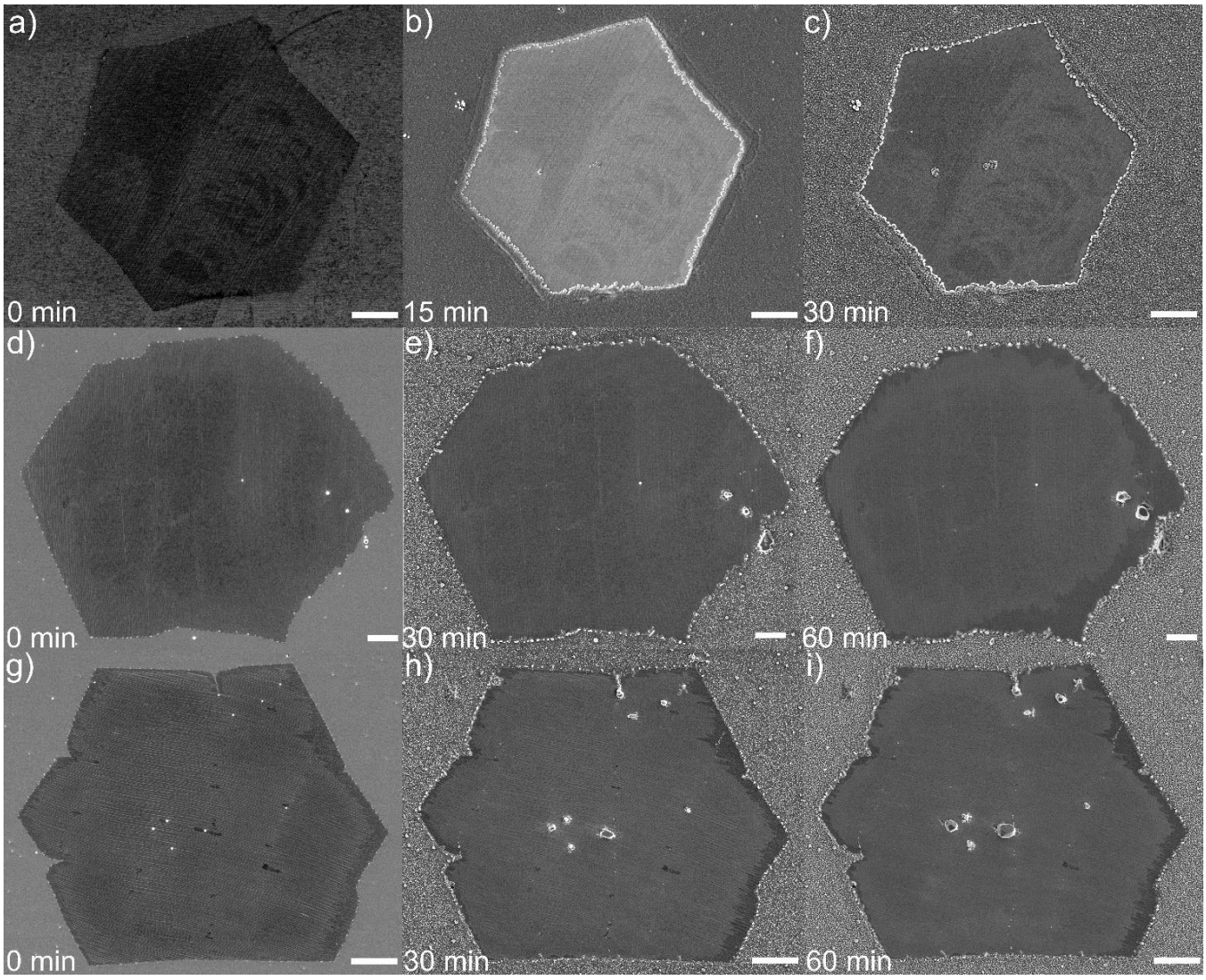

Figure 2.23. SEM images of graphene domains before treatment (0 min) and after repeated H_2S treatment. The total amount of H_2S treatment time is denoted in each SEM image. Multiple Cu_2S nanoparticles are formed in each graphene domain. Although the sizes of the Cu_2S nanoparticles generally increase with reaction time, some Cu_2S nanoparticles grow much faster than others within the same graphene domain. The different growth rates may originate from either the difference in vacancy defect sizes, or tight or loose binding of pre-existing SiO_x nanoparticles with surrounding defective graphene. Scale bar: 2 μm.

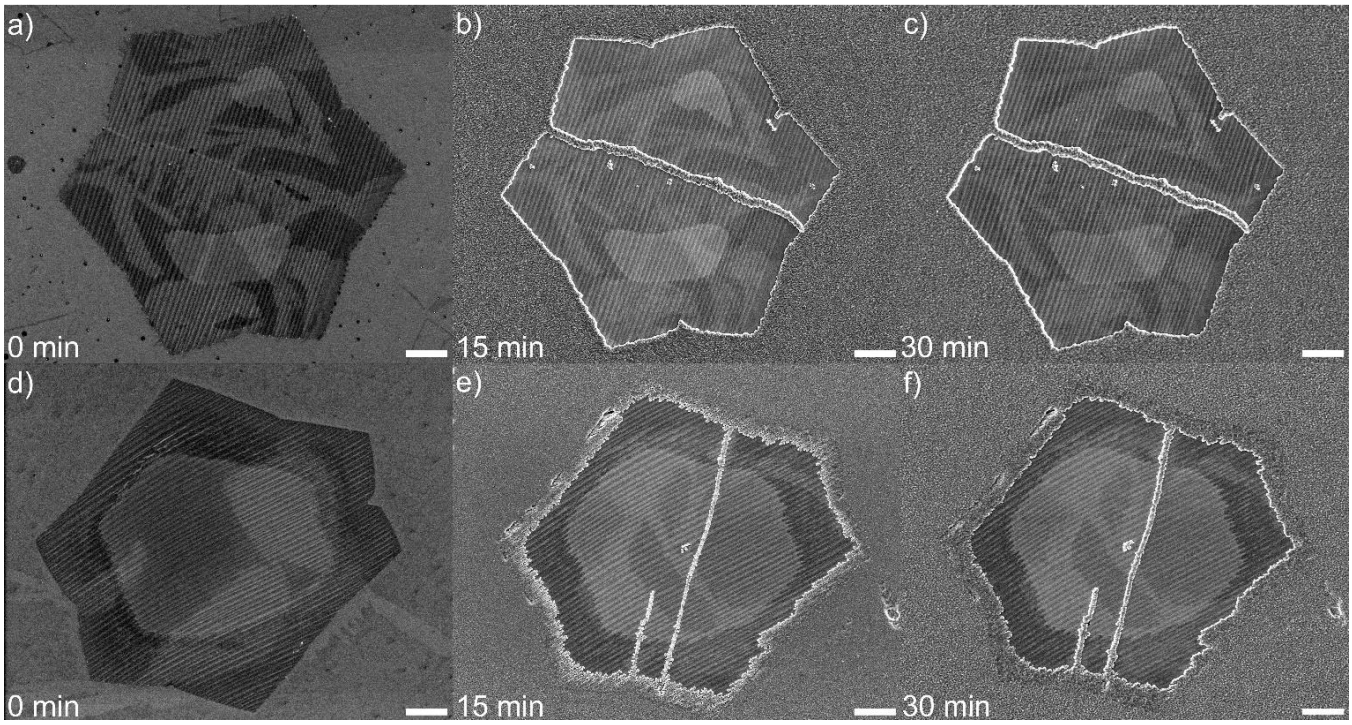

Figure 2.24. SEM images of graphene domains before treatment (0 min) and after repeated H_2S treatment. The total amount of H_2S treatment time is denoted in each SEM image. Both kinked and straight cracks can be visualized with formation of Cu_2S nanoparticles in the crack regions. The reaction time-dependent study shows that Cu_2S nanoparticles form rapidly and occupy all of cracked areas within 15 min of H_2S treatment. Further chemical treatment does not change the lengths of 1D Cu_2S nanowires, only increases their widths slightly. Scale bar: 2 μm.

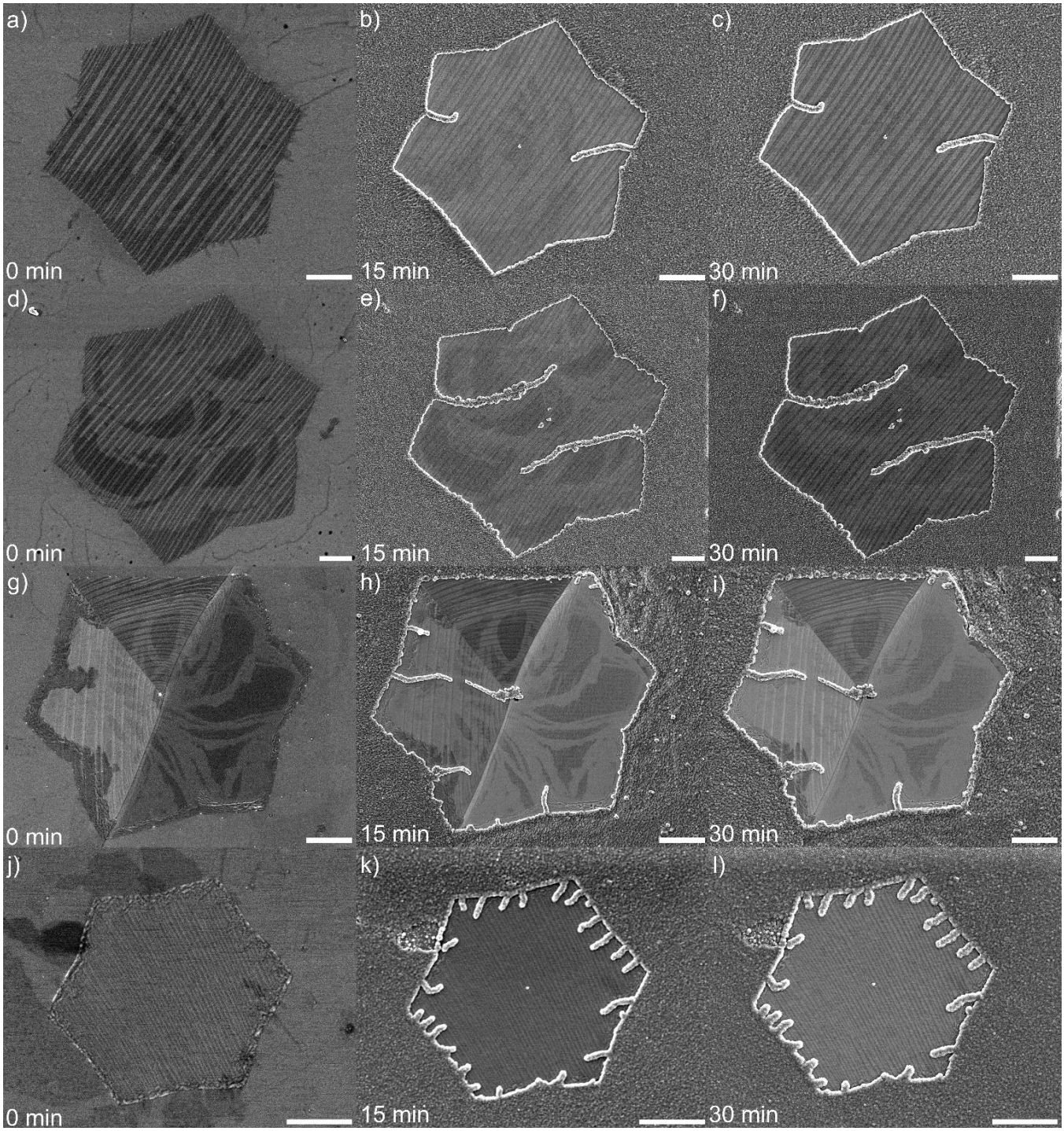

Figure 2.25. SEM images of graphene domains before treatment (0 min) and after repeated H_2S treatment. The total amount of H_2S treatment time is denoted in each SEM image. Both kinked and straight cracks can be visualized with formation of Cu_2S nanoparticles in the crack regions. The reaction time-dependent study shows that Cu_2S nanoparticles form rapidly and occupy all of cracked areas within 15 min of H_2S treatment. Further chemical treatment does not change the lengths of 1D Cu_2S nanowires, only increases their widths slightly. Scale bar: 2 μm.

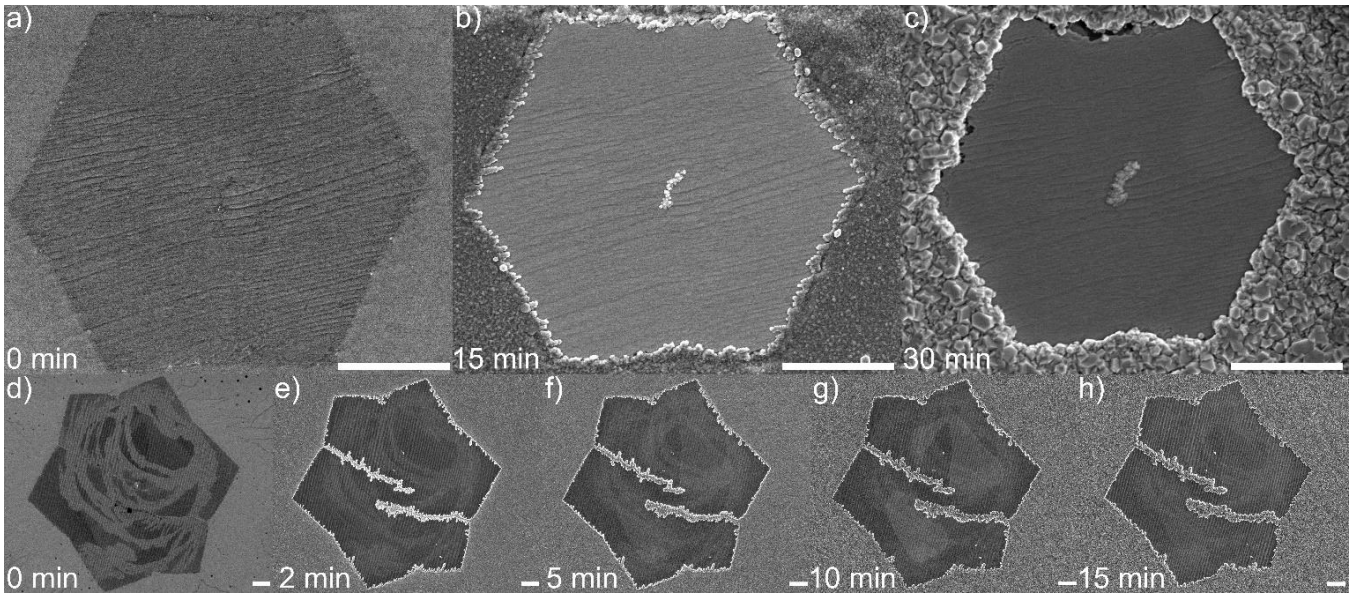

Figure 2.26. SEM images of graphene domains before treatment (0 min) and after repeated H_2S treatment. The total amount of H_2S treatment time is denoted in each SEM image. Cracks can be visualized with formation of Cu_2S nanoparticles in the crack regions. **(a-c)** Two cracks originate from domain center, resembling hour and minute hands in a clock. **(d-h)** Branched cracks. Scale bar: 2 μm.

To further investigate the potential effect of H_2S on graphene, we performed comparative Raman spectroscopy measurement in the same region on transferred hexagonal graphene domains on silicon wafer before and after the H_2S treatment. As shown in Figure 2.27, there is little change of Raman features of monolayer graphene after the H_2S treatment and 24h degassing under vacuum, suggesting minimum effects of H_2S on graphene in our experiments.

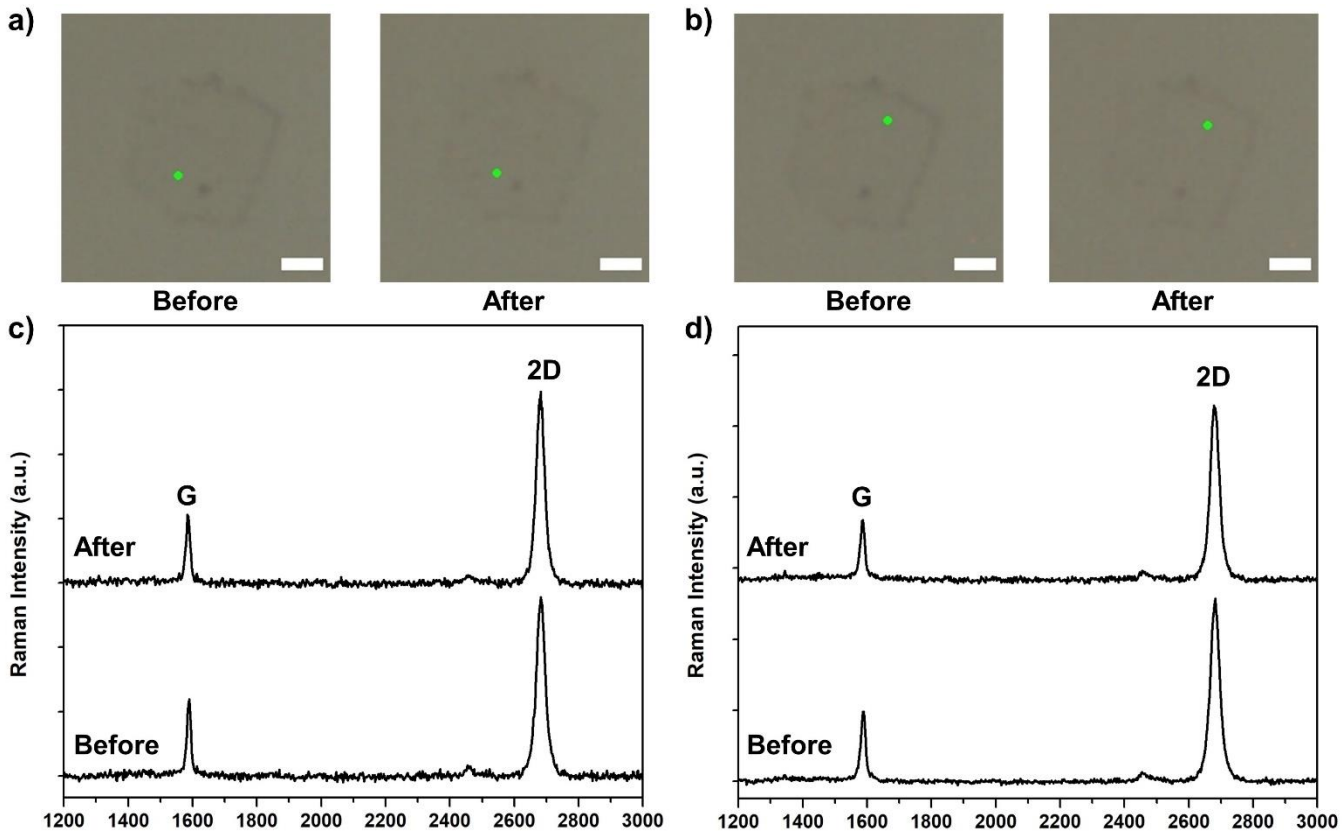

Figure 2.27. Representative Raman spectra of the monolayer graphene domain transferred onto Si wafer. **(a,b)** Microscopic optical images of the graphene domain on Si wafer and the green dots showing the first and second spots where the Raman spectra were taken, respectively. Scale bar: 2 μm. **(c)** Raman spectra on the same region of the first spot in the same graphene domain on Si wafer before (bottom) and after (top) 15 min of H_2S treatment. **(d)** Raman spectra on the same region of the second spot in the same graphene domain on Si wafer before (bottom) and after (top) 15 min of H_2S treatment. There is little change of Raman features of monolayer graphene after H_2S treatment.

2.3.5. Minimization of H_2S usage

We have been able to significantly reduce the amount of H_2S needed in the H_2S treatment. A typical H_2S treatment is similar to that in the section 2.2.4 except for the amounts of reagents used. 0.09 mL of freshly prepared 1 mg/mL $Na_2S.9H_2O$ solution, and 0.2 mL of 1.25 M H_2SO_4 were used for a 0.65 cm^2 of graphene sample, which corresponds to 0.02 mg of H_2S/cm^2 of graphene.

The freshly prepared $Na_2S.9H_2O$ solution should be used immediately to avoid potential decomposition in the air. As shown in Figure 2.28, a Cu_2S nanoparticle appears at the nucleation center of each of two graphene domains, respectively. In addition, the exposed copper substrate outside the graphene domain is fully covered with numerous Cu_2S nanoparticles, which indicates that 0.02 mg of H_2S/cm^2 of graphene is sufficient for chemical probing of graphene vacancy defects.

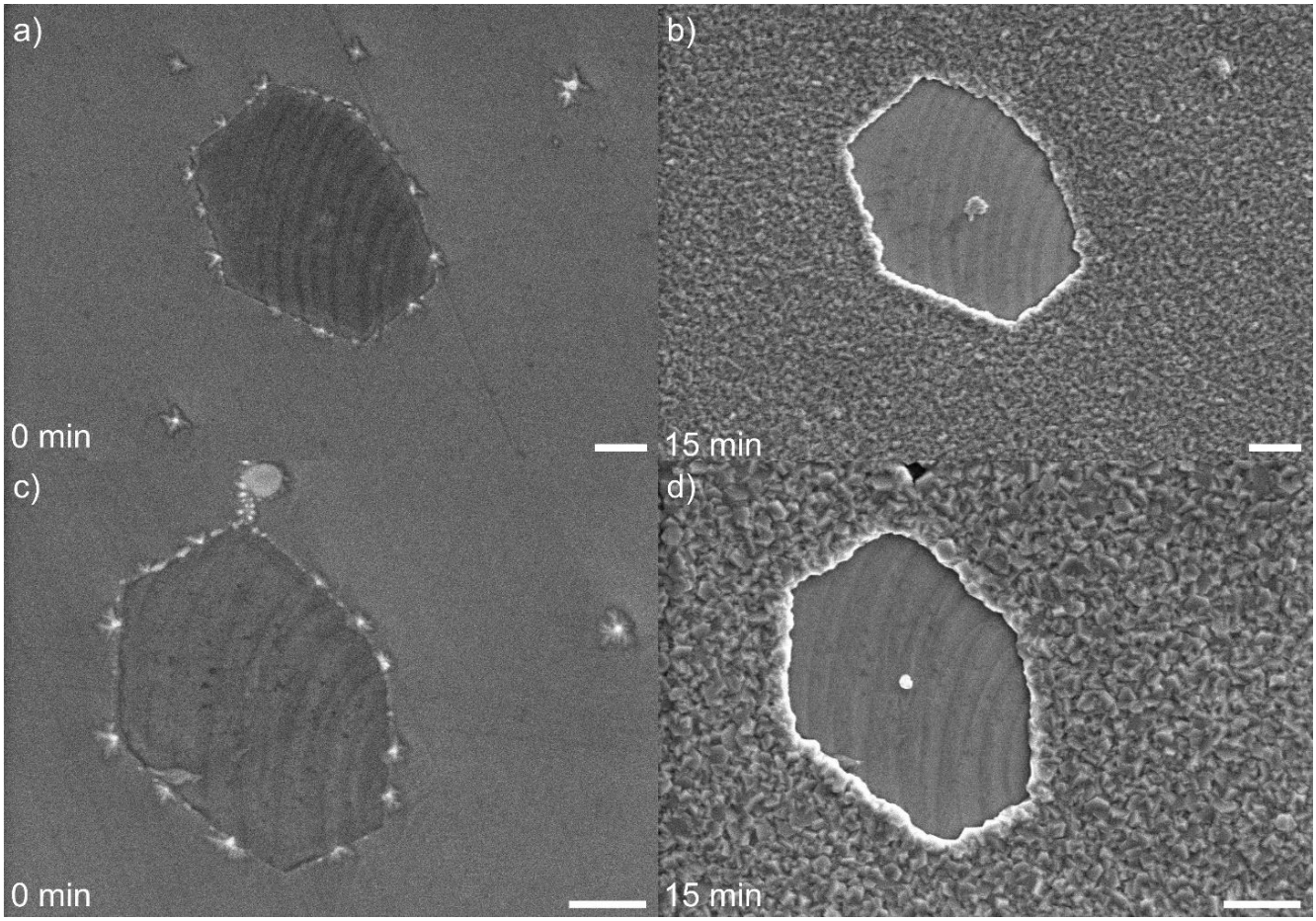

Figure 2.28. SEM images of graphene domains before treatment (0 min) and after 15 min of H_2S treatment using the minimum amount of H_2S gas produced *in situ*, corresponding to 0.02 mg of H_2S/cm^2 of graphene. A Cu_2S nanoparticle appears at the nucleation center of each of two graphene domains, respectively. In addition, the exposed copper substrate outside the graphene domain is fully covered with numerous Cu_2S nanoparticles, suggesting 0.02 mg of H_2S/cm^2 of graphene is sufficient for chemical probing of graphene vacancy defects. Scale bar: 0.5 µm.

Since the H_2S gas is toxic, the safety issue in using H_2S needs to be addressed in more details. According to the Occupational Safety and Health Administration (OSHA) standard, although H_2S is toxic, it only starts to show various effects at concentration higher than 2 ppm.[37]

To evaluate the safety of using H_2S, let's consider three scenarios: 1) In our standard H_2S treatment experiment which uses the large excessive amount of H_2S (section 2.2.4), 17 mg of H_2S is produced *in situ* inside the sealed vial in the fume hood. 2) We have also demonstrated that we can significantly reduce the amount of H_2S needed to 0.02 mg of H_2S/cm^2 of graphene (section 2.3.5 and Figure 2.24). For the 0.65 cm^2 of graphene sample, only 0.013 mg of H_2S produced *in situ* is found to be sufficient for chemical probing of graphene vacancy defects. 3) In a hypothetical scaled-up chemical probing scenario, for the 100 cm^2 of graphene sample, 2 mg of H_2S should be sufficient for chemical probing of graphene vacancy defects.

The ppm concentration of H_2S in air can be calculated according to the equation below.[38]

$$\text{Concentration (ppm)} = 24.45 \times \text{concentration (mg/m}^3) \div \text{molecular weight} \quad (1)$$

For a typical small two-person lab with ~ 100 m^3 of space volume, 17/0.013/2 mg of H_2S, *if completely leaked into the air in the two-person lab in the absence of a fume hood*, only corresponds to 0.12/0.00009/0.014 ppm of H_2S concentration, respectively, in aforementioned three scenarios, which is significantly lower than 2 ppm. Since all of our H_2S treatment experiments are carried out in the fume hood, *the concentration of potentially leaked H_2S in the two-person lab is much lower than the above fully leaked H_2S concentration*. Such extremely low concentration of potentially leaked H_2S (<< 0.12 ppm) has no toxic effects according to the OSHA standard ($\geq$ 2 ppm).[37] Furthermore, the H_2S gas can be conveniently prepared *in situ* by mixing $Na_2S.9H_2O$ with dilute H_2SO_4 solution, which eliminates the need of H_2S storage and

possibility of leaking of large amount of H_2S into the air. Moreover, *in situ* production of needed H_2S eliminates the necessity of storing a H_2S gas tank at the workplace. Based on these considerations, it is very safe to use our chemical probing method.

2.4. Conclusion

In conclusion, we have developed a new method for *in situ* chemical probing of vacancy defects such as holes and cracks in CVD-grown graphene. Our technique not only allows for fast probing of spatial distribution of vacancy defects in large area CVD-grown graphene samples, but also provides new insightful information on complex graphene cracking behaviors such as kinking, branching, and possibly ductile fracture. Our study also suggests that the copper grain and copper grain boundary play significant roles in formation and distribution of graphene vacancy defects. The observed discontinuous cracks more likely originate from a ductile fracture of graphene, which involves a plastic deformation ahead of the fracture. In the ductile fracture of conventional materials, the plastic deformation leads to formation of microvoids first, then followed by coalescence of microvoids to form a continuous crack.[20] The discontinuous cracks (Figure 2.15d, 2.17b, and 2.17d) resemble the “necklace” coalescence mode in the ductile failure (Figure 2.21e),[21] which suggests that they may be intermediate precursors to continuous cracks. In fact, we have noticed some examples where the continuous crack is immediately followed by oriented hole defects along the roughly same cracking direction (Figure 2.15d, 2.17b). The combination of extremely low concentration of potentially leaked H_2S (<< 0.12 ppm), sealed reactor in the fume hood, and *in-situ* production of H_2S makes it very safe to use our chemical probing method. Our approach could be extended to probe 2D

materials (graphene, h-BN, etc.) grown on a variety of metal substrates, because the H_2S is also known to react with other metals such as nickel, platinum, and silver.

2.5. References

(1) Graedel, T. E., J. *Electrochem. Soc.,* **1987***, 134*, 1632.

(2) Zhang, W.; Yang, S., *Acc. Chem. Res.,* **2009***, 42*, 1617.

(3) Choi, J.; Zhao, Y.; Kim, K. S.; Kim, K. S.; Kim, P.; Jang, H.; Lee, S. Y.; Ahn, J.; Hong, B. H.; Kim, J. M., *Nature*, **2009***, 457*, 706-710.

(4) Yuan, Q.; Gao, J.; Shu, H.; Zhao, J.; Chen, X.; Ding, F., *J. Am. Chem. Soc.,* **2012***, 134*, 2970-2975.

(5) Han, G. H.; Gunes, F.; Bae, J. J.; Kim, E. S.; Chae, S. J.; Shin, H. J.; Choi, J. Y.; Pribat, D.; Lee, Y. H., *Nano Lett*., **2011***, 11*, 4144-4148.

(6) Lisi, N.; Dikonimos, T.; Buonocore, F.; Pittori, M.; Mazzaro, R.; Rizzoli, R.; Marras, S.; Capasso, A., *Sci. Rep.,* **2017***, 7*, 9927-11.

(7) Girit, C. O.; Meyer, J. C.; Erni, R.; Rossell, M. D.; Kisielowski, C.; Yang, L.; Park, C. H.; Crommie, M. F.; Cohen, M. L.; Louie, S. G.; Zettl, A., *Science*, **2009***, 323*, 1705-1708.

(8) Lan, Y.; Chang, W.; Xiao, B.; Liang, B.; Chen, J.; Jiang, P.; Li, L.; Su, Y.; Zhong, Y.; Chen, C., *Small*, **2014***, 10*, 4778-4784.

(9) Zhang, T.; Li, X.; Gao, H., *Int J Fract*, **2015***, 196*, 1-31.

(10) Fujihara, M.; Inoue, R.; Kurita, R.; Taniuchi, T.; Motoyui, Y.; Shin, S.; Komori, F.; Maniwa, Y.; Shinohara, H.; Miyata, Y., *ACS Nano*, **2015***, 9*, 9027-9033.

(11) Zhang, B.; Mei, L.; Xiao, H., *Appl. Phys. Lett*, **2012***, 101*, 121915.

(12) Yu, Q.; Jauregui, L. A.; Wu, W.; Colby, R.; Tian, J.; Su, Z.; Cao, H.; Liu, Z.; Pandey, D.; Wei, D.; Chung, T. F.; Peng, P.; Guisinger, N. P.; Stach, E. A.; Bao, J.; Pei, S. S.; Chen, Y. P., *Nat. Mater*., **2011***, 10*, 443-449.

(13) Luo, Z.; Kim, S.; Kawamoto, N.; Rappe, A. M.; Johnson, A. T., *ACS Nano*, **2011***, 5*, 9154-9160.

(14) Vasilii I. Artyukhov; Yuanyue Liu; Boris I. Yakobson, *PNAS*, **2012***, 109*, 15136-15140.

(15) Kim, K.; Artyukhov, V. I.; Regan, W.; Liu, Y.; Crommie, M. F.; Yakobson, B. I.; Zettl, A., *Nano Lett*., **2012***, 12*, 293-297.

(16) Mohsin, A.; Liu, L.; Liu, P.; Deng, W.; Ivanov, I. N.; Li, G.; Dyck, O. E.; Duscher, G.; Dunlap, J. R.; Xiao, K.; Gu, G., *ACS Nano*, **2013***, 7*, 8924-8931.

(17) Na, S. R.; Wang, X.; Piner, R. D.; Huang, R.; Willson, C. G.; Liechti, K. M., *ACS Nano*, **2016***, 10*, 9616-9625.

(18) Jia, X.; Campos-Delgado, J.; Terrones, M.; Meuniere, V.; Dresselhaus, M.S., *Nanoscale*, **2011***, 3*, 86-95.

(19) Omeltchenko, A.; Yu, J.; Kalia, R. K.; Vashishta, P., *Phys. Rev. Lett.,* **1997***, 78*, 2148-2151.

(20) Zhang, B.; Xiao, H.; Yang, G.; Liu, X., *Eng. Fract. Mech.,* **2015***, 141*, 111-119.

(21) Benzerga, A. A.; Leblond, J., *Adv. Appl. Mech*., **2010***, 44*, 169-305.

(22) Nardelli, M. B.; Yakobson, B. I.; Bernholc, J., *Phys. Rev. Lett*., **1998***, 81*, 4656-4659.

(23) Dumitrica, T.; Hua, M.; Yakobson, B. I., *Proc. Natl. Acad. Sci. U.S.A.*, **2006***, 103*, 6105-6109.

(24) Xu, Z., *J. Comput. Theor. Nanosci.,* **2009***, 6*, 625-628.

(25) Huang, P. Y.; Ruiz-Vargas, C. S.; van der Zande, A M; Whitney, W. S.; Levendorf, M. P.; Kevek, J. W.; Garg, S.; Alden, J. S.; Hustedt, C. J.; Zhu, Y.; Park, J.; McEuen, P. L.; Muller, D. A., *Nature*, **2011***, 469*, 389-392.

(26) Li, X.; Cai, W.; An, J.; Kim, S.; Nah, J.; Yang, D.; Piner, R.; Velamakanni, A.; Jung, I.; Tutuc, E.; Banerjee, S. K.; Colombo, L.; Ruoff, R. S., *Science*, **2009***, 324*, 1312-1314.

(27) D. L. Duong, G. H. Han, S. M. Lee, F. Gunes, E. S. Kim, S. T. Kim, H. Kim, Q. H. Ta, K. P. So, S. J. Yoon, S. J. Chae, Y. W. Jo, M. H. Park, S. H. Chae, S. C. Lim, J. Y. Choi, Y. H. Lee, *Nature*, **2012***, 490*, 235-239.

(28) Wang, Z.; Weinberg, G.; Zhang, Q.; Lunkenbein, T.; Klein-Hoffmann, A.; Kurnatowska, M.; Plodinec, M.; Li, Q.; Chi, L.; Schloegl, R.; Willinger, M., *ACS Nano*, **2015***, 9*, 1506-1519.

(29) Gwan-Hyoung Lee; Ryan C. Cooper; Sung Joo An; Sunwoo Lee; Arend van der Zande; Nicholas Petrone; Alexandra G. Hammerberg; Changgu Lee; Bryan Crawford; Warren Oliver; Jeffrey W. Kysar; James Hone, *Science*, **2013***, 340*, 1073-1076.

(30) Dong, J.; Wang, H.; Peng, H.; Liu, Z.; Zhang, K.; Ding, F., *Chem. Sci*., **2017***, 8*, 2209-2214.

(31) Murdock, A. T.; Koos, A.; Britton, T. B.; Houben, L.; Batten, T.; Zhang, T.; Wilkinson, A. J.; Dunin-Borkowski, R. E.; Lekka, C. E.; Grobert, N., *ACS Nano*, **2013***, 7*, 1351-1359.

(32) Xu, L.; Wei, N.; Zheng, Y., *Nanotechnology*, **2013***, 24*, 505703

(33) Dewapriya, M. A. N.; Rajapakse, R. K. N. D, *J. Appl. Mech.*, **2014***, 81*, 81010.

(34) Lin, L.; Deng, B.; Sun, J.; Peng, H.; Liu, Z., Chem. Rev., **2018***, 118*, 9281-9343.

(35) Hegde, V. I.; Shirodkar, S. N.; Tit, N.; Waghmare, U. V.; Yamani, Z. H., *Surf. Sci.,* **2014***, 621*, 168-174.

(36) Reshak, A. H.; Auluck, S., *J. Appl. Phys.,* **2014***, 116*, 103702.

(37) The OSHA standard on H_2S. *https://www.osha.gov/SLTC/hydrogensulfide/hazards.html* (accessed April, 2018).

(38) Calculation of the ppm concentration of a gas in air. *https://cfpub.epa.gov/ncer_abstracts/index.cfm/fuseaction/display.files/fileID/14285* (accessed April, 2018).

Chapter 3: Preliminary investigation of Origins of Vacancy Defects in CVD-Grown Graphene

3.1. Introduction

As discussed in chapter 2, Our technique not only allows for fast probing of spatial distribution of vacancy defects in large area CVD-grown graphene samples, but also provides new insightful information on complex graphene cracking behaviors such as kinking, branching, and possibly ductile fracture. Our study also suggests that the copper grain and copper grain boundary play significant roles in formation and distribution of graphene vacancy defects. The observed discontinuous cracks more likely originate from a ductile fracture of graphene, which involves a plastic deformation ahead of the fracture. In the ductile fracture of conventional materials, the plastic deformation leads to formation of microvoids first, then followed by coalescence of microvoids to form a continuous crack.[1] The discontinuous cracks (Figure 2.15d, 2.17b, and 2.17d) resemble the "necklace" coalescence mode in the ductile failure (Figure 2.21e),[2] which suggests that they may be intermediate precursors to continuous cracks. In fact, we have noticed some examples where the continuous crack is immediately followed by oriented hole defects along the roughly same cracking direction (Figure 2.15d, 2.17b).

However, there are other possible sources such as graphene wrinkles that may contribute to the formation of vacancy defects in CVD-grown graphene. In this chapter, we have performed further study to understand the origins of vacancy defects.

A common issue with the CVD-grown graphene on a metal substrate is ubiquitous surface corrugation at the metal and graphene interface and formation of graphene wrinkles.[3] Beside grain boundaries, the wrinkles are the other type of line defects that is widely observed

in graphene produced by CVD. Initiation of the growth of graphene in CVD process often requires high temperature, about 1000 °C, and at this temperature, surface copper layer becomes melted and pre-existing surface features disappears.[4] This helps flexible graphene to be conformal with copper surface and to be strain-free.[3] After growth and during cooling, the strain is induced at the copper and graphene interface due to thermal expansion coefficient difference between copper ($\alpha_{Cu} = 18 \times 10^{-6}\ K^{-1}$) and graphene ($\alpha_{graphene} \approx -7 \times 10^{-6}\ K^{-1}$).[3,5] Whereas copper substrate is under tensile stress caused by thermal expansion of graphene, the graphene experiences compressive stress by the contraction of copper, simultaneously. This results in copper surface roughening and formation of graphene wrinkles.[3,6] The reconstructed copper surface lines that are visible under graphene is referred as copper step bunches (CuSB) or the copper surface stripes in the literature.[3-5,7,8] The aligned copper steps formation upon cooling relieves strain in one direction and the strain in perpendicular direction is relieved by wrinkle formation. Figure 3.1 shows graphene wrinkles that are generally perpendicular to CuSB.[3]

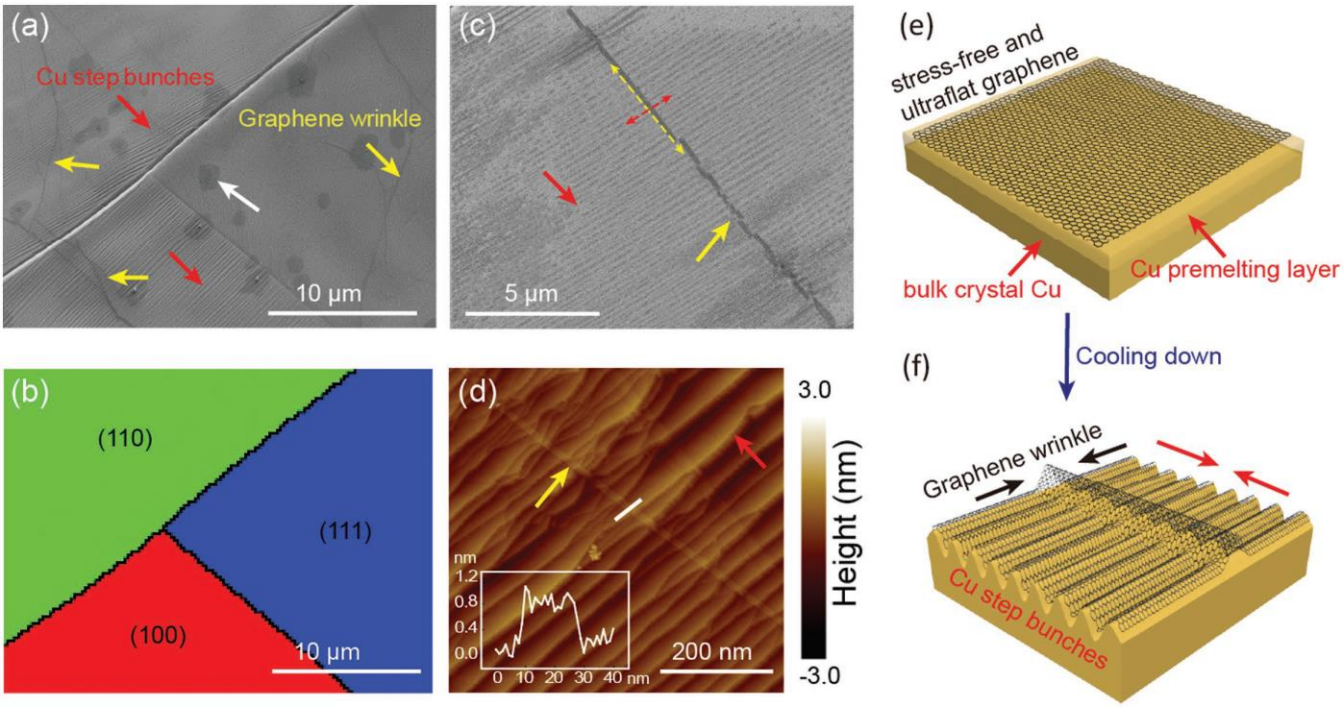

Figure 3.1. The orientation relationship between copper step bunches (copper surface stripes) and graphene wrinkles. **(a)** SEM and **(b)** Electron back scattering diffraction (EBSD) images of graphene grown on polycrystalline Cu foil. The red, yellow, and white arrows show Cu step bunches, graphene wrinkles, and graphene adlayers, respectively. **(c)** SEM image of a graphene wrinkle, showing graphene wrinkle and copper step bunches are nearly perpendicular to each other. **(d)** AFM image of a graphene wrinkle. Inset shows the height profile along the white line. (e) Illustration of ultraflat graphene on Cu with a premelting layer. (f) Illustration of the corrugation process during cooling. The black and red arrows indicate the buckling of graphene and the surface roughening of Cu, respectively.[3]

The graphene chemical reactivity significantly increases due to local curvature caused by rippling or wrinkling.[9] This is similar to the increased reactivity at the end caps of pristine carbon nanotubes (CNTs). The curvature at the end caps of CNTs causes a loss of spatial overlap of the atomic p orbitals that contribute to conjugation and a shift in hybridization of the atoms from the sp^2 of graphite to something intermediate between sp^2 and sp^3. This results in an increase in energy locally and an introduction of partial radical character in the π-bonding electrons.[10] Addition reactions require out-of-plane bending of three-coordinate carbon atoms

(Figure 3.2a). As the reactant carbon atoms shift from three to four coordinate, the local preferred geometry shifts from planar to tetrahedral. Further, any local conjugation is broken, and the carbon atoms' hybridization change from sp^2 to sp^3. The energy required to induce such curvature, commonly called strain energy, can therefore be considered as energy already there due to pyramidalization (Figure 3.2b) for an addition reaction, thus enhancing reactivity selectively at the highly curved sites.[10]

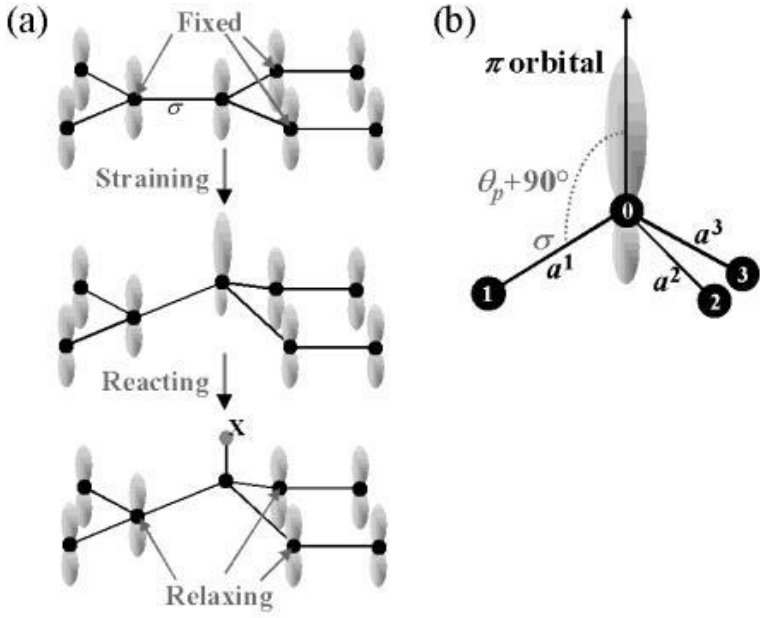

Figure 3. 2. (a) Steps of a reaction on a graphene sheet. (b) Pyramidalization: the π orbital and three σ bonds describe pyramidalization.[11]

The source of graphene's chemical inertness comes, in part, from the reduced strain present in its sp^2 network due to its planar structure.[12] There is a reaction barrier for the carbon atoms in the graphene sheet due to the need of stretching strong carbon-carbon bonds. However, carbon atoms in the vicinity of curvature area are already slightly out of plane and thus have reduced reaction barrier with the incoming atoms.[13] Therefore, ripples, wrinkles and folded wrinkles could have carbon atoms with increased chemical reactivity compared to the carbon atoms in flat graphene areas. The storage of graphene in air even as short as one week

causes oxidation of copper from the position of graphene wrinkles.[3] The oxidation of copper requires at least a nanoscale entry point in the position of graphene wrinkles for the oxygen and water molecules' access to the copper surface.[3] Therefore, CVD-grown graphene is prone to defect formation on the wrinkle locations by time depending on the storage conditions.[3,14]

The surface corrugations, which prevents the monolayer from collapsing, are intrinsic to graphene. Based on the physical dimensions, different types of corrugations can be defined, such as graphene ripples, wrinkles and folds.[14] Graphene ripples have a length/width aspect ratio close to 1 and a height less than 1 nm; they act as out-of-plane deformations stabilizing the graphene sheet. Graphene wrinkles have an aspect ratio larger than 1 and can have a length of up to a few micrometers.[14] Graphene wrinkles are formed when graphene experiences a uniaxial exterior force due to the interaction between the metallic substrate and graphene during cooling stage of CVD.[15] Graphene folds can be described as collapsed wrinkles. When the wrinkle exceeds the critical height, it bends and collapses upon the fold formation.[14] Moreover, graphene folds or folded wrinkles are usually longer than wrinkles with tens of microns in length.[16]

The relatively weak Van der Waals interaction between graphene and copper surface permits slipping and delamination of graphene under strain.[7] The delaminated graphene can form different wrinkle morphologies. When a ripple gets taller, due to Van der Waals interactions between layers of excessively buckled graphene, it can turn into a standing collapsed wrinkle or folded wrinkle.[16] Therefore, folded wrinkles provide a multilayer of adhered graphene layers due to Van der Waals interactions between layers of graphene. Furthermore, folded wrinkles can be more protective over the substrate underneath by effectively limiting the accessibility of the substrate.[17]

The types of graphene wrinkle morphologies are illustrated in Figure 3.3. While standing collapsed wrinkles are narrow and high, folded wrinkles are large in width and have a low height.[7]

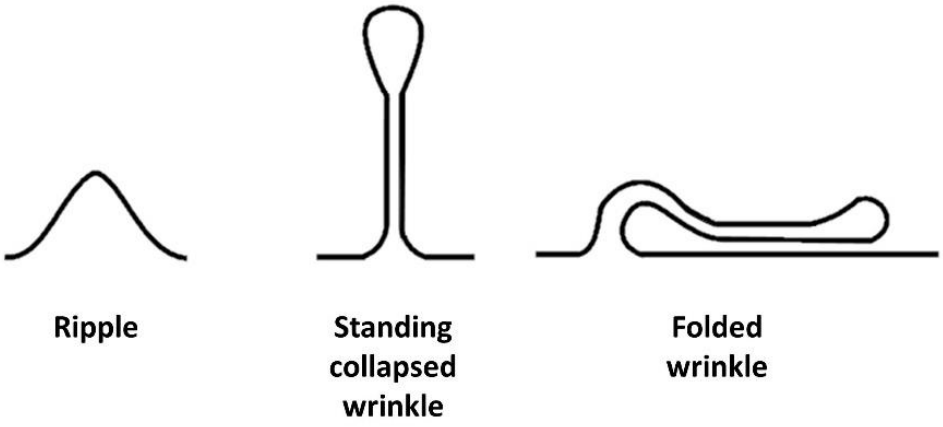

Figure 3.3. Illustrations of simple ripple, standing collapsed wrinkle and folded wrinkle on graphene grown by chemical vapor deposition.

The Backscattered electron (BSE) imaging mode primarily detects elastically scattered electrons formed during interaction between an accelerated electron beam and a sample. BSE, when used with low accelerating voltages (such as under 5 kV), is useful for observing surface details of the samples. When high probe current and low accelerating voltage is employed, the interaction volume of the electron beam with the target sample is reduced. Thus, the surface detail and contrast are enhanced.[18] An SEM system equipped with a backscattered electron detector can be used to better visualize graphene wrinkles on copper foil.[19] In SEM-BSE images (Figure 3.4b), the dark lines with larger-width may indicate folds and the dark lines with the smaller-width may indicate standing collapsed wrinkles. While larger-width or folded wrinkles are sometimes visible in SEM images, smaller-width wrinkles can be more obvious in SEM-

BSE images with the similar imaging conditions (such as same accelerating voltage, working distance).

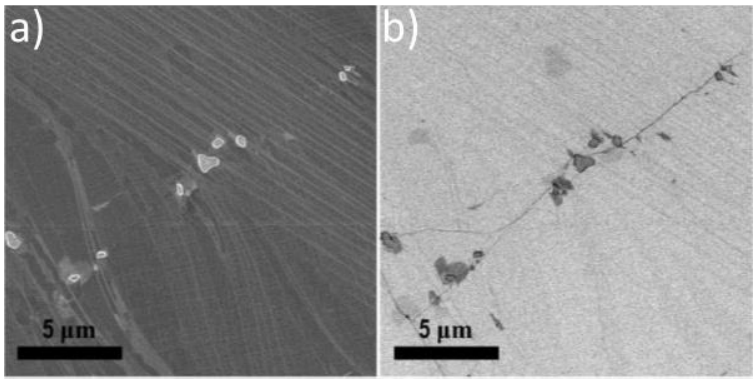

Figure 3.4. (a) SEM image of monolayer graphene on copper film. The subtle surface features such as graphene wrinkles are not obvious. **(b)** SEM-BSE image of the same region in **(a)**. The graphene wrinkles that are not visible or partially visible in **(a)** are obvious.[19]

Recently, Kwak and coworkers proposed another resource that is responsible for the observation of vacancy defects. They found that wrinkle is the main source of hole defects in CVD-grown polycrystalline graphene. Kwak *et al.* studied nanosized defects in a CVD-grown graphene by observing etching pits in the copper substrate.[19] Their method relays on dipping graphene on copper sample in 10 v/v% HCl aqueous solution and etching copper through graphene defects to identify the holes in graphene samples. However, this method includes interaction of liquids with graphene and introduction of surface tension effects and possible impurities on graphene which may result in new defects on graphene that is only one atom-thick sheet. Besides, carbon atoms have increased chemical reactivity in the strained locations such as wrinkles than flat locations in graphene.[9] Also, the created etch pits in their study that can be seen in figure 3.5 have a size in microscale, which is likely bigger than mentioned nanoholes that is being identified. Their conclusion is that nanosized holes in the CVD-grown graphene on copper foil are primarily concentrated on graphene wrinkles.[19]

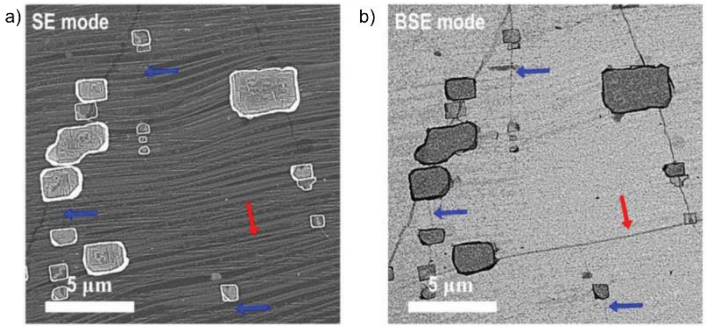

Figure 3. 5. (a) An SEM image of the graphene on copper surface after dipping in an aqueous HCl solution for 10 minutes. **(b)** BSE mode image of the same region in (a). Blue and red arrows indicate wrinkles in the images.[19]

To understand the origins of defects in CVD-grown graphene is crucial in order to minimize or eliminate them. However, due to the difficulty on large scale probing of vacancy defects there is only limited understanding on the origins of vacancy defects. As described in Chapter 2, we have observed a variety of vacancy defects such as holes, continuous and discontinuous cracks. In addition, our technique not only allows for fast probing of spatial distribution of vacancy defects in large area CVD-grown graphene samples, but also provides new insightful information on complex graphene cracking behaviors such as kinking, branching, and possibly ductile fracture. Also, our study suggests that the copper grain and copper grain boundary play significant roles in formation and distribution of graphene vacancy defects. The observed discontinuous cracks most likely originate from a ductile fracture of graphene, which involves a plastic deformation probably at high temperature during the CVD process, leading to the formation of orientated nanoscale hole defects before the fracture. This is similar to the ductile fracture of conventional materials, where the plastic deformation leads to formation of microvoids first, then followed by coalescence of microvoids to form a continuous crack. However, as reported by Kwak and coworkers, there are other possible sources such as graphene wrinkles that may contribute to the formation of vacancy defects in polycrystalline CVD-grown graphene[19]. In this chapter, our goal is to clarify whether graphene wrinkles are

responsible for the formation of observed vacancy defects in our polycrystalline and single crystalline CVD-grown graphene samples, respectively.

The SEM-BSE images provide more surface details for graphene on copper samples. This is a very useful method to get more information about the smaller-width wrinkles that aren't obvious in SEM images. To image graphene wrinkles better, we used SEM-BSE in conjunction with standard SEM imaging. Since the origins of vacancy defects may be different in polycrystalline graphene and single crystalline graphene, we studied and clarified potential effects of graphene wrinkles on the formation of vacancy defects in both types of graphene samples using our chemical probing method.

3.2 Experimental

The CVD-grown monolayer graphene samples on copper foil were purchased from ACS Materials Inc. Sodium sulfide nonahydrate ($Na_2S.9H_2O$) and sulfuric acid (H_2SO_4) (6.00 N) were purchased from MP Biomedicals and Ricca Chemical Company, respectively.

3.2.1 Characterization

SEM imaging and EDX analysis were performed using a Hitachi S-4800 field emission scanning electron microscope equipped with a back-scattered electron (BSE) detector under high vacuum ($<10^{-3}$ Pa). All SEM and SEM-BSE experiments were carried out under the same conditions. SEM-BSE experiments were performed by using emission current of 10 μA and accelerating voltage of 1 keV with a working distance of about 3 mm.

3.2.2 H_2S treatment of graphene on copper foil

In a typical experimental procedure, a piece of graphene on copper was cut for initial SEM and SEM-BSE imaging (0 min). After imaging, the graphene sample was placed upright in a 4 mL glass vial. The size of the graphene on copper piece and the vial allows almost similar standing angle for the graphene piece in every experiment. Thus, the accessibility of the piece by H_2S gas is similar between different experiments. A 20 mL vial with a larger diameter was charged with 120 mg $Na_2S.9H_2O$. Then the 4 mL vial with graphene sample in it was placed inside the 20 mL vial. The reaction setup was similar to the one showed in Figure 2.1 in Chapter 2. After that, the 20 mL vial was sealed using a matching screw cap with PTFE/silicone septum. Finally, 0.5 mL of 0.5 M H_2SO_4 solution was quickly injected into the 20 mL vial via a syringe through the septum. Then the reaction setup was immediately placed in dark during the reaction. After certain amount of time (e.g. 15 min), the reaction was stopped by opening the vial and removing the graphene sample. Subsequently, the H_2S-treated graphene sample was placed under vacuum in dark for about 24 h, in order to remove any potential residual H_2S gas adsorbed on the surface. Later, the chemically treated graphene sample was imaged by SEM for the second time at the same spots as the first SEM imaging. The acquired SEM and SEM-BSE images were denoted with total amount of reaction time the graphene sample experienced (e.g. 15 min).

3.3 Results and Discussion

3.3.1 The relationship between discontinuous cracks and wrinkles in polycrystalline graphene films

Figure 3.6 shows SEM and SEM-BSE images graphene samples before H_2S gas treatment and SEM images after H_2S gas treatment. The larger-width wrinkles or folds are

obviously visible in SEM images as larger dark lines (Figure 3.6a, d, g, j). The thinner dark lines which represent smaller-width wrinkles become more visible with SEM-BSE imaging (Figure 3.6b, e, h, k). After H_2S gas treatment, Cu_2S particles formed majorly on thinner dark lines, which indicates wrinkles. The blue arrows show some of the newly formed Cu_2S particles that are on a wrinkle (Figure 3.6c, f, i, l). There is no particle formation on larger-width wrinkles. This suggests that larger-width wrinkles or folded wrinkles are more protective over copper by limiting H_2S access to the copper surface. Nevertheless, there are newly formed particles that are not on a wrinkle (shown by orange arrows). The thinner lines or smaller-width wrinkles are preferred locations for formation of particles which suggests the existence of graphene vacancy defects on the wrinkles. Therefore, it can be said that wrinkles are detrimental to the production of high-quality CVD-grown graphene. Furthermore, it is important to pay attention to reduce or eliminate wrinkles in order to produce excellent graphene samples with lower density of defects.

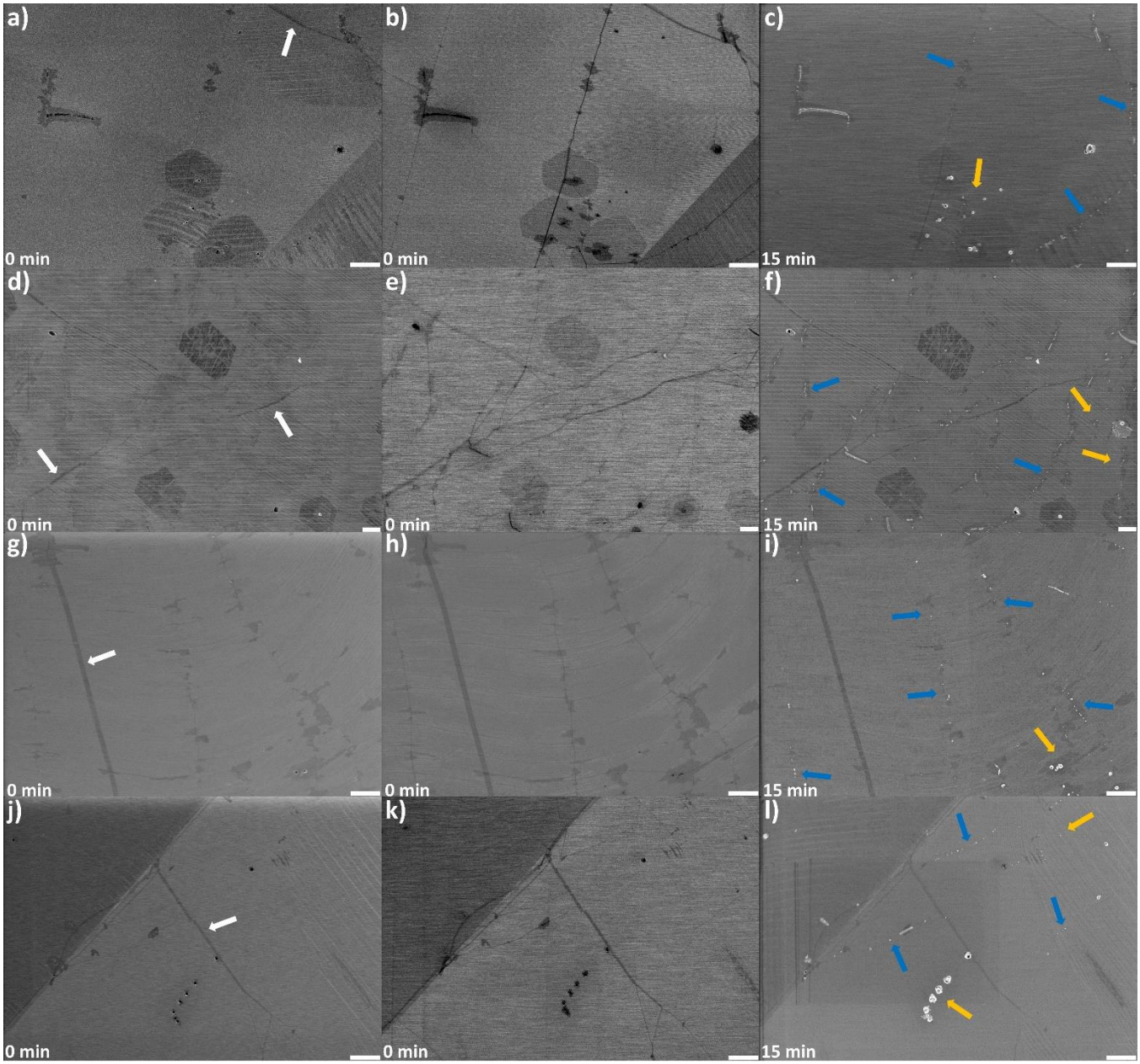

Figure 3.6. SEM and SEM-BSE images graphene on copper samples before H_2S gas treatment and SEM images after 15 minutes of H_2S gas treatment. **(a,d,g,j)** SEM images of polycrystalline graphene on copper before H_2S treatment. The white arrows indicate large wrinkles or larger parts of the wrinkles. **(b,e,h,k)** SEM-BSE images of the approximately same region in **(a,d,g,j)** before H_2S treatment. The smaller-width wrinkles are better visible in SEM-BSE images which are not obvious in SEM images in **(a,d,g,j)**. **(c,f,i,l)** SEM images of the approximately same region after 15 minutes of H_2S treatment. The blue arrows show areas that new particles formed on the wrinkles. The orange arrows show new particles formed not on the wrinkles. The thinner lines, that are smaller-width wrinkles, are the preferred locations for the formation of Cu_2S particles. Scale bar: 2 μm.

Figure 3.7 presents more examples of the discontinuous defects on smaller-width wrinkles of graphene film on copper foil. After H_2S treatment, the Cu_2S particles are formed on the dark regions on thinner lines, indicated by the blue arrows in (Figure 3.7c, f). This suggests that the dark areas on smaller-width wrinkles are generally indicative of vacancy defects. Also, these dark regions mostly take place on smaller-width wrinkles but not on larger-width wrinkles or folded wrinkles.

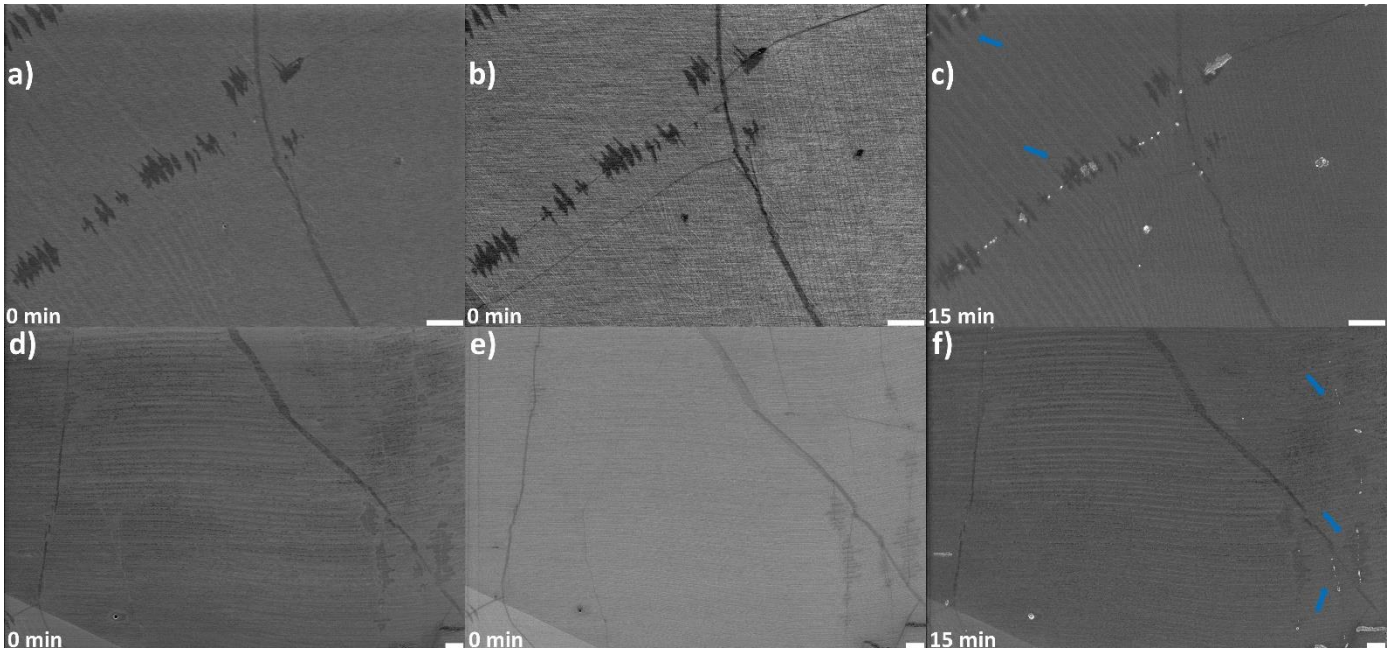

Figure 3.7. SEM and SEM-BSE images graphene on copper samples before H_2S treatment and SEM images after 15 minutes of H_2S gas treatment. **(a,d)** SEM images of polycrystalline graphene on copper before H_2S treatment. **(b,e)** SEM-BSE images of the approximately same region in **(a,d,g,j)** before H_2S treatment. **(c,f)** SEM images of the approximately same region after 15 minutes of H_2S treatment. The blue arrows show areas that new particles formed on the dark regions on thinner lines. The dark spots on thinner lines, that are smaller-width wrinkles, are generally the preferred locations for the formation of Cu_2S particles. Scale bar: 2 µm.

3.3.2 The relationship between discontinuous cracks and wrinkles in hexagonal graphene domains

In the study by Kwak *et al.*, vacancy defects are found on wrinkles in polycrystalline graphene. Our investigations of vacancy defects in Chapter 2 show that mechanical stress is the main source of vacancy defects in single crystalline and polycrystalline graphene, not enhanced chemical reactivity. We observed discontinuous cracks most likely originate from a ductile fracture of graphene, which involves a plastic deformation probably at high temperature during the CVD process, leading to the formation of orientated nanoscale hole defects before the fracture. In CVD process, hexagonal monolayer graphene domains are single crystalline while graphene films are polycrystalline with the merging of growing domains. Therefore, it is important to study polycrystalline and single crystalline graphene samples to have a better understanding of the effects of wrinkles on the formation of vacancy defects. In contrast to polycrystalline graphene samples, we have found that wrinkles are not mainly responsible for the formations of vacancy defects in hexagonal single crystalline graphene domains.

3.3.2.1 The hexagonal graphene domains with wrinkle and no discontinuous crack

Wrinkles are not commonly observed in hexagonal graphene domains compared to polycrystalline graphene films. Only 25% of all hexagonal graphene domains that are investigated in our study showed wrinkle line in SME-BSE images. Figure 3.8 shows an example of hexagonal graphene domain with wrinkle lines and no particles formed on the wrinkles, but particles observed in possible nucleation center and close to the edge of the domain (indicated by orange arrows in figure 3.8c). There is no particle formation on the wrinkles which is indicated by the white arrows in figure 3.8b.

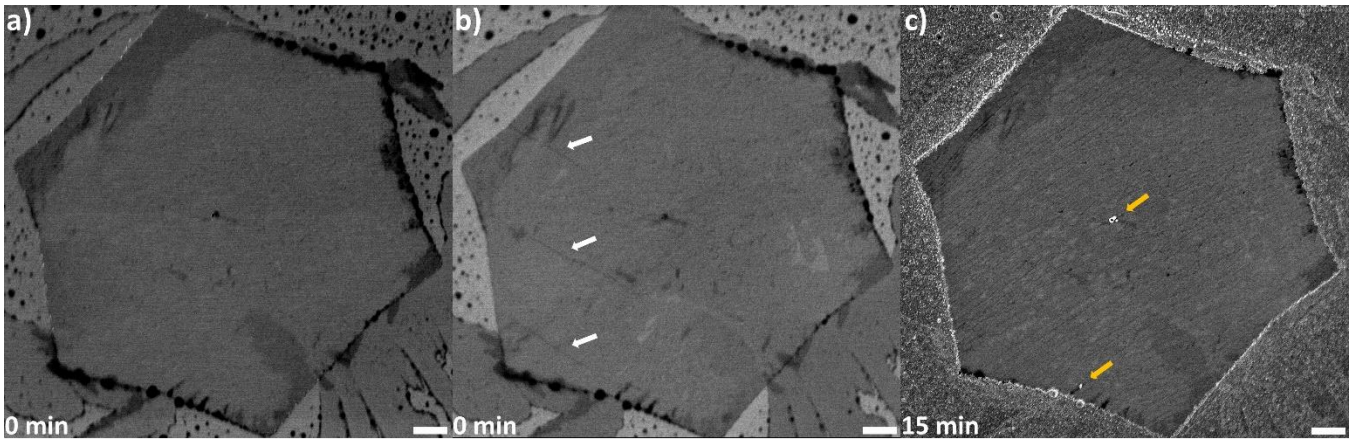

Figure 3.8. SEM and SEM-BSE image hexagonal graphene domain on copper before H_2S treatment and SEM image after 15 minutes of H_2S gas treatment. **(a)** SEM image of hexagonal graphene domain on copper before H_2S treatment. The wrinkles are not visible. **(b)** SEM-BSE image of the same region in **(a)**. The white arrows indicate graphene wrinkles. **(c)** SEM image of the same region in **(a,b)** after 15 minutes of H_2S treatment. There is no discontinuous crack, but particle formation at vacancy defect locations which are indicated by orange arrows. Scale bar: 1 µm.

3.3.2.2 The discontinuous cracks in the absence of wrinkles in the hexagonal graphene domains

In hexagonal graphene domains, discontinuous cracks are observed even though there is no graphene wrinkle (Figure 3.9). Also, nanoscale vacancy defects are observed in single crystalline hexagonal graphene domains in the absence of graphene wrinkles. This shows that wrinkles are not the main source for discontinuous cracks on single crystalline hexagonal graphene domains. Most likely ductile cracking during the cooling stage of CVD can be a reason for the discontinuous cracks and vacancy defects in hexagonal graphene domains.

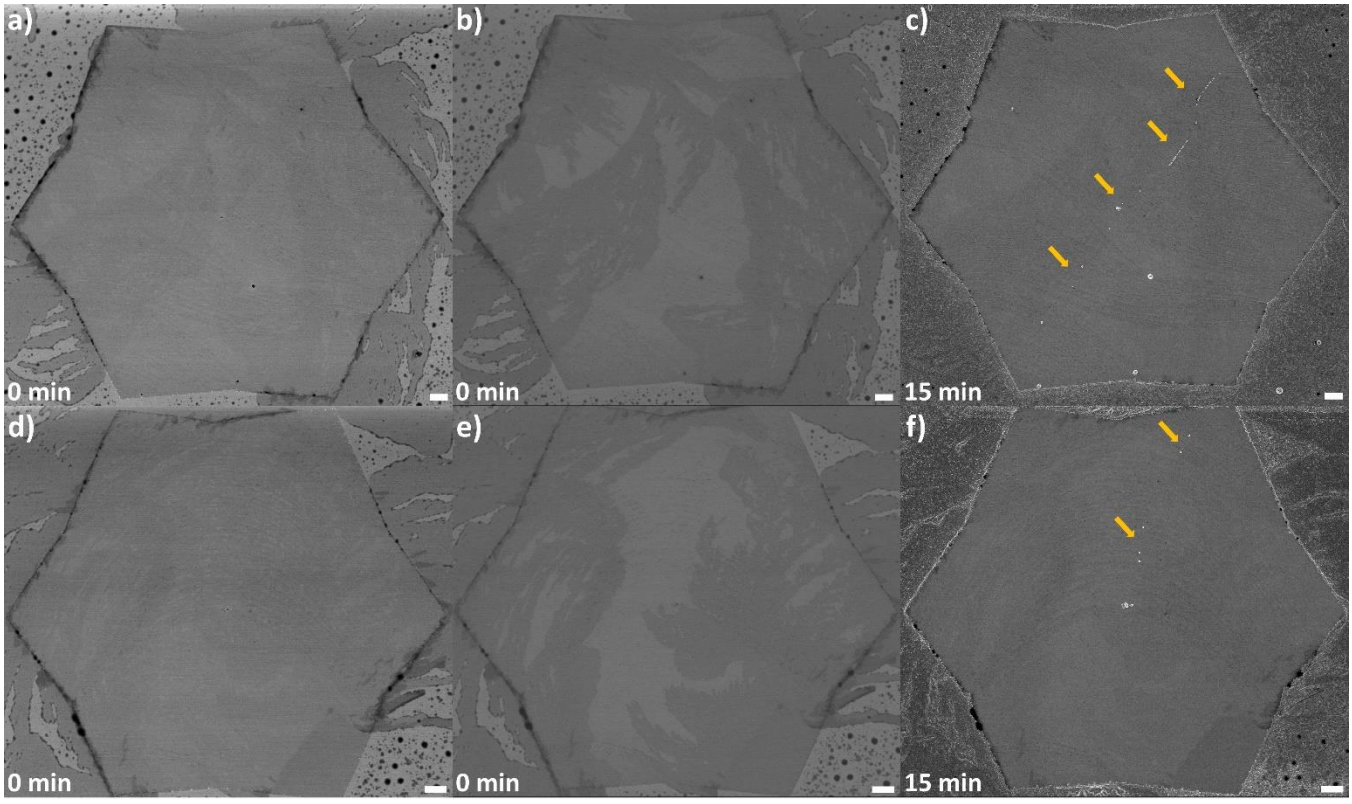

Figure 3.9. SEM and SEM-BSE images hexagonal graphene domains on copper before H_2S treatment and SEM images after 15 minutes of H_2S gas treatment. **(a,d)** SEM images of hexagonal graphene domains on copper before H_2S treatment. **(b,e)** SEM-BSE images of the same regions in (a,d). There is no wrinkle observed. **(c,f)** SEM images of the same region in **(a-e)** after 15 minutes of H_2S treatment. There are particles formed on discontinuous defects which is indicated by orange arrows. Scale bar: 1 µm.

3.3.2.3 The wrinkle and isolated discontinuous cracks in the hexagonal graphene domains

In some of the hexagonal monolayer single crystalline graphene domains, it is seen that discontinuous cracks exist as independent from wrinkles. Figure 3.10 shows examples of this kind of domains where discontinuous cracks are observed away from wrinkles. This shows that wrinkles are not the main resource for discontinuous cracks on single crystalline hexagonal graphene domains. Therefore, complex mechanical stresses that graphene experience during

the CVD process due to substrate effects may be the reason for the observed discontinuous defects.

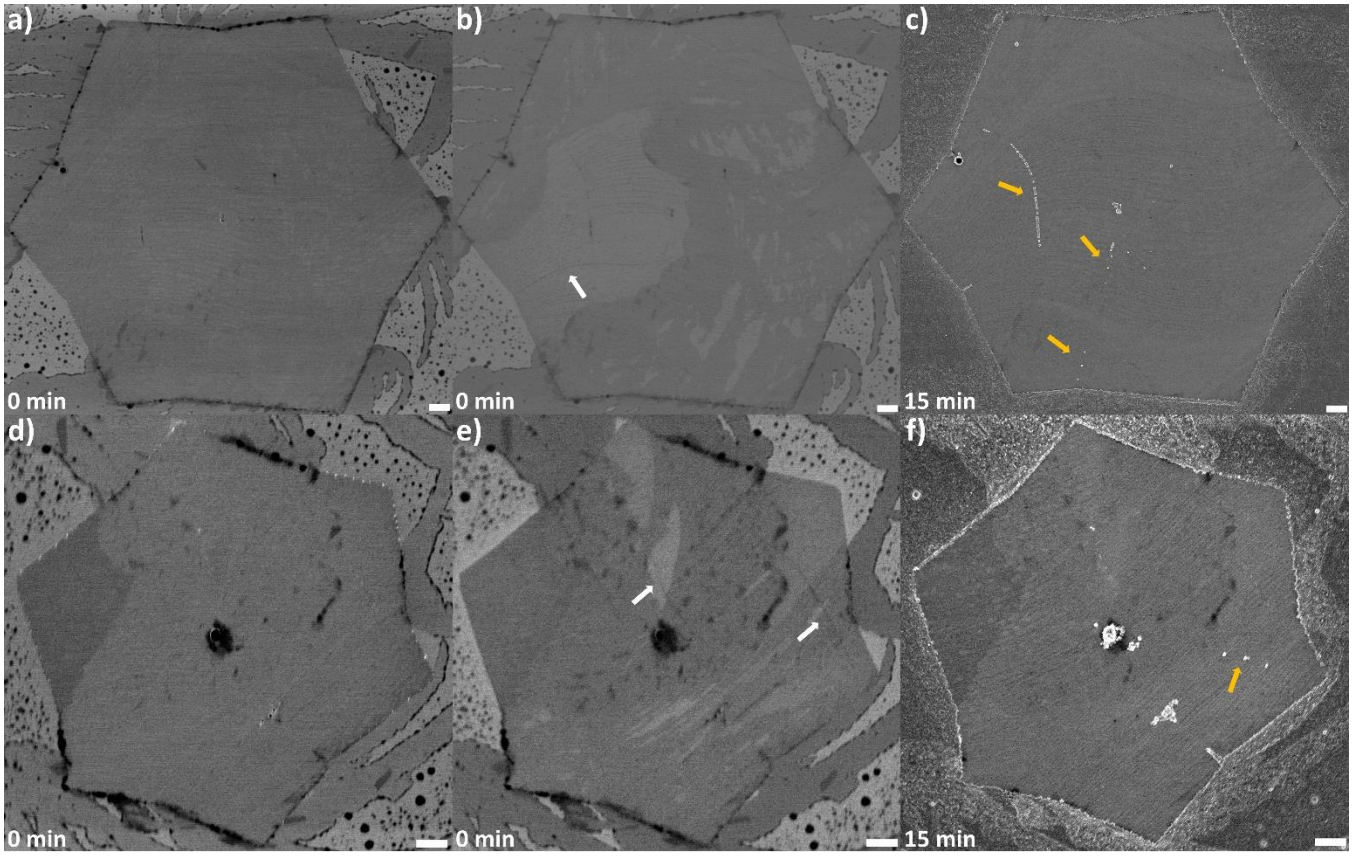

Figure 3.10. SEM and SEM-BSE images of hexagonal graphene domains on copper before H_2S treatment and SEM image after 15 minutes of H_2S treatment. **(a,d)** SEM images of hexagonal graphene domains on copper before H_2S treatment. The wrinkles are not visible. **(b,e)** SEM-BSE images of the same graphene domains in **(a,d)**. The white arrows indicate graphene wrinkles. **(c,f)** SEM images of the same graphene domains in **(a,d)** after 15 minutes of H_2S treatment. There is no particle formation on wrinkles but on the other regions which is indicated by blue arrows. Scale bar: 1 µm.

3.4. Conclusion

We have studied and clarified potential effects of graphene wrinkles on the formation of vacancy defects in polycrystalline graphene and single crystalline graphene, respectively. We have found that although the graphene wrinkles are the main source for vacancy defects in the

polycrystalline CVD-grown graphene samples, there are other possible sources such as mechanical stress that are responsible for the formation of vacancy defects in polycrystalline graphene where wrinkles are not found (e.g. Figure 2.20). In contrast, we have found that graphene wrinkles are NOT mainly responsible for the observed vacancy defects in single crystalline hexagonal graphene domains. Our study in this chapter lends further indirect support to our previous findings in chapter 2, that is, the copper grain and copper grain boundary play significant roles in formation and distribution of graphene vacancy defects, and the observed discontinuous cracks more likely originate from a ductile fracture of graphene.

3.5 References

(1) Zhang, B.; Xiao, H.; Yang, G.; Liu, X., *Eng. Fract. Mech.,* **2015***, 141*, 111-119.

(2) Benzerga, A. A.; Leblond, J., *Adv. Appl. Mech*., **2010***, 44*, 169-305.

(3) Deng, B.; Wu, J.; Zhang, S.; Qi, Y.; Zheng, L.; Yang, H.; Tang, J.; Tong, L.; Zhang, J.; Liu, Z.; Peng, H., *Small*, **2018***, 14*, 1800725.

(4) Wang, Z.; Weinberg, G.; Zhang, Q.; Lunkenbein, T.; Klein-Hoffmann, A.; Kurnatowska, M.; Plodinec, M.; Li, Q.; Chi, L.; Schloegl, R.; Willinger, M., *ACS Nano*, **2015***, 9*, 1506-1519.

(5) Zhang, Y.; Zhang, H.; Chen, Z.; Ge, X.; Liang, Y.; Hu, S.; Deng, R.; Sui, Y.; Yu, G., *J. Appl. Phys*, **2017***, 121*, 245306.

(6) Wood, J. D.; Schmucker, S. W.; Lyons, A. S.; Pop, E.; Lyding, J. W., *Nano Lett.,* **2011***, 11*, 4547-4554.

(7) Deng, B.; Pang, Z.; Chen, S.; Li, X.; Meng, C.; Li, J.; Liu, M.; Wu, J.; Qi, Y.; Dang, W.; Yang, H.; Zhang, Y.; Zhang, J.; Kang, N.; Xu, H.; Fu, Q.; Qiu, X.; Gao, P.; Wei, Y.; Liu, Z.; Peng, H., *ACS Nano*, **2017***, 11*, 12337-12345.

(8) Tian, J.; Cao, H.; Wu, W.; Yu, Q.; Chen, Y. P., *Nano Lett.,* **2011***, 11*, 3663-3668.

(9) Ozbal, G.; Falkenberg, J. T.; Brandbyge, M.; Senger, R. T.; Sevincli, H., *Phys. Rev. Mater*., **2018,** 2, 073406.

(10) Srivastava, D.; Brenner, D. W.; Schall, J. D.; Ausman, K. D.; Yu, M.; Ruoff, R. S., *J. Phys. Chem. B*, **1999***, 103*, 4330-4337.

(11) Park, S.; Srivastava, D.; Cho, K., *Nano Lett.,* **2003***, 3*, 1273-1277.

(12) Bissett, M.A.; Tsuji, M.; Ago, H., *Phys. Chem. Chem. Phys., **2014**, 16,* 11124-11138.

(13) Rasmussen, J. T.; Gunst, T.; Bøggild, P.; Jauho, A.; Brandbyge, M., *Beilstein J Nanotechnol*, **2013***, 4*, 103-110.

(14) Deng, S.; Berry, V., *Mater. Today*, **2016***, 19*, 197-212

(15) Pacakova, B.; Verhagen, T.; Bousa, M.; Hübner, U.; Vejpravova, J.; Kalbac, M.; Frank, O., *Sci. Rep*., **2017***, 7*, 10003-11

(16) Long, F.; Yasaei, P.; Sanoj, R.; Yao, W.; Král, P.; Salehi-Khojin, A.; Shahbazian-Yassar, R., *ACS Appl Mater Interfaces*, **2016***, 8*, 18360-18366.

(17) Kwak, J.; Jo, Y.; Park, S.; Kim, N. Y.; Kim, S.; Shin, H.; Lee, Z.; Kim, S. Y.; Kwon, S., *Nat. Commun*., **2017***, 8*, 1549.

(18) Tzolov, M. B.; Barbi, N. C.; Bowser, C. T.; Healy, O*., Microsc. Microanal*., **2018***, 24*, 488-496.

(19) Kwak, J.; Kim, S.; Jo, Y.; Kim, N. Y.; Kim, S. Y.; Lee, Z.; Kwon, S., *Adv. Mater*., **2018***, 30*, 1800022.

Chapter 4: *In Situ* Chemical Probing of Defects in Hexagonal Boron Nitride (h-BN) at Room Temperature

4.1. Introduction

The family of two-dimensional materials beyond graphene such as transition metal dichalcogenides (TMDCs), hexagonal boron nitride (h-BN) offers greater choices of desired properties for various applications. The appealing properties of these materials can complement or surpass graphene in many applications in electronics, optoelectronics and energy storage.[1]

Similar to carbon, boron nitride commonly exists in hexagonal (h-BN) and cubic forms (c-BN). While h-BN features sp^2 hybridized atomic orbitals, c-BN atoms adopt the sp^3 hybridization configuration.[2] h-BN, a structural analogue of graphene, is a single atomic layer of alternating boron and nitrogen atoms in hexagonal lattice structure. h-BN is referred as "white graphene" due to its structural similarity to graphene.[3] While graphene is zero band-gap and semi-metal, monolayer h-BN is an insulator material with the optical band gap of about 6 eV.[2-4] Monolayer h-BN exhibits higher transparency than graphene in the visible region.[4] In h-BN each B and N atom possesses sp^2 hybrid orbitals through hybridization of the 2s orbital with two of the 2p orbitals. Three sp^2 orbitals of each B atoms are bonded three sp^2 orbitals of each N atoms with strong in-plane σ bonds, rendering h-BN with high mechanical strength, excellent chemical inertness and high thermal conductivity.[5] h-BN has good oxidation resistance up to 1000 °C, higher than as of graphene, which makes it attractive as high-temperature oxidation resistant coating material.[6] It also has a very high thermal conductivity (2000 W/m K), which makes it an ideal heat spreader and thermal interface material.[7] The thermal expansion

coefficient of monolayer h-BN is -3.41 x 10^{-2} cm^{-1} K^{-1}.[3] The planar hexagonal lattice structure with a small mismatch with graphene (only 1.7%), atomically smooth surface and large band-gap makes h-BN a promising candidate as a dielectric layer or a protecting encapsulator for two-dimensional electronic devices.[3] To illustrate, an ultrahigh carrier mobility (60 000 cm^2 V^{-1} s^{-1} at room temperature) was exhibited in graphene transistors when h-BN employed as a substrate instead of SiO_2.[8-9] The ultraflat surface of h-BN without dangling bonds even makes it a candidate substrate for the growth of other two-dimensional nanomaterials such as graphene, WS_2, MoS_2 and others .[8,10]

4.1.1. Chemical Vapor Deposition (CVD) h-BN

Monolayer h-BN flakes can be obtained by exfoliation from bulk single crystalline h-BN similar to mechanical exfoliation of graphene from graphite.[11] Whereas this method gives tiny pieces of h-BN through laborious mechanical exfoliation and transferring process which is valuable for fundamental research, a scalable way of production is required for both scientific and commercial purposes.[12] In addition, it is hard to prepare single layer h-BN by mechanical exfoliation due to greater electrostatic attractions between B and N atoms in neighboring layers. The ionic characteristic of B-N bond may cause formation of interlayer B-N bonds acting as welding spot between layers.[10] This makes mechanical exfoliation of h-BN more challenging than mechanical exfoliation of graphene.

Besides mechanical exfoliation some other methods have been developed to obtain h-BN such as liquid phase exfoliation, unzipping BN nanotube, molecular beam epitaxy (MBE) and chemical vapor deposition (CVD).[13] Among them CVD seems to be the most facile and scalable way to produce large-area and high-quality monolayer h-BN film. CVD is a versatile

method in terms of feedstock, chamber pressure, carrier gas and the substrate that the thin film would grow onto.[3]

Monolayer h-BN production on single crystal substrates and in ultrahigh-vacuum (UHV) by CVD was reported since 1990s.[14] The high cost of single crystalline substrate and UHV chamber for the production rendered this method impractical for large scale production of monolayer h-BN. CVD synthesis of monolayer graphene on cheap substrates was soon followed by the synthesis of monolayer h-BN as a feasible way of production.[1,7,15-18] Moreover, a great deal of progress has been made by catalyst surface treatment, tuning of precursors, temperature and pressure of CVD system.[7,19-20] Similar to the graphene synthesis, polycrystalline copper and nickel foils have been widely used as a substrate for h-BN synthesis due to their large availability, low-cost and allowing transfer of the synthesized films with the ease of etching.[21] On the other hand, h-BN has been produced on various transition metal surfaces, such as Pt, Co, Ag, Fe, Ir, Rh and Ru.[13,21] Gaseous precursors such as BF_3/NH_3, BCl_3/NH_3, and B_2H_6/NH_3 ; liquid precursors such as borazine ($B_3N_3H_6$), trichloroborazine ($B_3N_3H_3Cl_3$), and hexachloroborazine ($B_3N_3Cl_6$); and solid precursors such as ammonia borane (H_3BNH_3), which is also called as borazane, have been used as precursors for h-BN synthesis in CVD. Borazane has clear advantages over other precursors because of 1/1 B:N stoichiometry and being solid and stable under ambient conditions.[22] In terms of pressure of the growth chamber, both atmospheric pressure CVD (APCVD) and low-pressure CVD (LPCVD) have also been used to produce h-BN on metals. All of the aforementioned variables as well as growth temperature and duration affect the domain size and shape as well as uniformity and thickness of the produced film in CVD growth of h-BN.[22]

4.1.2. Defects in Chemical Vapor Deposition (CVD) h-BN

Similar to graphene production in CVD, imperfections and grain boundaries on polycrystalline copper surface are preferred locations for the nucleation of h-BN domains. This consequently affects the quality of the final product. Moreover, pre-growth surface treatments on the substrate and melting the top layers of the substrate can help eliminate surface imperfections and improve overall quality of the produced h-BN film.[2] Various h-BN domain shapes were observed including triangle, asymmetric diamond and hexagon due to the difference in the growth parameters such as pressure of the CVD chamber, growth time, temperature of the precursor and the location of the substrate inside the growth chamber.[22-23] Moreover, the shape of the formed domains affected by the ratio of B/N species on the copper surface inside the CVD chamber. When N containing species are in high concentration, nitrogen ended triangles and; when B containing species are in high concentration, truncated triangles and hexagonal domains with B and N terminated edges have been observed.[3]

In a typical CVD growth of h-BN, nucleation occurs in many locations on polycrystalline copper surface simultaneously. Unlike graphene, h-BN consist of 2 different elements, B and N, therefore there is a greater variation of the edge termination. This variation makes it more complicated for stitching of individual domains to form monolayer continuous h-BN. Moreover, nitrogen termination is generally considered energetically more favorable, compared to Boron termination (Figure 4.1).[8]

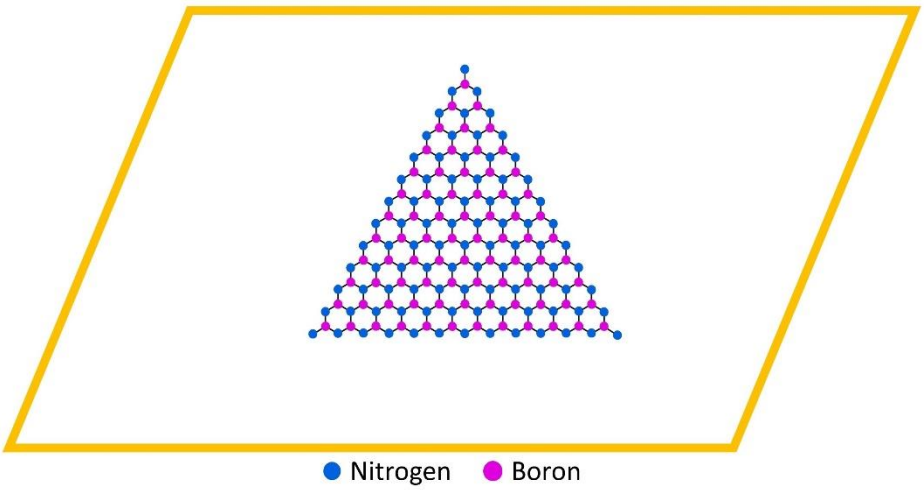

Figure 4.1. Illustration of atom arrangement of monolayer triangular h-BN domain.

In a general CVD production of h-BN, the nucleation takes place in an uncontrolled fashion. Due to nucleation on many spots with a small domain size, orientation angle of each individual domain and domain edge atoms play an important role for coalescing seamlessly and form a continuous single layer. It is known that the average domain size of CVD-grown h-BN (several micrometers) on copper in a normal growing procedure is much smaller compared to the graphene domain size (which can exceed 1 cm).[22] The orientation of individual h-BN domains is generally same on the same copper domain that they grow on.[24] Different copper domains yield different preferred h-BN orientations, which indicates the epitaxial relationship between h-BN and copper film.[13] Depending on the domain shape, orientation angle and edge atoms of the individual domains, seamless merging, merging with a grain boundary or not merging, by creating a defect line, seems to be possible to occur.[13]

Large-area CVD-grown monolayer h-BN is typically polycrystalline and therefore contains grain boundaries. Figure 4.2 shows the illustration of possible merging situations for individual triangular h-BN domains that have various orientations.

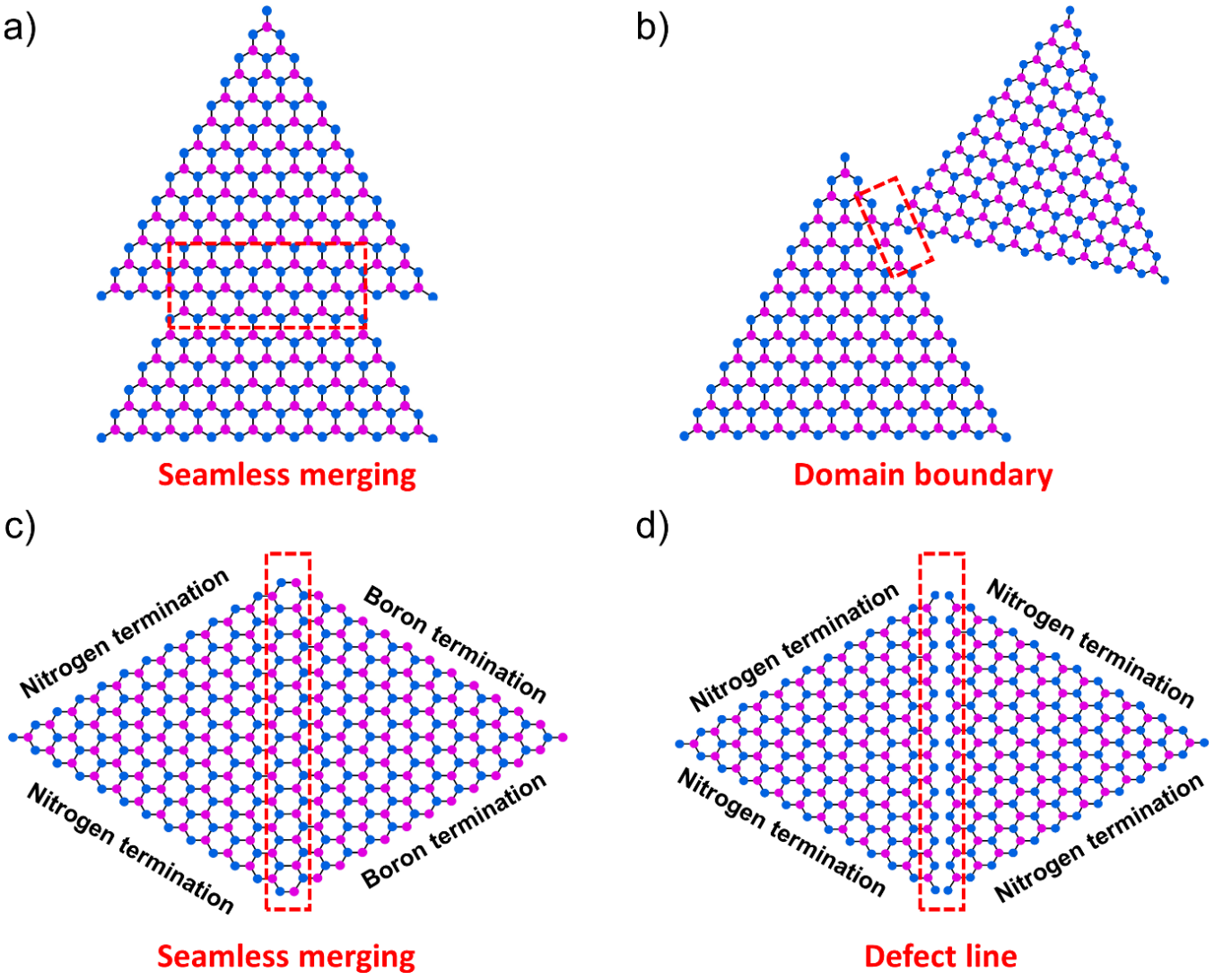

Figure 4.2. Schematic illustration of the atomic configuration for merging between triangular h-BN domains that have different orientations.

It is very important to produce large area uniform h-BN for practical applications.[8] In this regard, another common issue for the production of monolayer h-BN via CVD is the existence of ubiquitous adlayers. These are layers of triangular h-BN regions on monolayer continuous h-BN film.[25] The h-BN multilayers often resemble pyramid like structure.[26] The number of

adlayers can be various and be noticeable on SEM images depending on the imaging conditions (Figure 4.3).[27]

Similar to graphene, h-BN also has a negative thermal expansion coefficient value that causes formation of wrinkles during cooling stage of CVD.[28] These wrinkles of CVD-grown monolayer h-BN are seen as a characteristic feature of monolayer h-BN films. [25]

4.1.3. Characterization of CVD-grown monolayer h-BN

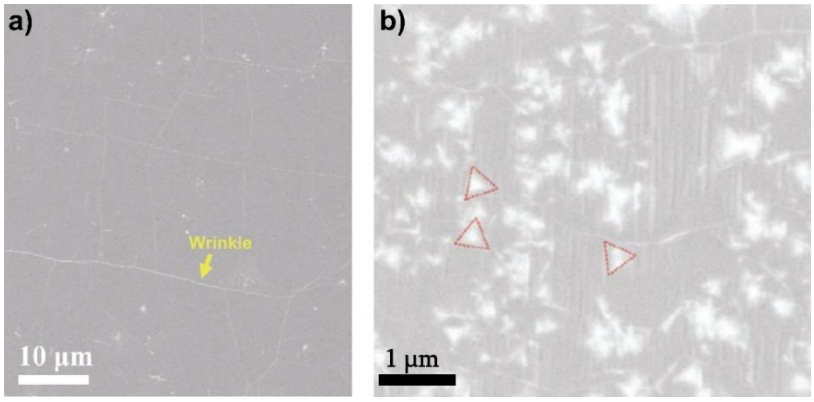

Figure 4.3. SEM images of CVD grown h-BN on copper foil. **(a)** Low-magnification SEM image of a continuous monolayer h-BN. The yellow arrow indicates one of the h-BN wrinkles. **(b)** Higher magnification image, showing triangular multilayer pyramidal h-BN islands (some of which indicated with red triangles) on monolayer h-BN.[25]

Similar to graphene characterization, SEM, TEM, STM and Raman Spectroscopy is used in the literature to characterize produced monolayer h-BN samples. The wrinkles, multilayers and nanoparticles can be seen on SEM images of h-BN on copper foil after the growth without any transfer (Figure 4.3).[25] High-resolution transmission electron microscopy (HRTEM) and STM imaging give information about monolayer h-BN in atomic scale. The crystallinity, grain boundaries and structural defects can be surveyed by these techniques. However, these techniques require transfer of the produced monolayer h-BN from the growth substrate and only

allows to investigate a very small area at once.[29] Also, STM investigation of h-BN is particularly challenging due to inhomogeneity of layer thickness, roughness of the growth substrate and insulator character of h-BN film.[30] Raman spectroscopy is used to confirm the existence of h-BN as well as to examine its quality. The characteristic peak at about 1366 cm^{-1} corresponds to vibrations between B and N moving against each other in the same plane. The width, intensity and position of these Raman signal is sensitive to h-BN thickness. Raman spectroscopy of h-BN requires transfer of the film. Though Raman signal of h-BN is very weak for monolayer but increase with the increase of the number of layers.[30] X-ray photoelectron spectroscopy (XPS) measurements are used to identify the elemental composition and bonding information in h-BN.[27] Atomic force microscopy (AFM) can be used to measure the thickness, therefore allows to check uniformity of the produced sample. However, it requires transfer of the sample onto a flat surface such as silicon wafer. UV−vis absorption spectroscopy of monolayer h-BN films is used to calculate the bandgap and compare with the usual bandgap, about 6 eV, of monolayer h-BN film in order to investigate the quality.[27] These aforementioned techniques often require transfer of the produced film from the original substrate to a flat substrate or a grid. Like it is in the case of graphene, transfer process leads to undesired artefacts, such as residues, wrinkles and/or cracks.[27] In addition, requiring transfer and being able to examine a very small area in the micrometer-scale makes it very time consuming to survey a usual CVD-grown sample entirely which is often in inch-scale. Therefore, a technique that allows one to investigate a relatively large area without requiring transfer is needed for the quality control of the produced monolayer h-BN films in commercial and research purposes.

In the literature, it is seen that the methods specifically developed to identify GBs on h-BN are rare.[31-32] One of the GB detection methods in large area is based on high temperature

hydrogen etching at the GB regions.[32] To the best of our knowledge, there is no experimental method in the literature suggested for the identification of vacancy defects in produced monolayer CVD-grown h-BN practically in large scale. Compared with vacancy defects in graphene, vacancy defects in h-BN are much less characterized and understood. The practical investigation of individual nanoscale vacancy defects in h-BN still remains as a challenge.[31,33] Hence, it is important to develop a method for rapidly identification of the vacancy defects in large area monolayer h-BN. Such a method would be either useful for the quality control of the produced material or provide useful information on defects for improving synthesis procedures. Therefore, our defect identification method developed for graphene (in Chapter 2) can be used for the identification of vacancy defects in large area h-BN.

4.2. Experimental

4.2.1. Materials

The CVD-grown monolayer h-BN samples on copper foil were purchased from Grolltex Inc. and Graphene Laboratories Inc. Sodium sulfide nonahydrate ($Na_2S.9H_2O$) and sulfuric acid (H_2SO_4) (6.00 N) were purchased from MP Biomedicals and Ricca Chemical Company, respectively.

4.2.2. Characterization

SEM imaging and EDX analysis were performed using a Hitachi S-4800 field emission scanning electron microscope equipped with an EDX spectrometer under high vacuum ($<10^{-3}$ Pa). An emission current of 10 μA and accelerating voltage of 1, 2 and 3.5 keV with a working distance of about 3, 8 and 15 mm were used for SEM. EDX experiments were performed by

using emission current of 10 μA and accelerating voltage of 3.5 keV with a working distance of about 15 mm.

4.2.3. H_2S treatment of h-BN on copper foil

In a typical experimental procedure, a piece of h-BN on copper was cut for initial SEM imaging (0 min) (Figure 4.4a, b). After SEM imaging, the sample was placed in a 4 mL glass vial (Figure 4.4c). Then the 4 mL vial with h-BN sample in it was placed inside a vial with a larger diameter. The 20 mL vial was charged with 30 mg $Na_2S.9H_2O$ (Figure 4.4d). After that, the 20 mL vial was sealed using a matching screw cap with PTFE/silicone septum. Finally, 0.5 mL of 0.5 M H_2SO_4 solution was quickly injected into the 20 mL vial via a syringe through the septum. Then the reaction setup was immediately placed in dark during the reaction. After certain amount of time (e.g. 2 min), the reaction was stopped by opening the vial and removing the graphene sample. Subsequently, the H_2S-treated h-BN sample was placed under vacuum in dark for about 24 hours, in order to remove any potential residual H_2S gas that may be adsorbed on the surface. Later, the chemically treated h-BN sample was imaged by SEM for the second time at the same spots as the first SEM imaging (Figure 4.4e). All the H_2S treatment experiments were performed at room temperature in the fume hood.

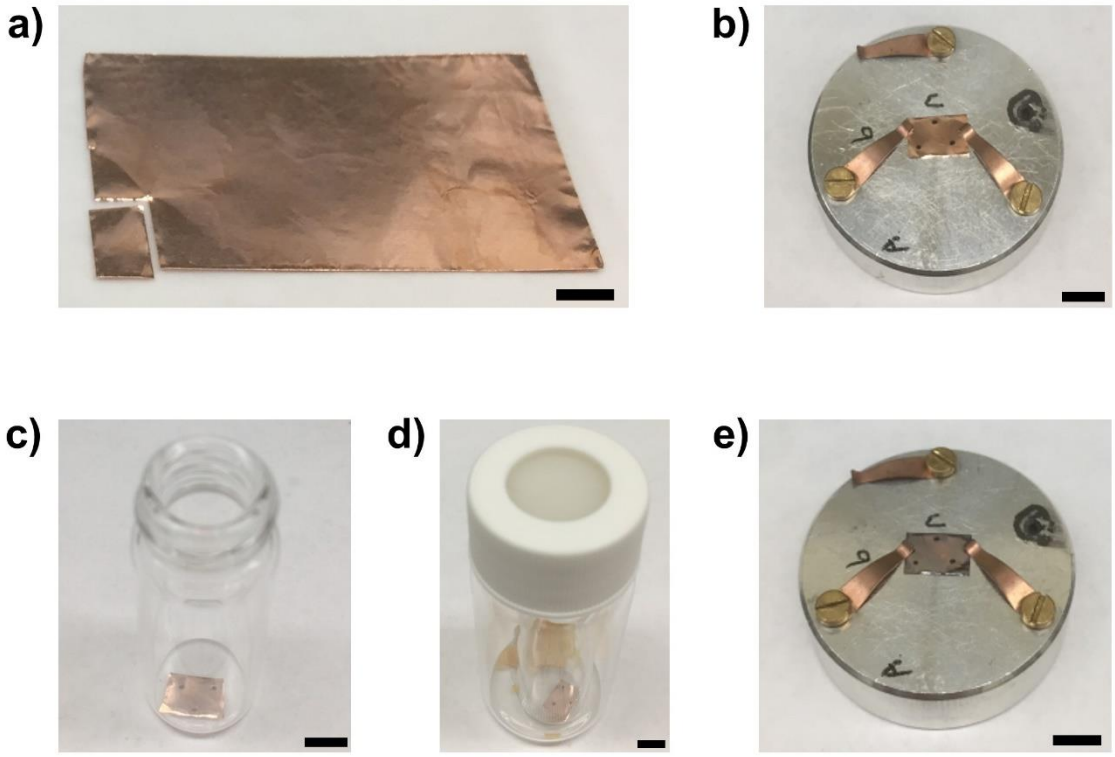

Figure 4.4. Photo pictures of the experimental steps for H_2S treatment for h-BN on copper. **(a)** A piece of h-BN on copper is cut from commercially bought h-BN on copper foil. **(b)** h-BN on copper foil is placed on an SEM stub and held in place with the screw holders for initial SEM imaging. **(c)** After initial SEM, the piece is placed in a 4 mL vial. **(d)** 4 mL vial with the h-BN on copper piece is placed in a 20 mL vial. The 20 mL vial is charged with reagents for the treatment. **(e)** After the treatment and 24 hours vacuum, h-BN on copper piece is placed on the SEM stub for a second imaging after the treatment. Scale bar: 0.5 cm.

4.3. Results and Discussion

4.3.1 Characterization of CVD-grown h-BN samples

Commercially available CVD-grown monolayer h-BN samples from Grolltex Inc. and Graphene Laboratories Inc. were used in all experiments. A typical sample comprises mainly nearly continuous polycrystalline monolayer h-BN on 25 μm-thick copper foil, with numerous triangular adlayer and multilayer pyramidal h-BN islands on it (Figure 4.5a). Also, thin white

lines indicate the existence of wrinkles. These wrinkles are indicative of h-BN films and are postulated to be caused by differences in thermal expansion between Cu and h-BN.[25]

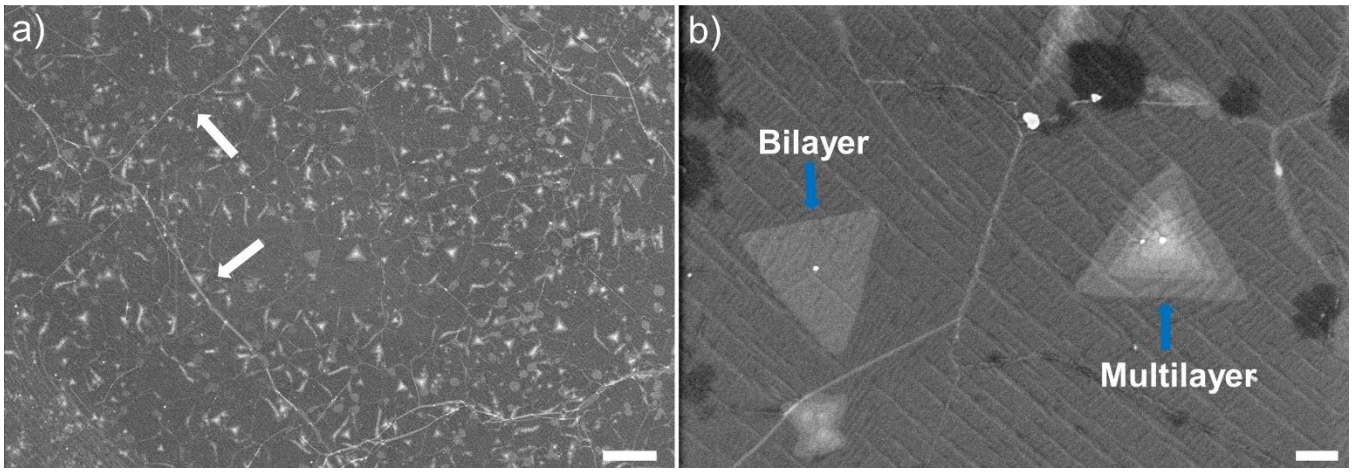

Figure 4.5. SEM images of CVD grown h-BN on copper foil. **(a)** Low-magnification image, showing excessive multilayers of h-BN in monolayer h-BN. The white arrows show the wrinkles on h-BN. **(b)** High-magnification image in the same region, showing triangular adlayer and multilayer pyramidal h-BN island on monolayer h-BN. Scale bar: **(a)** 2 μm and **(b)** 0.2 μm.

Energy-dispersive X-ray spectroscopy (EDX) analysis can be used to track layer thickness of h-BN on copper sample. It is challenging to observe and quantify light elements such as Boron in EDX experiments because of inherent physical problems such as low fluorescence yield, absorption and peak overlaps with heavier elements. Due to their low energies, many of the few X-rays produced by Boron may not be able to leave the sample because they may be absorbed before reaching the sample surface. Nevertheless, in our study, adequate signals provided by Nitrogen in EDX experiments. EDX analysis results are presented in (Figure 4.6). The SEM image shows the points that EDX analyses were performed on. (a-i) A thicker spot, close to the center of multilayer area; (a-ii) less thick region on multilayer area, close to the edge of the triangular region; and (a-iii) outside of the multilayer area on monolayer h-BN. EDX spectra of the spots i, ii and iii in (a) have nitrogen atomic percentage of 11.4, 3.0

and 1.2 respectively (figure 4.6e). Therefore, it can be said that brighter regions on monolayer h-BN have adlayers of h-BN. While the bright triangular regions are thicker in the middle, they are thinner closer to the edges; reminding a pyramidal structure of multilayers.

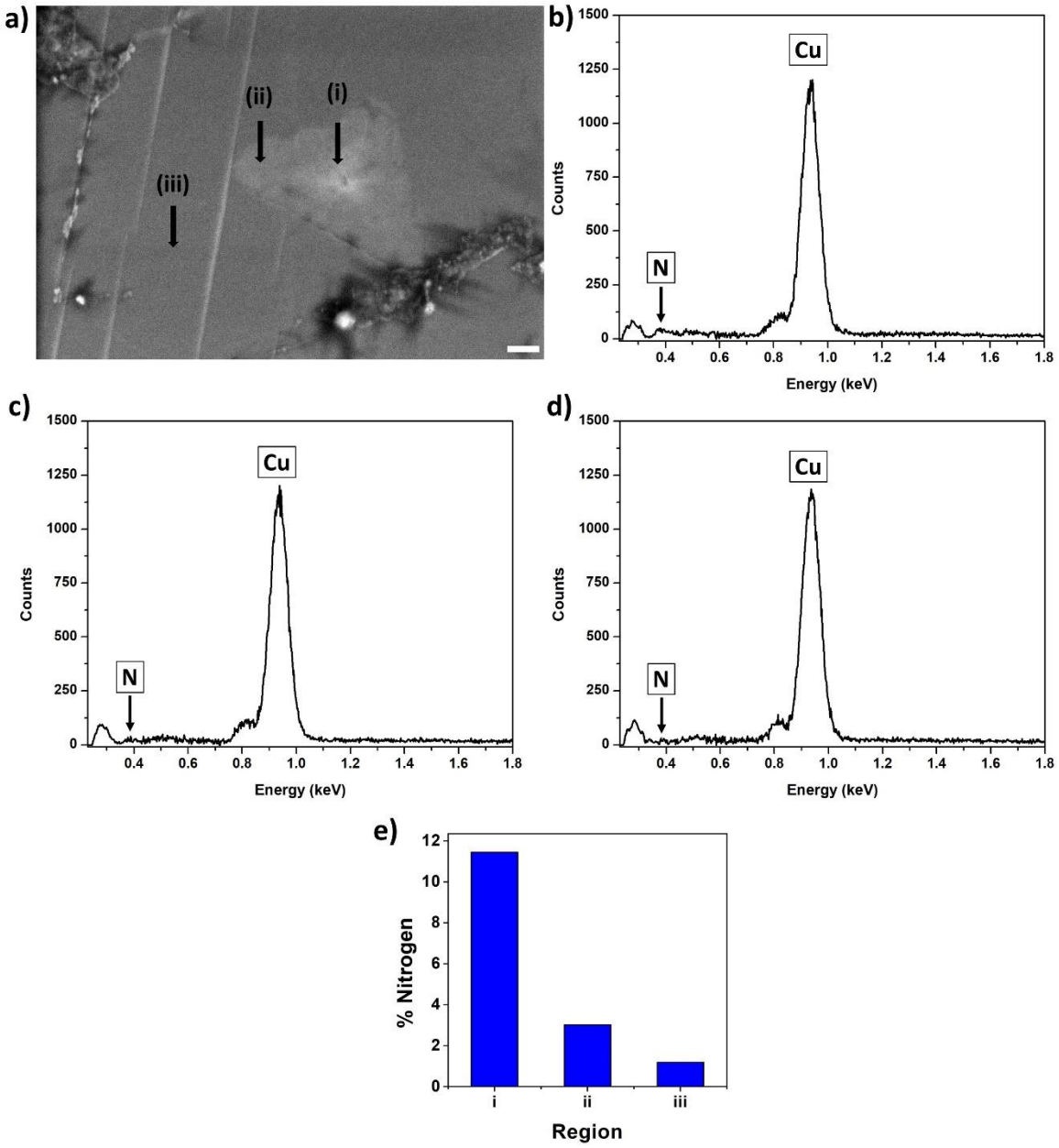

Figure 4.6. EDX spectra of pristine h-BN on copper. **(a)** SEM image of monolayer h-BN on copper with a triangular multilayer region. The scale bar: 0.2 μm. **(b,c,d)** EDX spectra of spots indicated as **(i)**, **(ii)** and **(iii)** in **(a)** in order, respectively. **(e)** Bar graph for atomic percentage of nitrogen in regions i, ii and iii in **(a)**.

An EDX analysis was performed on h-BN on copper foil after 2 minutes of H_2S gas treatment is applied. SEM image of the h-BN on copper foil after the treatment is shown in Figure 4.7a. The SEM image shows the points that EDX analysis was performed on. i) a monolayer h-BN region, ii) a particle formed around a multilayer h-BN region iii) inside of the multilayer area on h-BN.

a)

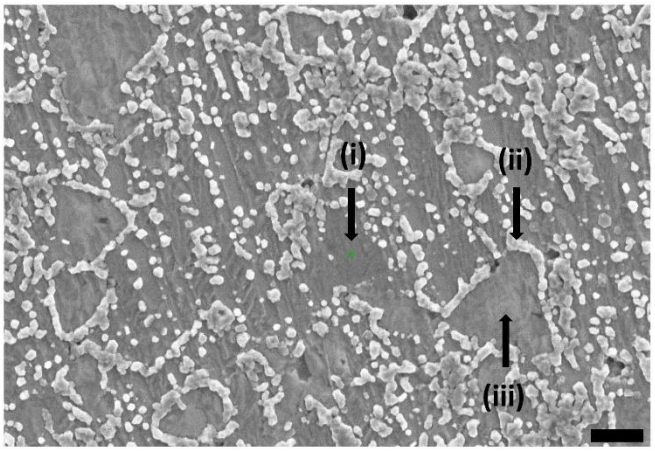

b)

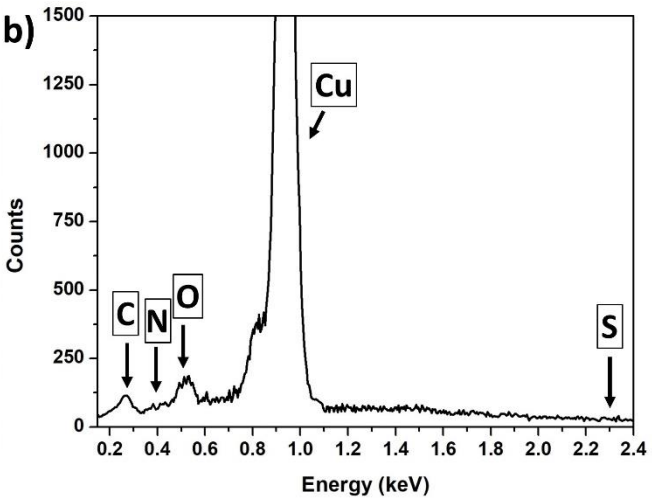

c)

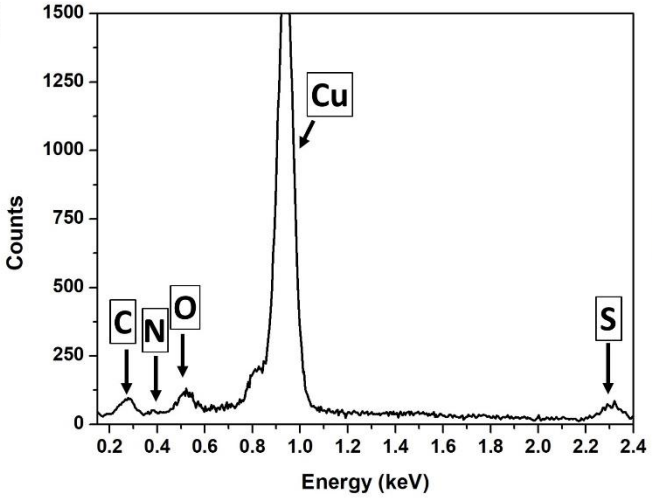

d)

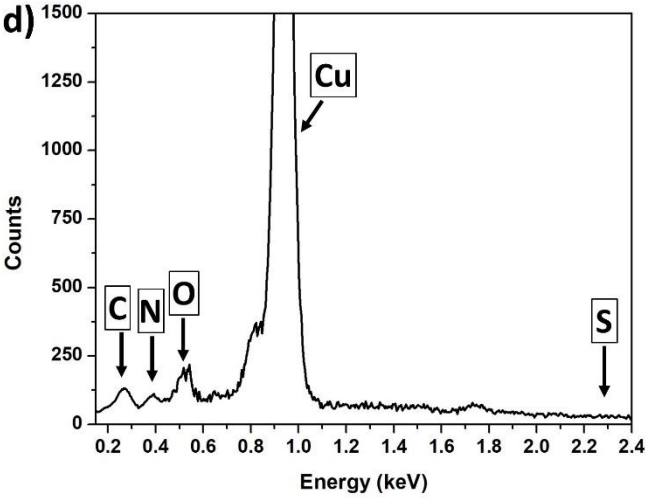

e)

	(i)	(ii)	(iii)
Element	Atomic %		
N	4.1	3.1	10.7
O	6.3	5.9	6.9
Cu	82.2	61.3	72.8
S	2.0	19.5	1.2

f)

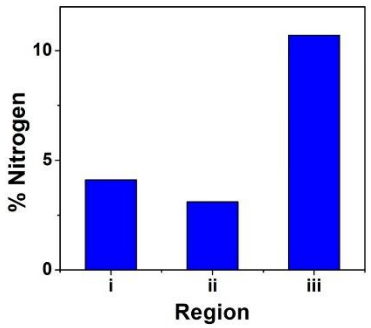

Figure 4.7. EDX spectra of h-BN on copper after H_2S gas treatment for 2 minutes. **(a)** SEM image of monolayer h-BN on copper with newly formed particles. The scale bar: 0.5 μm. **(b,c,d)** EDX spectra of spots indicated as **(i)**, **(ii)** and **(iii)** in **(a)** in order, respectively. **(e)** Table showing the elemental composition of the analyzed spots in (a) by atomic percentage. **(f)** Bar graph for atomic percentage of nitrogen in regions i, ii and iii in (a).

As it can be seen in the table in Figure 4.7e, the particle formed on h-BN on copper with H_2S gas treatment, mainly consist of Cu (61.3%) and S (19.5%) elements. Atomic percentage of nitrogen is higher in triangular multilayer region compared to monolayer region of h-BN (Figure 4.7f).

4.3.2. Chemical probing of vacancy defects in polycrystalline h-BN films

Herein, we report a new method for *in situ* chemical probing of vacancy defects in CVD-grown h-BN. Our approach is based on a solid-gas phase reaction that occurs selectively in h-BN vacancy defect regions such as holes and cracks, where the underlying metal catalyst substrate such as copper is exposed to the air and oxidized at room temperature. Owing to its small molecular size, which is roughly comparable with O_2, H_2S can penetrate through nanoscale h-BN vacancy defects. The reaction between the exposed oxidized copper substrate and H_2S gas at room temperature leads to the formation of Cu_xS nanoparticles, which can be readily imaged by SEM.[34] SEM is relatively easily accessible and common instrument in nanotechnology laboratories which can allow investigation of inch-wide samples. Thus, our method with such a short application time allow producers to routinely check the quality of the produced sample in a short period of time.

Figure 4.8 shows SEM images of monolayer h-BN before and after H_2S gas treatment. The H_2S gas treatment time is noted in each image. The bright triangular regions (some of which are indicated with white arrows in Figure 4.8a, c, e) are known in the literature as

multilayers of h-BN. It can be seen that no particles formed on multilayer regions after H_2S gas treatment (Figure 4.8b, d, f). The copper underneath is well protected, meaning not exposed to the air or H_2S gas on the multilayer triangular regions. In addition, no particles formed on irregular shaped bright regions too (some of which are indicated with blue arrows in Figure 4.8a, c, d). This suggests that irregular and relatively thick lines in SEM images indicate multilayer areas, similar to triangular regions. This is a new finding related to the characterization of monolayer CVD-grown h-BN, suggesting that not only triangular regions but also irregular shaped thick bright lines are indicative of multilayer regions. On the other hand, dark and corrugated looking areas in the SEM images are where the vacancy defects are commonly observed after the treatment. The dark areas are not completely defective but are defect-dense areas.

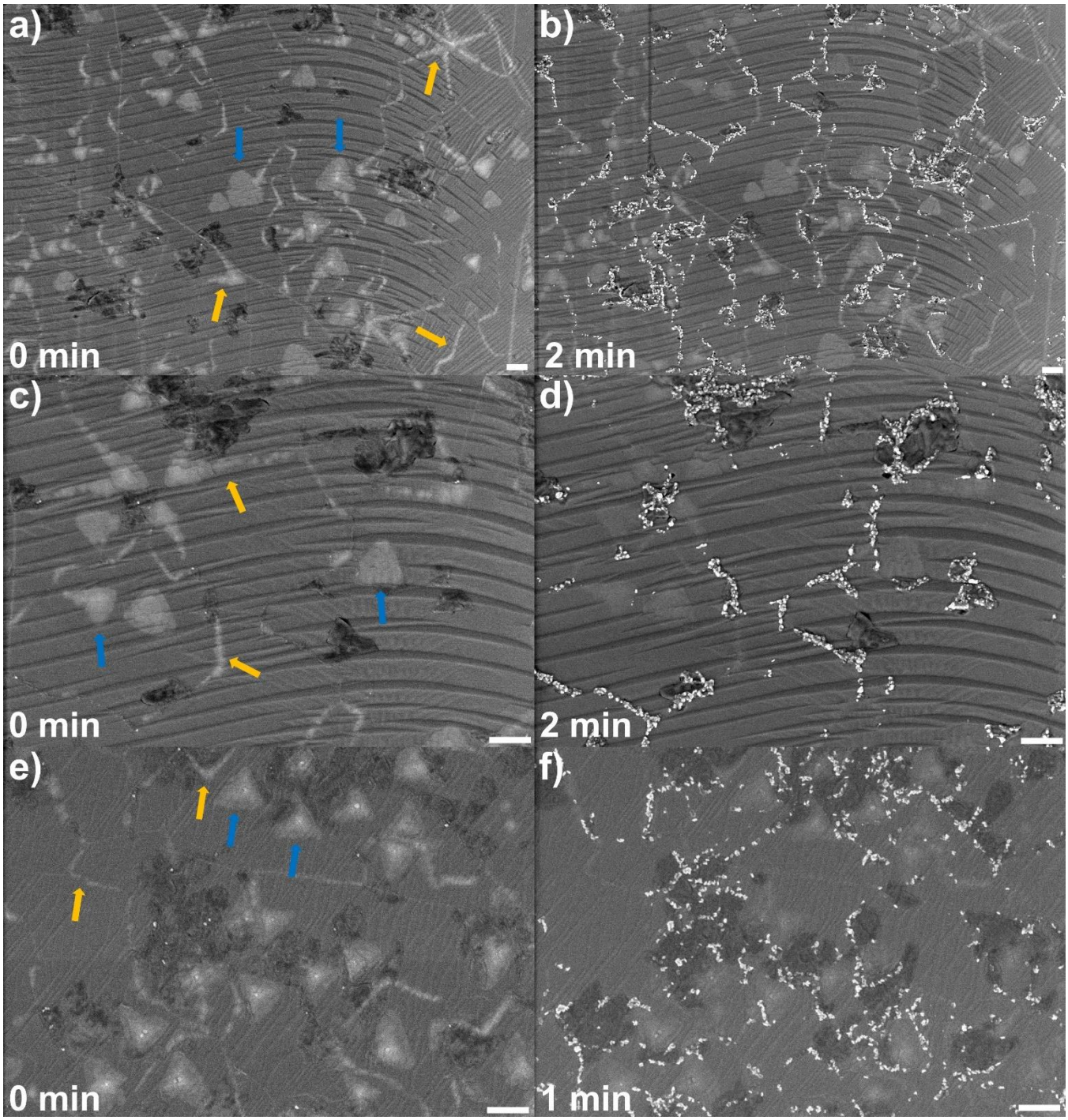

Figure 4.8. SEM images of monolayer h-BN on copper foil before and after H_2S gas treatment. **(a,b)** SEM images of the same region before and after 2 min treatment. **(c,d)** The higher magnification images of the upper-middle region in **(a)**. **(e,f)** SEM images of another region before and after 1 min H_2S gas treatment. Scale bar: 0.5 μm.

In a study by Ren *et al.*, it is suggested that overlapping grain boundaries (GBs) are common in monolayer h-BN.[29] The irregular shaped bright lines or areas on monolayer h-BN may represent overlapping grain boundaries (figure 4.8 and 4.10a). The multiple layer triangular h-BN regions seem brighter in SEM images. The overlapping GBs also look brighter as being thicker h-BN regions, similar to double or multiple layer regions. It seems that particles are formed with H_2S treatment on thin bright lines or at the parts that thick bright lines become thinner or indiscernible at the same magnification. This suggests that, as different than monolayer CVD-grown graphene, grain boundary regions can have nanoscale vacancy defects in CVD-grown h-BN. The h-BN nucleation occurs in many locations on the metal substrate surface simultaneously. Unlike graphene, two different elements, B and N, needed for coalescence of individual domains to form monolayer continuous h-BN. Even though the stochiometric equivalence of B and N can be provided by a selected precursor such as borazine (B/N = 1), the actual supply of these elements is dependent on the interaction of the individual elements with the catalyst during CVD.[18] Thus, merging for neighboring domains is more challenging in polycrystalline h-BN than graphene, which may cause vacancy defects at the grain boundary regions (Figure 4.9).[33]

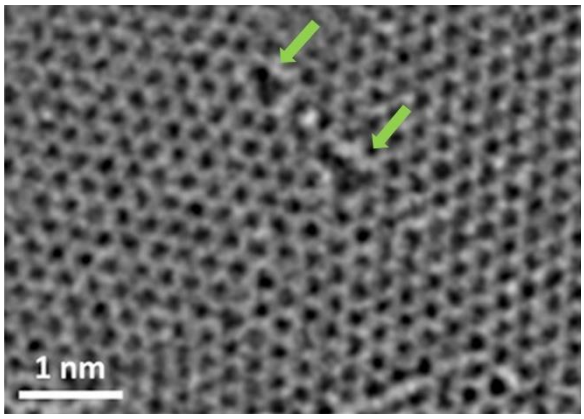

Figure 4.9. HRTEM image of CVD-grown h-BN with vacancy defects at the grain boundary region indicated by green arrows.[33]

In an overlapping GB, while some areas of h-BN grow onto the next grain, some areas can stop or grow with missing atoms due to lack of availability of needed atoms along the GB region. This may result in nanoscale voids along the grain boundaries in h-BN.

In the literature, the revealed grain boundaries of polycrystalline monolayer graphene look like a web of connected lines around the quilted patches.[35] The interconnected bright lines in monolayer h-BN also resembles the similar look of revealed grain boundaries in graphene. A smaller magnification image shows the interconnectivity of the irregular shaped bright lines (Figure 4.10a). After the H_2S gas treatment, Cu_xS particles majorly formed on thinner or intermittent parts of these connected bright lines (Figure 4.10b).

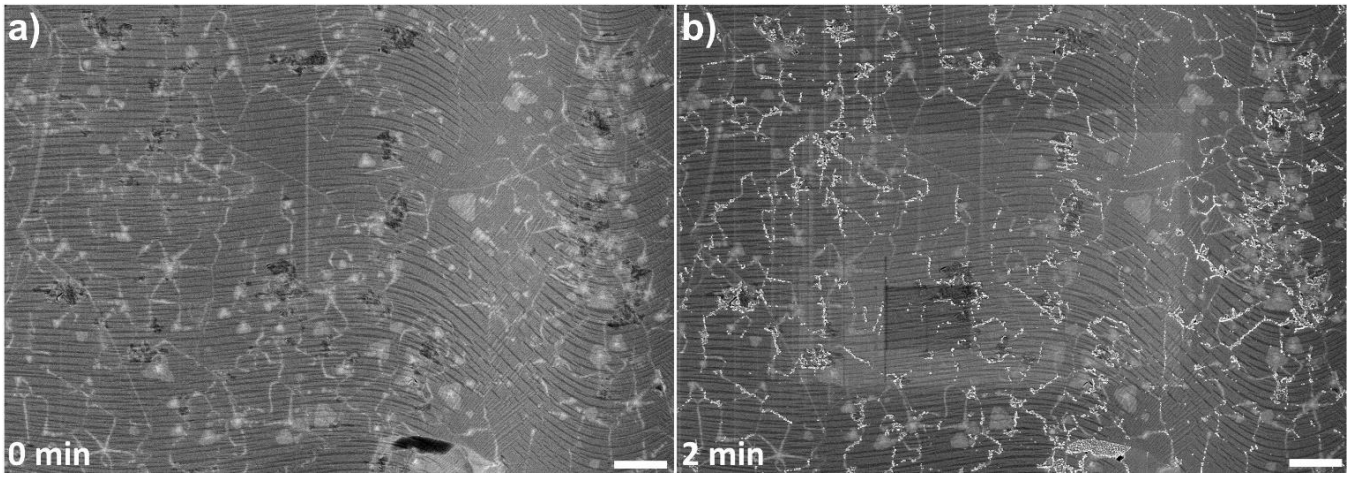

Figure 4.10. SEM images of monolayer h-BN on copper foil before and after 2 minutes of H_2S gas treatment. Scale bar: 2 μm.

Figure 4.11 shows SEM images of monolayer h-BN on copper foil before and after H_2S gas treatment. The possible overlapping grain boundary areas are shown with the orange arrows (Figure 4.11a, c, d). It can be seen in images (Figure 4.11b, d, f) that particles formed partially at the edges of some triangular multilayer regions (shown by blue arrows) and at the bright thin regions (shown with the orange arrows) after the H_2S gas treatment. This suggests

the existence of the voids where overlapping GB has a narrow width and non-existence of the voids where overlapping GB has a large width. To the best of our knowledge, no nanoscale voids in GBs are mentioned or shown experimentally in the literature for the overlapping grain boundaries in monolayer CVD-grown h-BN so far.

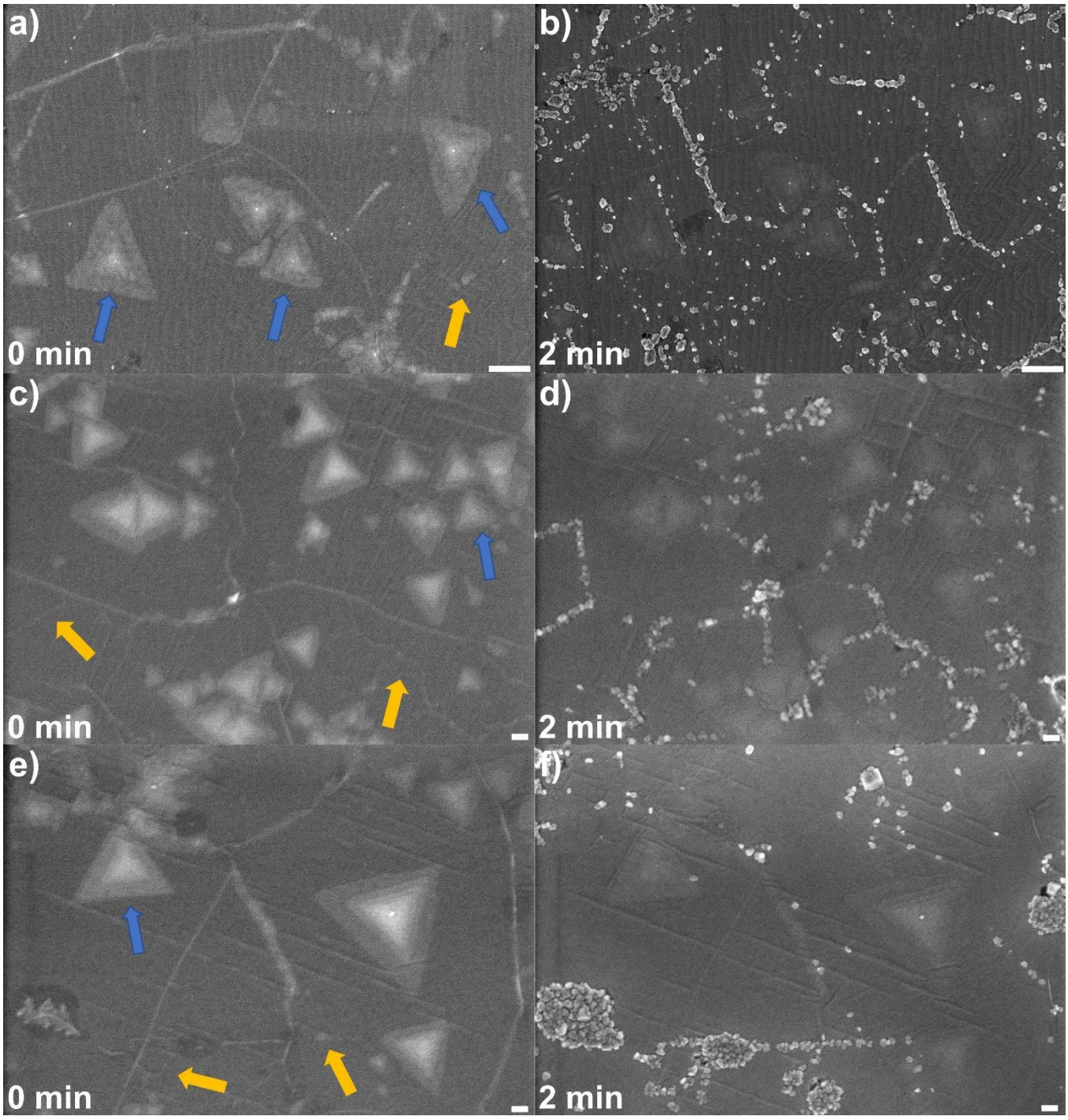

Figure 4.11. SEM images of monolayer h-BN on copper foil before **(a,c,e)** and after **(b,d,f)** H_2S gas treatment. The treatment time is noted on each image. The blue arrows indicate triangular multilayer regions and orange arrows indicate thin or irregular shaped bright regions in **(a,c,e)**, where Cu_xS particle formation is observed. Scale bar: 0.5 µm.

In general, triangular multilayer regions are commonly observed in h-BN samples in the literature as well as in the samples in our work.[27] When excessive amount of H_2S gas used in the treatment procedure, it is seen that no Cu_xS particles formed on triangular bright regions (figure 4.12). This shows that multilayer regions are rarely defective sites and provides better coverage on copper foil. However, the edges of the triangular multilayer regions majorly show particle formation after the treatment.

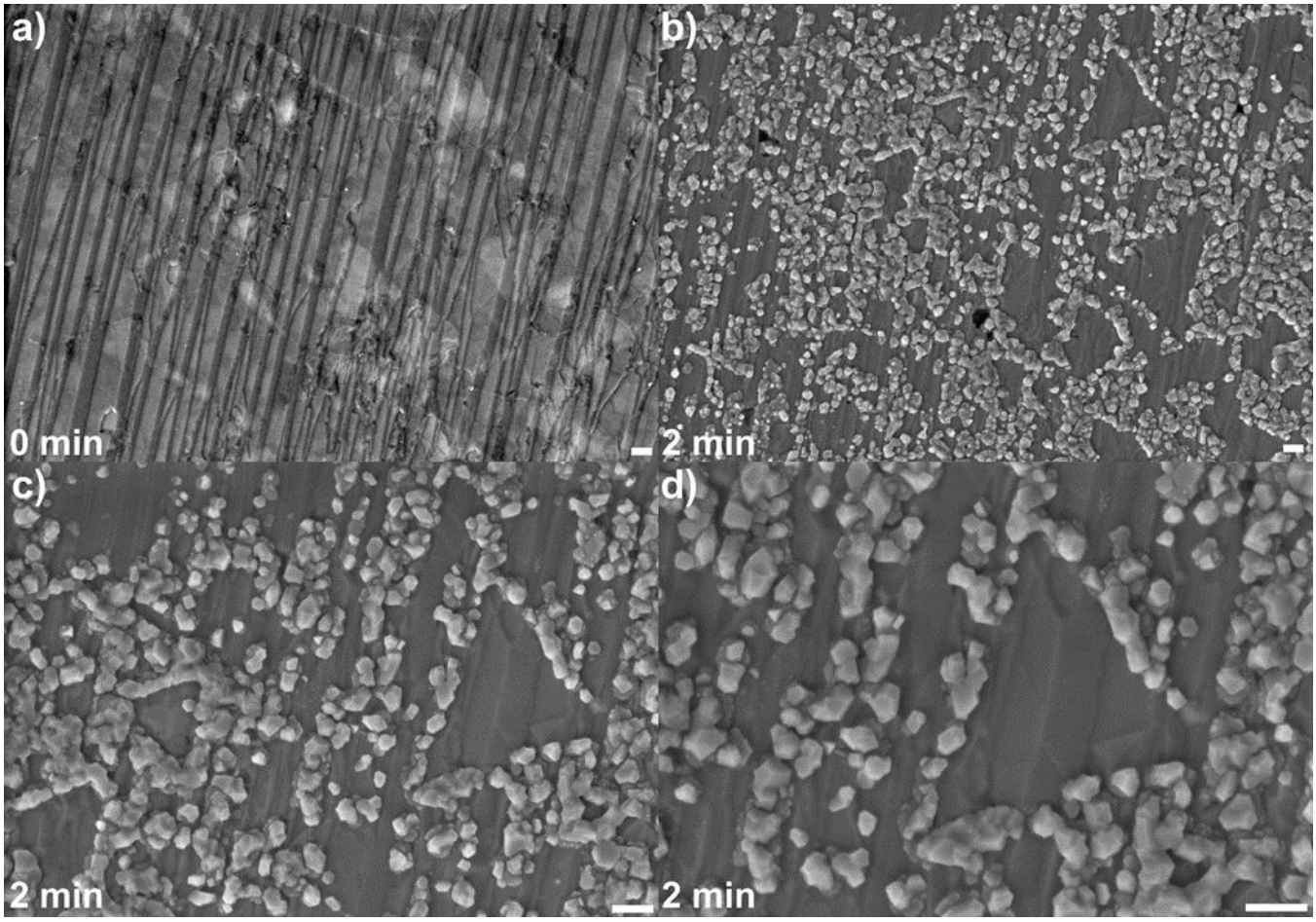

Figure 4.12. SEM images of monolayer h-BN on copper foil before and after H_2S gas treatment. **(a,b)** SEM images of the same region before and after 2 min treatment, respectively. **(c,d)** The higher magnification images of the upper-right region in **(a)**. Scale bar: 0.2 μm.

The low-cost and readily available polycrystalline copper is widely used for the CVD synthesis of 2D materials such as graphene and h-BN. The nucleation density and alignment of newly formed h-BN domains are dependent on the copper crystalline facets that they formed on.[36] The SEM images after H_2S gas treatment in Figure 4.12 shows a high density of defects on h-BN by the formation of excessive particles. Figure 4.12c, the higher magnification SEM image, shows one of the edges of the multilayer triangular h-BN region aligned with the direction of the Cu_xS particles in the same copper domain. This reminds the merging challenge that is illustrated in Figure 4.2d for the individual h-BN grains during the synthesis of monolayer h-BN. Therefore, it is clearly shown that copper crystalline facets have a profound effect on the quality of the synthesized polycrystalline h-BN.

4.4. Conclusion

In conclusion, we have performed *in situ* chemical probing study of vacancy defects in CVD-grown h-BN. Our H_2S gas treatment procedure reveals that currently commercially available CVD-grown monolayer h-BN samples have high density of nanoscale voids. High defect density in monolayer h-BN appears to be caused by the hardship of stitching of individual domains with various rotations and edge atoms. It has been shown that h-BN may have nanoscale vacancy defects along the grain boundaries which is different than graphene. It is important to limit H_2S amount and treatment time for our method to work well towards identification of vacancies.

4.5. References

(1) Zou, X.; Yakobson, B. I., *Acc. Chem. Res.,* **2015***, 48*, 73-80.

(2) Khan, M. H.; Huang, Z.; Xiao, F.; Casillas, G.; Chen, Z.; Molino, P. J.; Liu, H. K., *Sci. Rep*., **2015**, 5, 7743.

(3) Stehle, Y.; Meyer, H. M.; Unocic, R. R.; Kidder, M.; Polizos, G.; Datskos, P. G.; Jackson, R.; Smirnov, S. N.; Vlassiouk, I. V., *Chem. Mater.,* **2015**, 27, 8041-8047.

(4) Zhang, K.; Feng, Y.; Wang, F.; Yang, Z.; Wang, J., *J. Mater. Chem. C*, **2017***, 5*, 11992-1222.

(5) Li, M.; Zhou, S.; Wang, R.; Yu, Y.; Wong, H.; Luo, Z.; Li, H.; Gan, L.; Zhai, T., *Nanoscale*, **2018***, 10*, 17865-17872.

(6) Li, J.; Li, Y.; Yin, J.; Ren, X.; Liu, X.; Jin, C.; Guo, W., *Small*, **2016***, 12*, 3645-3650.

(7) Tay, R. Y.; Wang, X.; Tsang, S. H.; Loh, G. C.; Singh, R. S.; Li, H.; Mallick, G.; Tong Teo, E. H., *J. Mater. Chem. C*, **2014***, 2*, 1650.

(8) Sun, J.; Lu, C.; Song, Y.; Ji, Q.; Song, X.; Li, Q.; Zhang, Y.; Zhang, L.; Kong, J.; Liu, Z., *Chem. Soc. Rev.,* **2018***, 47*, 4242-4257.

(9) Wu, Q.; Park, J.; Park, S.; Jung, S. J.; Suh, H.; Park, N.; Wongwiriyapan, W.; Lee, S.; Lee, Y. H.; Song, Y. J., *Sci. Rep.,* **2015**, 5, 16159.

(10) Koepke, J. C.; Wood, J. D.; Chen, Y.; Schmucker, S. W.; Liu, X.; Chang, N. N.; Nienhaus, L.; Do, J. W.; Carrion, E. A.; Hewaparakrama, J.; Rangarajan, A.; Datye, I.; Mehta, R.; Haasch, R. T.; Gruebele, M.; Girolami, G. S.; Pop, E.; Lyding, J. W.,*Chem. Mater*., **2016**, 28, 4169-4179.

(11) Feigelson, B. N.; Bermudez, V. M.; Hite, J. K.; Robinson, Z. R.; Wheeler, V. D.; Sridhara, K.; Hernández, S. C., *Nanoscale*, **2015***, 7*, 3694-3702.

(12) Guangyuan Lu; Tianru Wu; Qinghong Yuan; Huishan Wang; Haomin Wang; Feng Ding; Xiaoming Xie; Mianheng Jiang, *Nat. Commun*., **2015***, 6*, 6160.

(13) Chang, R.; Wang, X.; Wang, S.; Sheng, Y.; Porter, B.; Bhaskaran, H.; Warner, J. H., *Chem. Mater*., **2017**, 29, 6252-6260.

(14) Nagashima, A.; Tejima, N.; Gamou, Y.; Kawai, T.; Oshima, C., *Phys. Rev. B Condens. Matter Mater.* Phys., **1995**, 51, 4606-4613.

(15) Ismach, A.; Chou, H.; Ferrer, D. A.; Wu, Y.; McDonnell, S.; Floresca, H. C.; Covacevich, A.; Pope, C.; Piner, R.; Kim, M. J.; Wallace, R. M.; Colombo, L.; Ruoff, R. S., *ACS Nano*, **2012**, 6, 6378-6385.

(16) Gao, Y.; Ren, W.; Ma, T.; Liu, Z.; Zhang, Y.; Liu, W.; Ma, L.; Ma, X.; Cheng, H., *ACS Nano*, **2013**, 7, 5199-5206.

(17) Kim, G.; Jang, A.; Jeong, H. Y.; Lee, Z.; Kang, D. J.; Shin, H. S., *Nano Lett*., **2013**, 13, 1834-1839.

(18) Kidambi, P. R.; Blume, R.; Kling, J.; Wagner, J. B.; Baehtz, C.; Weatherup, R. S.; Schloegl, R.; Bayer, B. C.; Hofmann, S., *Chem. Mater*., **2014**, 26, 6380-6392.

(19) Goriachko, A.; He, Y.; Knapp, M.; Over, H.; Corso, M.; Brugger, T.; Berner, S.; Osterwalder, J.; Greber, T., *Langmuir*, **2007**, 23, 2928-2931.

(20) Lee Joo Song; Choi Soo Ho; Yun Seok Joon; Kim Yong In; Boandoh Stephen; Park Ji-Hoon; Shin Bong Gyu; Ko Hayoung; Lee Seung Hee; Kim Young-Min; Lee Young Hee; Kim Ki Kang; Kim Soo Min, *Science*, **2018***, 362*, 817-821.

(21) Sharma, S.; Kalita, G.; Vishwakarma, R.; Zulkifli, Z.; Tanemura, M., *Sci. Rep.,* **2015**, 5, 10426.

(22) Wang, H.; Zhao, Y.; Xie, Y.; Ma, X.; Zhang, X., *J. Semicond.,* **2017***, 38*, 031003.

(23) Wang, L.; Wu, B.; Jiang, L.; Chen, J.; Li, Y.; Guo, W.; Hu, P.; Liu, Y., *Adv. Mater*., **2015***, 27*, 4858-4864.

(24) X. Song, J. Gao, Y. Nie, T. Gao, J. Sun, D. Ma, Q. Li, Y. Chen, C. Jin, A. Bachmatiuk, M. H. Rümmeli, F. Ding, Y. Zhang, Z. Liu, *Nano Res.* 2015, **8**, 3164-3176.

(25) Kim, K. K.; Hsu, A.; Jia, X.; Kim, S. M.; Shi, Y.; Hofmann, M.; Nezich, D.; Rodriguez-Nieva, J. F.; Dresselhaus, M.; Palacios, T.; Kong, J., *Nano Lett*., **2012***, 12*, 161-166.

(26) Bayer, B. C.; Caneva, S.; Pennycook, T. J.; Kotakoski, J.; Mangler, C.; Hofmann, S.; Meyer, J. C., *ACS Nano*, **2017***, 11*, 4521-4527.

(27) Ji, Y.; Calderon, B.; Han, Y.; Cueva, P.; Jungwirth, N. R.; Alsalman, H. A.; Hwang, J.; Fuchs, G. D.; Muller, D. A.; Spencer, M. G., *ACS Nano*, **2017***, 11*, 12057-12066.

(28) Wang, J.; Ma, F.; Sun, M., *RSC Advances*, **2017***, 7*, 1681-16822.

(29) Ren, X.; Dong, J.; Yang, P.; Li, J.; Lu, G.; Wu, T.; Wang, H.; Guo, W.; Zhang, Z.; Ding, F.; Jin, C., *Phys. Rev. Mater.*, **2019***,* 3, 014004.

(30) Lin, W.; Brar, V. W.; Jariwala, D.; Sherrott, M. C.; Tseng, W.; Wu, C.; Yeh, N.; Atwater, H. A., *Chem. Mater*., **2017***, 29*, 4700-4707.

(31) Wong, D.; Velasco, J., Jairo; Ju, L.; Lee, J.; Kahn, S.; Tsai, H.; Germany, C.; Taniguchi, T.; Watanabe, K.; Zettl, A.; Wang, F.; Crommie, M. F., *Nat. Nanotechnol.,* **2015***, 10*, 949-953.

(32) Yin, J.; Yu, J.; Li, X.; Li, J.; Zhou, J.; Zhang, Z.; Guo, W., *Small*, **2015***, 11*, 4497-4502.

(33) Gibb, A. L.; Alem, N.; Chen, J.; Erickson, K. J.; Ciston, J.; Gautam, A.; Linck, M.; Zettl, A., *J. Am. Chem. Soc*., **2013***, 135*, 6758-6761.

(34) Zhang, W.; Yang, S., *Acc. Chem. Res.,* **2009***, 42*, 1617.

(35) Hong, K. P.; Lee, D.; Choi, J. B.; Kim, Y.; Kim, H., *ACS Appl. Nano Mater.,* **2018***, 1*, 2515-2520.

(36) Wang, R.; Purdie, D. G.; Fan, Y.; Massabuau, F. C.; Braeuninger-Weimer, P.; Burton, O. J.; Blume, R.; Schloegl, R.; Lombardo, A.; Weatherup, R. S.; Hofmann, S., *ACS Nano*, **2019***, 13*, 2114.

ALI IHSAN ALTAN

Education

Ph.D., Chemistry

University of Wisconsin-Milwaukee, Milwaukee, WI, USA.

September 2012-May 2019

Advisor: Prof. Jian Chen

Dissertation: *In Situ* Chemical Probing of Vacancy Defects in Graphene and Boron Nitride at Room Temperature

M.Sc., Chemistry

Gebze Technical University, Gebze, Turkey.

September 2010-August 2012.

Thesis Title: Synthesis of Colloidal Quantum Dots Coated with Polymeric Ligands and Investigation of Their Photovoltaic Properties

B.Sc., Chemistry

Anadolu University, Eskisehir, Turkey.

September 2002-June 2008

Research Experience

- Characterization of 2D Nanomaterials such as Graphene, h-BN
- Graphene transfer onto various substrates
- Synthesis of CdSe nanocrystal quantum dots, post-synthesis size separation and ligand exchange.
- Synthesis of various polymers (methacrylate copolymers) by free radical polymerization and their characterization
- Operating injection molding machine to produce plastic articles from commonly used resins such as PET, PE, PA, PS, PVC, etc.

- Mechanical Testing of Polymers/Composites: Impact Test (Charpy/Izod), Tensile Test, MFI by following ASTM standards.
- Analytical techniques: TGA, DSC, GPC, EDS, EBSD, XRD
- Imaging techniques: SEM/EDS, AFM, Optical Microscopy and Raman Microscopy
- Spectroscopy techniques: UV-Vis, FT-IR, NMR, Raman Spectroscopy

Teaching Experience

- Teaching Organic Chemistry, General Chemistry laboratories and discussions for undergraduate classes in UW-Milwaukee, Chemistry Department. Leading organic syntheses and work-up procedures and demonstrating how to use laboratory instruments such as Gas Chromatography and FT-IR, NMR spectroscopy.

Work Experience

2018 May-2018 August

Internship in EHS department at Thermo Fisher Scientific, Eugene, OR.

- Learned and searched about REACH (regulated by ECHA) compliance on a variety of products. Compiled data and created suggestions for product improvement.

2015, 2016 Summer

- Volunteered for patent and market search for Dr. Pradeep Rohatgi at Intelligent Composites, LLC., after a brief training at UWM Research Foundation on intellectual property and market research.

Publications

- Altan, A.I**.**, Chen, J., "*In situ* chemical probing of hole defects and cracks in graphene at room temperature", Nanoscale, DOI: 10.1039/C8NR03109F
- Kuram, E., Tasci, E., Altan, A.I., Medar, M.M.,Yilmaz, F., Ozcelik,B., "Investigating the effects of recycling number and injection parameters on the mechanical properties of glass-fibre reinforced nylon 6 using Taguchi method", Materials and Design, DOI:10.1016/j.matdes.2013.02.027